A PROBABILISTIC APPROACH TO ASSESS THE STABILITY OF FLOOD EMBANKMENTS: THE CASE STUDY OF THE ADIGE RIVER EMBANKMENT

Alessia Amabile

Thesis submitted to the Department of Civil and Environmental Engineering, University of Strathclyde, Glasgow, in fulfilment of the requirements for the degree of

Doctor of Philosophy

in

Civil and Environmental Engineering

May 2018,

Glasgow, UK

Declaration of authenticity and author's right

This thesis is the result of the author's original research. It has been composed by the author and has not been previously submitted for examination which has led to the award of a degree.

Signed:

Date: 21 May 2018

ABSTRACT

Flood embankments are a key asset in flood defence systems; assessing their probability of failure is therefore important for the evaluation of flood hazard. Flood embankments, however, can reach lengths of thousands of kilometres. Probability of failure assessments are complex and expensive, which limits their applicability on such a large scale. This challenge highlights the need to develop both a simple probabilistic approach that does not require excessive time or computational effort, and an affordable method for the deterministic hydro-mechanical characterisation of flood embankments that can easily be extended to long segments.

This thesis addresses these challenges by first focusing on the development of an accessible probabilistic method that accounts for uncertainties in the soil properties and hydrological loading. This approach benefits from the simple First Order Second Moment method while addressing its main limitation, namely the assumed probability distribution of the Factor of Safety. The approach is successfully validated against its ability to capture the annual probability of failure of a segment of the Adige River embankment that experienced instability of the landside slope.

The hydro-mechanical model of the embankment is characterised via site investigation and laboratory tests. In particular, the hydraulic model is characterised via inverse analysis of water flow in the saturated and unsaturated zones based on field monitoring data. However, this approach may be difficult to extend to long segments of the embankment, given the challenge to monitor water flow on a large scale. In order to address this issue, the use of Electrical Resistivity Tomography (ERT) for monitoring of water flow is investigated. Results show that ERT can be a valuable tool to quantify water content if a field-specific relationship between water content and ERT-measured resistivity is calibrated.

The case study of the Adige River embankment is further analysed to investigate the factors governing the water flow and stability of the embankment. Comparison of the water flow regime between two sections, located within and outside the failure segment, highlights the critical role played by the hydraulic response of the material on the landside outside the footprint of the embankment. This key finding can support the decision-making process when planning site investigation aimed to the stability assessment of flood embankments.

These outcomes combine to provide a flexible approach for the probabilistic stability analysis of flood embankments that can be easily adapted and applied to different contexts with limited levels of investment of time and resource. This approach may be developed into a suitable tool for the routine hazard assessment of the stability of flood embankments.

List of journal papers:

1. ‘An accessible approach to assess the probability of failure of flood embankments taking into account transient water flow’ – *A. Amabile, M. P. Cordão-Neto, A. Tarantino*. Submitted for publication to Natural Hazards.
2. ‘Failure hazard of flood embankments due to uplift pressure: lesson learned from the Adige River case study’ – *A. Amabile, A. Pozzato, A. Tarantino*. Submitted for publication to Journal of Geotechnical and Geoenvironmental Engineering.
3. ‘An assessment of ERT as a method to monitor water content regime in flood embankments: the case study of the Adige River embankment’ – *A. Amabile, B.C.F.L. Lopes, V. Beneš, A. Tarantino*. To be submitted for publication to Physics and Chemistry of the Earth.

Contributions of authors:

1. M. P. Cordão-Neto provided advice and feedback about the use of FOSM method.
2. A. Pozzato performed the laboratory tests for the soil characterisation (water retention, shear strength, saturated hydraulic conductivity) and supervised the installation and field calibration of the instruments.
3. B.C.F.L. Lopes provided support and advice for the inversion of ERT data. V. Beneš carried out ERT measurements and provided advice about the inversion process.

A. Tarantino supervised the development of research for all the papers.

Acknowledgements

I would like to express my thanks to my supervisor Alessandro Tarantino for his support, his ideas and his enthusiasm for the research. Thanks to him the PhD has been a productive experience that helped me to grow as a researcher and as a person.

I would also like to thank Manoel Cordão-Neto for his academic and moral support in the last two years and Annarita Pozzato for her energy and encouragement.

I gratefully acknowledge the funding received towards my PhD from the Autonomous Province of Bolzano and the support given by Fabio De Polo.

I would like to express my gratitude to my examiners Luca Pagano and Chris White for their time and constructive feedback.

I am very grateful to my parents and to my brothers Andino e Nangio for their infinite love and encouragement, not only during my PhD but in every moment of my life. Even if we are far apart you are my greatest source of energy and whenever I feel lost I think of you. A special thanks also to nonna Gianna, who despite her age has never stopped pushing me to do my best.

I would like to thank Alejandro for being always by my side, even when we were thousands of miles apart.

I am deeply grateful to my friends Gea, for the never ending conversations and for the unconditional support that gave me strength in the toughest times, and Brunella, for the optimism and positive attitude that never failed to cheer me up. We shared every moment of this journey and I would never have made it without you.

Finally, I would like to thank my friends in Glasgow for all the enjoyable and memorable moments that we shared in the last few years, and in particular I would like to thank Riccardo, Elena and Carolina for their constant support and friendship.

Table of Contents

3. FAILURE HAZARD OF FLOOD EMBANKMENTS DUE TO UPLIFT PRESSURE: LESSON LEARNED FROM THE ADIGE RIVER CASE STUDY 63

1. INTRODUCTION

1.1 Background

Flood embankments are one of the major assets in flood defence systems all over the world. The frequency and intensity of flood events has seen an increase in recent years, and this trend is expected to grow even more in the future because of climate change. For this reason, assessing the flood hazard associated with the instability of flood embankments is extremely important.

In current engineering practice, the common methods for stability analysis of flood embankments are mostly deterministic. However, natural hazards such as floods are uncertain phenomena by definition, due to the impossibility to predict exactly the time and magnitude of future events. Moreover, soils are materials of natural origin and therefore the characterisation of their hydro-mechanical properties is an additional source of uncertainty. These uncertainties should therefore be taken into account by determining the stability of the embankment in terms of probability of failure.

In order to assess the stability of the embankment, the hydro-mechanical model has to be characterised. This can be achieved via site investigation, laboratory testing and field monitoring. In particular, the hydraulic characterisation of the soil in the saturated and unsaturated zone can be carried out via inverse analysis of field monitoring of water flow regime. However, flood embankments are linear structures which can cover lengths of thousands of kilometres and field monitoring of water flow on such a large scale may prove challenging in practice. Traditional geotechnical monitoring systems based on local sensors can only provide information at a local scale and may not represent an effective solution for long linear structures like flood embankments.

This research provides a method for the hydro-mechanical characterisation of the deterministic model required for the stability analysis, and aims to develop a probabilistic approach to assess the stability of flood embankments. In particular, in order to address the issue related to the characterisation of the hydro-mechanical model for long structures like flood embankments, the use of suitable tools for large scale monitoring of water flow is assessed.

1.2 Literature review

1.2.1 Flood embankments

Flooding is one of the most frequent and destructive natural hazards worldwide and it has a substantial impact on the population from a social and economic point of view. Recent records have shown an increase in the number of catastrophic flood events and both intensity and frequency of flood events are expected to grow in the future because of climate change (Guerreiro, et al., 2018).

Embankments (or levees) are a common type of flood defence structure used to protect people and land from the devastating effects of flooding. Flood embankments are raised structures that run usually parallel to rivers, with the aim to contain water when the river level rises and prevent it from flooding the surrounding areas (Figure 1.1). Failure of these structures can have catastrophic consequences, both in terms of loss of human lives and damages to roads, properties and infrastructure.

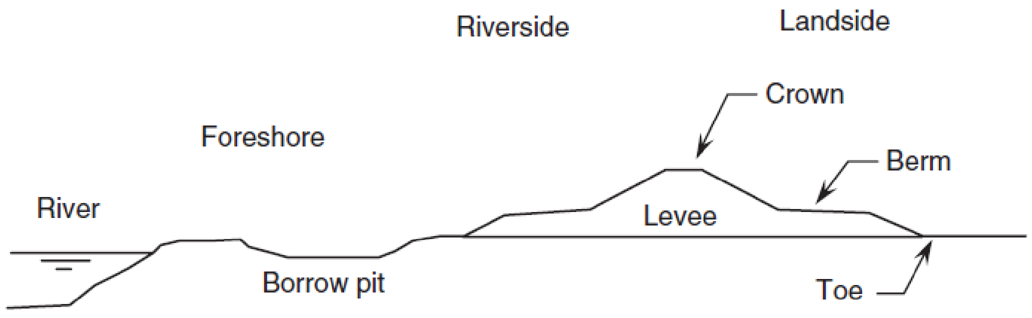

Figure 1.1. Example of cross section of flood embankment (Phoon, 2008).

Failure of flood embankments can be generated by different mechanisms, most commonly overtopping, erosion or slope instability (Phoon, 2008).

Overtopping occurs when river level exceeds the height of the embankment and water floods the protected area. This failure mechanism depends on the geometry of the embankment.

Erosion is determined by the wearing action of water or other atmospheric agents on the soil surface (CIRIA 2013). As a consequence of erosion, soil particles are gradually washed away and the cross section of the embankment becomes smaller. Besides the damage associated with erosion, the changes in the geometry of the embankment can lead to failure by other mechanisms such as instability. A protection measure against erosion can be provided by vegetation covers, concrete revetments or rocks at the toe of the embankment on the riverside.

Global instability occurs when the shear strength of the soil along a slip surface is not sufficient to withstand the loading generated by the water and the embankment weight. This can lead to rotational or translational slides, most commonly of the landside slope. Instability of the riverside slope is more commonly associated with drawdown conditions, which can trigger instability if the water level decrease is quicker than the pore water pressure dissipation in the soil (Phoon, 2008). This is an issue for embankments made of fine materials such as clays, which have a very low permeability. Another aspect that can lead to instability of the riverside slope in clay embankments is related to seasonal variations: cracks may develop in the clay layer during the dry season and then fill with water during flood events, leading to infiltration and slope instability.

Failure can also occur as a combination of different failure mechanisms. For example, the flood wave following overtopping may lead to erosion of the landside slope, or the decrease in cross section of the embankment due to erosion may lead to steeper slopes and therefore instability.

A recently developed tool to analyse failure of flood embankments is represented by fragility curves (Figure 1.2). Fragility curves describe the probability of failure over a range of loading conditions (Buijs, et al., 2007). Fragility curves allow expressing the probability of failure associated to different failure mechanisms for varying values of water level. One limitation of this approach is that the flood event is represented by a single value of water level. This may be a suitable assumption when considering failure by overtopping, when it may be sufficient to characterise the water level by using the maximum river level which is the only parameter determining the failure.

When assessing the probability of failure due to instability, however, this assumption may not be appropriate. Considering a single value of water level corresponds to a steady state seepage analysis, which in turns means assuming that the water level is maintained at that elevation for an infinite amount of time. However, this is not the case during a flood event (Tracy, et al., 2016), when the water level rises to a peak and then recedes. The water front propagates in the unsaturated soil of the embankment when the water level rises only to a certain degree, and then starts receding when the water level decreases: steady state flow conditions may not be reached during the flood event (Pozzato, et al., 2014).

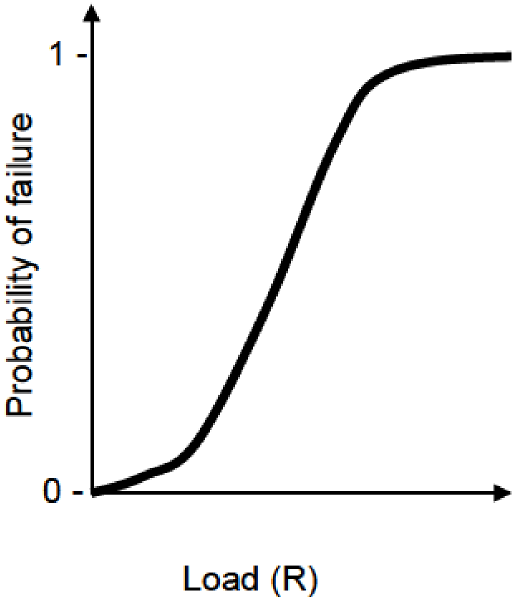

Figure 1.2. A conceptual fragility curve (Schultz, et al., 2010).

The stability of flood embankments should be assessed by accounting for transient water flow, therefore a time-dependent hydrological loading should be considered. The flood event should not be defined by a single value corresponding to the maximum river level, but using the full hydrograph, i.e. a function describing the evolution of the river level over time. In this case other factors like duration of the flood or shape of the hydrograph should be considered. This highlights the need for a probabilistic method to assess the stability of flood embankments which allows accounting for the time-dependent hydrological loading represented by the hydrograph.

1.2.2 Stability analysis of flood embankments

In the current engineering practice, the traditional methods for designing or verifying geotechnical structures, such as dams or embankments, are mostly deterministic. This means they treat values of the input variables as if they were fixed, and precisely known. However the process involves many uncertainties, generated by different sources. First of all, natural phenomena, such as floods or earthquakes, are affected by uncertainty due to the inability to predict where and when they will occur and with what consequences. These natural phenomena represent the loading on geotechnical structures and therefore need to be assessed and quantified in the hazard assessment. An additional source of uncertainty lies in the characterisation of the hydro-mechanical behaviour of soils. Given their natural origin, soil properties usually show a large variability and this uncertainty can be expanded by the lack or scarcity of experimental data.

The shortcomings of deterministic approaches in common practice in geotechnical engineering have long been recognised. In 1997 the U.S. Army Corps of Engineering had already introduced the concept of probabilistic methods in geotechnical engineering (U.S. Army Corps of Engineers, 1997). In many cases design codes and guidelines have included these considerations by accounting for uncertainties with a semi-probabilistic approach, for example as in the Eurocodes (CEN, 2004), which prescribe the use of appropriate values for partial safety factors to account for uncertainties in the mechanical characterisation of materials or in the loading.

To consider and quantify uncertainties in the process of hazard assessment, the stability of flood embankments should be assessed with a probabilistic approach.

Probabilistic approaches enable uncertainty in the loading and soil hydro-mechanical properties to be taken into account by defining them in probabilistic terms.

In the context of slope stability, the result of a deterministic stability analysis is a single value of the Factor of Safety; the failure corresponds to a value of Factor of Safety lower than or equal to one. With a probabilistic approach the result is expressed in terms of probability of failure, which corresponds to the probability of observing a Factor of Safety lower than or equal to one. The inadequacy of a single value of the Factor of Safety to describe the safety of a structure is clearly exemplified by Christian, et al. (1994) by comparing two different ideal scenarios (Figure 1.3). In the first scenario, the mean Factor of Safety, corresponding to a ‘deterministic’ value, is equal to 1.5, but there is a large uncertainty about its value, shown by the large standard deviation and the wide shape of the probability distribution. In the second scenario, the ‘deterministic’ Factor of Safety is equal to 1.2, but there is less uncertainty about its value, shown by the small value of the standard deviation and therefore the narrow shape of the probability distribution function. A deterministic analysis would conclude that the first scenario is safer than the second, given the greater value of the Factor of Safety. In fact, when comparing the probability of failure, represented by the probability of having a Factor of Safety lower than one, it is clear that the first scenario has a higher overall probability of failure (represented by the shaded area). This outcome cannot be captured by a deterministic approach.

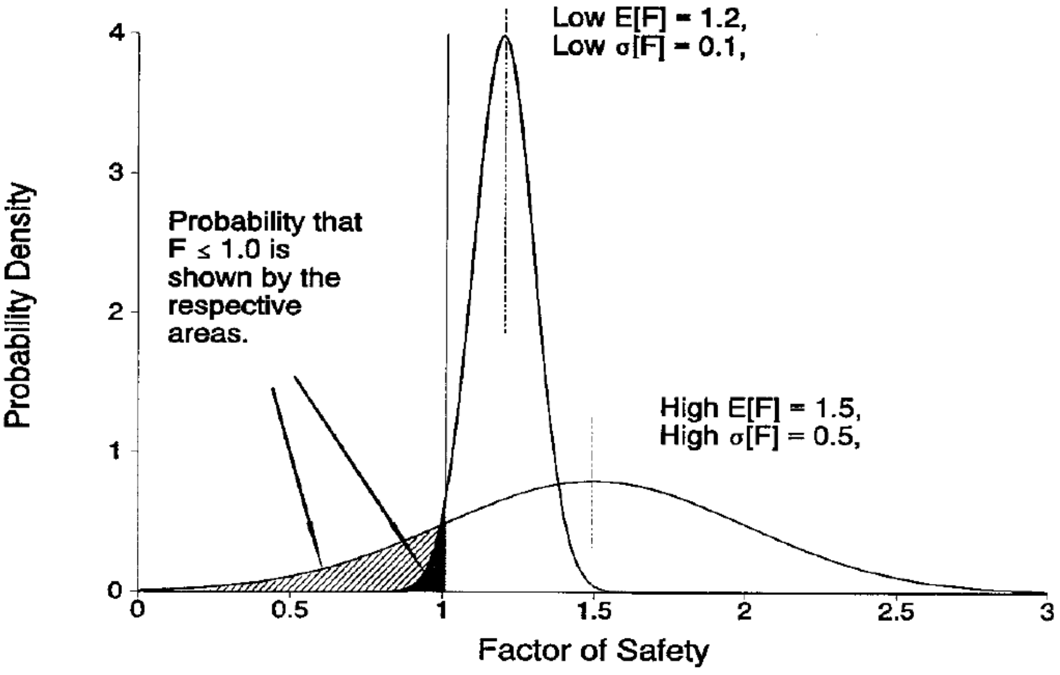

Figure 1.3. Comparison of two situations with different means and distributions of Factor of Safety, modified from Christian, et al. (1994).

1.2.3 Probabilistic methods in slope stability analysis

1.2.3.1 The Monte Carlo method

The Monte Carlo method is one of the most common probabilistic methods in engineering and it has been extensively applied to slope stability problems. The Monte Carlo method is a useful tool to obtain estimates of solutions to complex problems which can't be solved analytically. This is frequently the case in geotechnical engineering, where closed-form solutions are not available for many common problems (Fenton, 2014).

The Monte Carlo method is based on the repeated sampling of random numbers (Zio & Marseguerra, 2002) and requires solving the same problem a number of times, by sampling in every iteration a random value of the uncertain variable to take into account. In every iteration one random number is associated to one random value of the variable, through its probability distribution. This value is used as input to solve the ‘deterministic’ problem. For every iteration a different value of the input variable randomly generated is used and one solution to the deterministic problem is obtained. This process is repeated a number of times, in order to cover all the range of possible outcomes and estimate the probability distribution of the system response.

One of the first applications of this method to slope stability problems goes back to 1982, when Tobutt assessed the probability of failure of a multi-layered slope taking into account uncertainties in soil properties, such as density and shear strength, and in the pore water pressure expressed in terms of average pore pressure ratio.

The choice of soil properties to be considered in probabilistic terms in slope stability problems is not always obvious, and has seen different interpretations in the literature. The need to account for the uncertainty in the shear strength parameters has been widely recognised, to the point that even some commercial software offer now the chance to describe friction angle and cohesion in terms of probability distributions (GEO-SLOPE, 2004). However, many authors have also acknowledged the key role played by the hydraulic characterisation of the soil in the context of the stability analysis.

Among the hydraulic properties, the hydraulic conductivity determines seepage rate and therefore the pore water pressure distribution in earth structures. Pore water pressure distributions in turn affect the effective stress state, hence the shear strength and the stability of the structure. This means that uncertainty associated with the hydraulic conductivity leads to uncertainty about the pore water pressure distribution, and therefore about the stability of the slope (Gui, et al., 2000).

The seepage in unsaturated structures like embankments is also affected by the water retention behaviour of the soil in the unsaturated range. The uncertainty in the soil's behaviour in the unsaturated range can be accounted for by describing the water retention curve parameters with a probability distribution. For example if Van Genuchten's model is adopted for the water retention and hydraulic conductivity curve (Van Genuchten, 1980), the parameters α and n can be described by a probability distribution (Calamak & Yanmaz, 2017).

In principle, the Monte Carlo method is a flexible tool and can be used to account for uncertainty in a large number of variables, including shear strength, hydraulic conductivity and water retention curve parameters. However, its main limitation lies in the number of iterations required to have a sufficiently accurate estimate of the probability of failure: when more random variables are taken into account a greater number of iterations is required to obtain meaningful results. This can become time consuming and computationally demanding, and limits the suitability of the method for routine engineering applications (El-Ramly, et al., 2002).

1.2.3.2 The First Order Second Moment method

The First Order Second Moment (FOSM) method has often been recommended as a probabilistic method that can be easily adopted in routine geotechnical engineering design (Duncan, 2000) due to its simplicity and low computational effort.

The FOSM method can be used to estimate the mean and variance of a performance function Y depending on a number of independent random variables $X_1, \ldots, X_n$ as:

$$\mu[Y] \cong Y(\mu[X_1], \mu[X_2], \ldots, \mu[X_n])$$

Eq. 1.1

$$\sigma^2[Y] \cong \sum_{1}^{n} \left(\frac{\partial Y}{\partial X_i}\right)^2 \sigma^2[X_i] \qquad \textbf{Eq. 1.2}$$

These equations are derived from a Taylor's series expansion about the mean values of the random variables by retaining only first order terms (Wolff, et al., 2004). If there is a correlation between two or more of the random variables it should be considered in the calculation of the variance of the performance function.

The partial derivatives required to calculate the variance are evaluated at the mean value of the considered random variable X_i. The calculation of these derivatives may pose a challenge when a closed-form solution is not available, as is usually the case for seepage or stability problems. They can be calculated numerically by selecting an increment ΔX_i for each variable and evaluating the performance function Y in two points corresponding to the mean value plus and minus the selected increment ΔX_i. The value of ΔX_i is usually taken equal to the standard deviation of the input variable, to capture the non-linear behaviour of the performance function in a range of likely values (Wolff, et al., 2004).

In the context of slope stability analysis, the performance function is represented by the Factor of Safety. This procedure is shown in Figure 1.4 for a single input variable. The mean value of the Factor of Safety $\mu(FS)$ is calculated starting from the mean value of the input variable $\mu(X)$ (this corresponds to a routine deterministic analysis). If there is no uncertainty in the value of the input variable, there is no uncertainty in the resulting value of Factor of Safety either. However, the input variable is characterised by an uncertainty represented by its probability distribution. This uncertainty is taken into account by considering a range of likely values for the input variable around its mean value $(\mu(X)-\Delta X, \mu(X)+\Delta X)$. The Factor of Safety is calculated in two points corresponding to the extremes of this range. The resulting values define a range for the Factor of Safety representing its uncertainty.

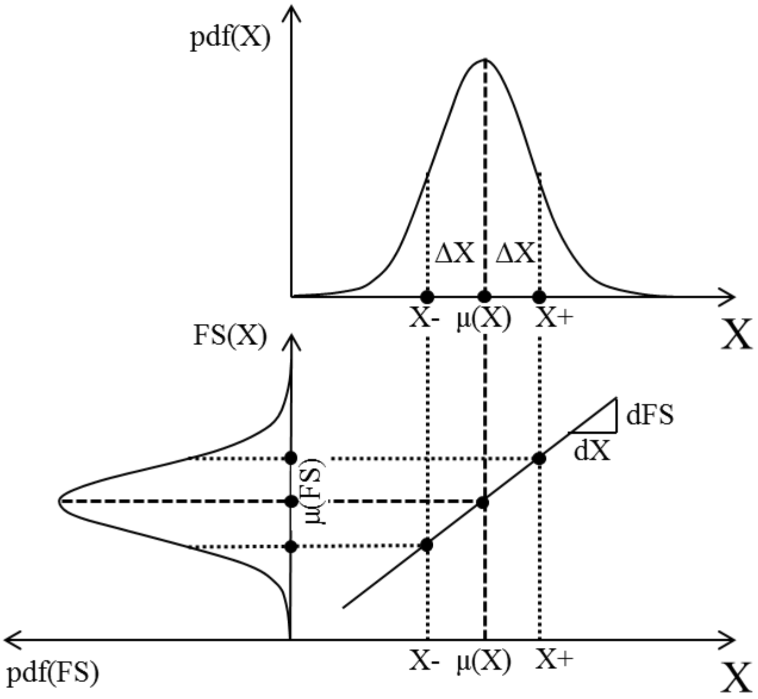

Figure 1.4. Application of FOSM method with a single variable, after Wolff, et al. (2004).

The application of the FOSM method to slope stability problems on its own does not allow calculating the probability of failure, because it only provides information about the mean and variance of the Factor of Safety; in order to calculate the probability of failure the shape of the probability distribution must be known as well, and the FOSM method does not provide any information about it. This means that a probability distribution function must be assumed to calculate the probability of failure.

Baecher and Christian (2005) recommend assuming a Normal distribution considering it a simple and conservative assumption, which will tend to overestimate the probability of failure. This assumption would also be somehow justified by the

Central Limit Theorem, which states that the distribution of the sum of a large number of random variables converges to a Normal distribution. This would be the case for geotechnical problems, where a large number of causes is contributing to the final effect, which should therefore be described by a Normal distribution. This assumption has been validated by Malkawi (2000) by fitting a Normal distribution on the empirical probability distribution of the Factor of Safety obtained from a Monte Carlo simulation. However, it can be argued that the Factor of Safety can only have positive values; this would be better represented by assuming a LogNormal distribution, as recommended by Duncan (2000), although he implies that a certain personal judgement is required in the assumption. This assumption has been followed in several studies (e.g. Phoon, 2008; Gui, et al., 2000).

The choice of the probability distribution is not a minor issue in the calculation of the probability of failure. Computed values of probability of failure are sensitive to the choice of the probability distribution function and this is especially the case when estimates of low probabilities are required, as in the case of safe structures (El-Ramly, et al., 2002). This is confirmed by the results obtained by Liang, et al. (1999), who have analysed the stability of the King Talal Dam under different conditions and compared results obtained by assuming a Normal and LogNormal distribution for the Factor of Safety. For the same analysis and slip surface the probability of failure can change by up to four orders of magnitude, and the difference increases for lower values of probability of failure (Table 1.1). This is a further confirmation that the a priori assumption of the probability distribution function constitutes the major limitation to the application of the FOSM method in the calculation of the probability of failure.

Loading condition	**Mean Factor of Safety**	**Probability of failure – Normal distribution**	**Probability of failure – LogNormal distribution**
End of construction downstream face	1.653	1.92E-3	1.43E-4
End of construction upstream face	2.089	8.64E-6	8.50E-10
Rapid drawdown downstream face	1.718	1.18E-3	5.04E-5
Rapid drawdown upstream face	1.280	4.32E-2	3.02E-2
Steady-state seepage downstream face	1.732	7.24E-4	2.15E-5

Table 1.1. Values of mean Factor of Safety and probability of failure based on Normal and LogNormal distributions for the King Talal Dam (redrawn from Liang, et al. (1999)).

1.2.4 Electrical Resistivity Tomography

The Electrical Resistivity Tomography (ERT) is based on the measurement of apparent resistivity in the subsoil under a flow of direct electric current via an electrode array. The basic discrete set is formed by a four electrode array, with two current injection electrodes and two potential measurement electrodes. In general, electrodes arrays can have different configurations (Figure 1.5) which influence the resolution, sensitivity, signal strength and depth of investigation.

Successive discrete sets of four electrodes are addressed one at a time until the entire array has been scanned and the apparent resistivity map has been obtained (Reynolds, 2011). The depth of investigation increases with increasing electrode spacing and the distribution of true electrical resistivity in the ground is obtained by inversion of the apparent resistivity data.

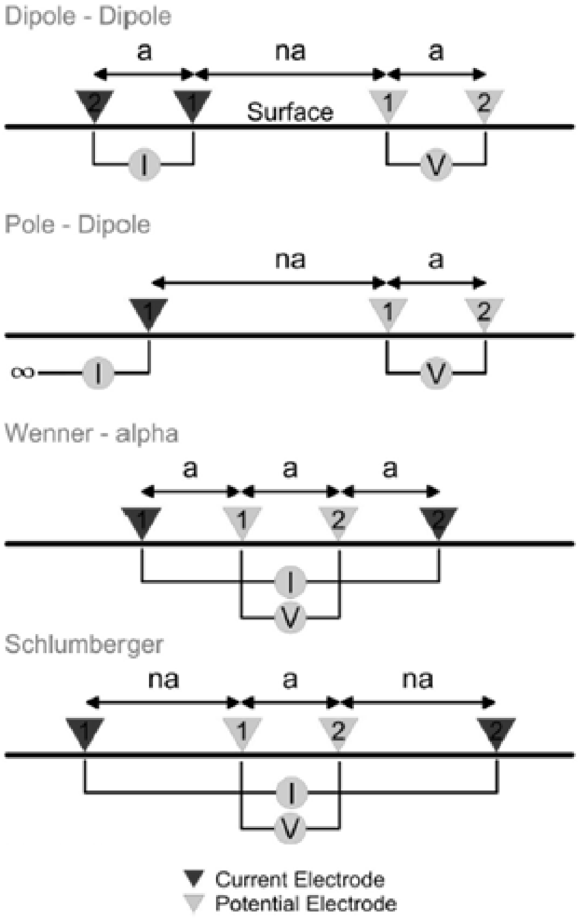

Figure 1.5. Common electrode array configurations (Gunn, et al., 2015).

The electrical resistivity of soil depends on several factors, including the size and mineralogy of the solid particles, the porosity and the degree of saturation (Samouelian, et al., 2005). If material properties such as porosity and particle size remain constant over time in an earth structure, changes in resistivity can be related to water flow in the soil (Johansson & Dahlin, 1996). Resistivity profiles measured over time can therefore be used to obtain a qualitative estimate of water flow in the soil, with lower resistivity linked to higher water content and higher resistivity linked to low water content. For this reason ERT can be applied to monitor water flow in the subsoil and offers a cheaper solution compared to geotechnical monitoring systems, especially for long structures such as flood embankments (Cygal, et al., 2016).

One of the advantages of ERT is represented by its ability to monitor larger areas compared to conventional geotechnical monitoring systems. This can be useful when trying to detect preferential flow paths in the subsoil, which may be difficult to capture with local sensors such as piezometers. However, resistivity data can only provide qualitative information about the seepage and results may be challenging to interpret if they are not coupled to geotechnical monitoring data (Lin, et al., 2013).

In order to obtain a quantitative estimate of the water content from the resistivity data, the relationship between the electrical resistivity and the soil water content has to be calibrated. Electrical resistivity in a partially saturated medium is related to porosity and degree of saturation via the empirical relationship derived by Archie (1942) as:

$$\rho = k \cdot n^{-p} \cdot S_r{}^{-m}$$

Eq. 1.3

where ρ is the electrical resistivity, n is the porosity of the soil, S_r is the degree of saturation and k, p and m are coefficients depending on the type of soil, with k also dependent on the resistivity of the pore fluid. Experimental evidence has shown that the coefficients p and m can be assumed to be equal, leading to the formulation of the generalised Archie’s law (Shah & Singh, 2005), which can be used to describe the relationship between electrical resistivity and volumetric water content θ:

$$\theta = \alpha\rho^{-\beta}$$

Eq. 1.4

The parameters α and β can be obtained experimentally to derive a soil specific relationship between electrical resistivity and water content. This can be achieved by measuring the electrical resistivity and water content of soil samples in the laboratory. The same relationship can then be used to estimate in situ water content from ERT resistivity measurements. This has proved to be a successful method to predict water content in the field for homogeneous soils reaching shallow depths, as shown by the work of Brunet, et al. (2010), in which the water content inferred from ERT measurements has been validated against field measurements via TDR.

Another option is offered by the field calibration of the relationship between resistivity inferred from ERT measurement and volumetric water content. This can be achieved by measuring water content in the field at the same time as ERT measurements and relate it to the ERT-measured resistivity to determine the parameters in Archie’s law (Fan, et al., 2015). This method may be more suitable to estimate water content over a soil profile with different layers or to investigate greater depths.

The resistivity of soils can vary in a very wide range, going from 10 Ωm for clays up to 10000 Ωm for coarse gravels (Figure 1.6). When ERT is used in sites where a variety of materials can be found, the profiles returned by ERT can exhibit large variations of resistivity. In this case the interpretation of ERT results may become more difficult because of artefacts generated during the inversion process by the high contrast in resistivity between different soil layers. The high contrast in resistivity can generate areas of increased resistivity during the inversion and affect the interpretation of the results, as proved in studies where a high contrast in resistivity was observed because of the presence of different soil layers (Carey, et al., 2017). The same effect has also been observed in different applications where strong resistivity contrasts were found to make the inversion and interpretation of ERT-measured resistivity more complex and less reliable (Hilbich, et al., 2009).

In cases where such contrasts are observed it is important to evaluate critically the results of ERT data inversion in order to identify artificial regions in the resistivity profiles which do not reflect changes of water content in the subsoil but are simply to be attributed to inversion artefacts.

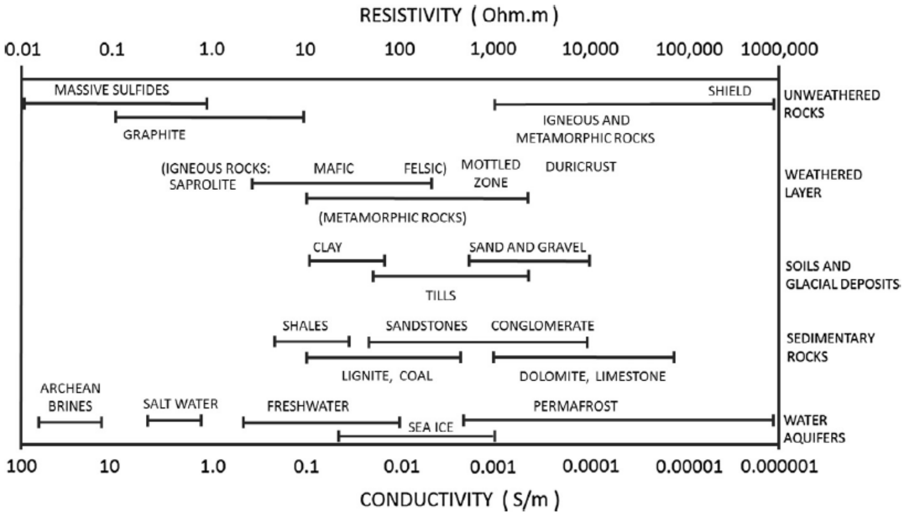

Figure 1.6. Resistivity ranges for surface waters, rocks and soils (Gunn, et al., 2015).

1.3 Aim and objectives

The aim of this research is to develop a probabilistic approach for the stability assessment of flood embankments and to provide a method to characterise the deterministic hydro-mechanical model for the stability analysis.

Flood embankments are usually small structures in terms of cross section, but they can reach lengths of thousands of kilometres. For the design and performance assessment of strategic and massive structures like dams, a great deal of investment and time is usually spent to achieve a detailed characterisation and the use of complex methods to assess their probability of failure is justified. On the other hand, for flood embankments the challenge is represented by the need to extend the performance assessment to very long segments with limited economic resources. In this case a quicker, more flexible tool is required for both the characterisation of the deterministic model and the probabilistic stability analysis. Complex and time-consuming probabilistic methods are not suitable to assess the probability of failure of these structures and a detailed characterisation based on the results of field monitoring is hardly feasible for long, linear structures. This research aims to address this issue by developing an accessible probabilistic approach for the stability analysis and by investigating the use of suitable techniques for the large scale monitoring of water flow in flood embankments. This will be developed with reference to a case study of a flood embankment on the Adige River in Northern Italy.

The main objectives of this are:

1. Develop and validate a probabilistic approach to calculate the probability of failure of flood embankments which is accessible to geotechnical engineers with a traditional “deterministic” background and easy to implement in hazard assessment in routine engineering applications;
2. Characterise the hydro-mechanical model for the stability analysis of the embankment and employ it to analyse the failure case study of a segment of the Adige River embankment;
3. Assess the use of ERT method for the monitoring of water content in the unsaturated soil in flood embankments and highlight its advantages and limitations.

1.4 Thesis outline

After providing a general overview of the research background and objectives (**Chapter 1**), the thesis is structured as follows:

Chapter 2 presents the development of an accessible probabilistic approach for the hazard assessment associated with the instability of flood embankment. The approach is based on the application of the FOSM method to calculate the mean and variance of the Factor of Safety. The main limitation of the FOSM method lies in the a priori assumption of the probability distribution of the Factor of Safety, which is required to calculate the probability of failure of the embankment. This limitation is addressed by suggesting a criterion based on the application of the Monte Carlo method with a single random variable to select the appropriate probability distribution for the Factor of Safety. The method is tested and validated against the failure case study of a segment of the Adige River embankment which experienced instability of the landside slope.

Chapter 3 further develops the analysis of the case study of the Adige River embankment with respect to two cross sections, located within and outside the failure segment. Results of site investigations and hydro-mechanical characterisation of the embankment material and its foundation are presented. The hydro-mechanical model based on laboratory tests and field monitoring data is used to compare water flow regimes between the two sections. Results of water flow simulations are used to highlight the critical role played by the hydraulic response of the material on the landside in the development of uplift pressures at the toe of the embankment. This emphasizes the importance of characterising the hydraulic properties of the material on the landside outside the footprint of the embankment in the context of site investigation.

Further attention to large scale monitoring of water flow is given in **Chapter 4**, which assesses the use of ERT as a tool for quantifying water content in flood embankments. Two ERT measurement campaigns were carried out on the same segment of the Adige River embankment with the aim to map water content in the unsaturated zone. The relationship between water content and electrical resistivity for the material of the embankment was determined in the laboratory using Time Domain Reflectometry (TDR) and was used to convert the ERT-derived resistivity profiles into water content profiles in the embankment. These were compared to water content profiles derived from numerical simulations of water flow based on the inverse analysis of field monitoring data. When the laboratory derived relationship between resistivity and water content is used, only a qualitative assessment of water content profiles is achieved. This is attributed to artefacts generated in the inversion process by the high resistivity contrasts observed between the different layers of the embankment. However, if a field specific relationship between ERT-measured resistivity and water content is developed, ERT offers a good quantitative prediction of water content in the embankment.

Further details about the laboratory determination of the relationship between electrical resistivity and water content for unsaturated soils are provided in the **appendix**.

2. AN ACCESSIBLE APPROACH TO ASSESS THE PROBABILITY OF FAILURE OF FLOOD EMBANKMENTS TAKING INTO ACCOUNT TRANSIENT WATER FLOW

Abstract

Flood embankments are one of the most important flood defence measures. Stability of these structures should be assessed in probabilistic terms by taking into account uncertainties associated with the hydro-mechanical soil properties and the hydrological loading. This paper presents an accessible approach to assess the probability of failure of flood embankments. To allow for transient seepage analysis, the entire hydrograph is modelled in probabilistic terms. The proposed approach is based on the application of the FOSM method to calculate the mean and variance of the Factor of Safety. The main limitation of the FOSM method lies in the a priori assumption of the probability distribution for the Factor of Safety for the calculation of the probability of failure. This limitation is addressed by suggesting a criterion for the selection of the most appropriate probability distribution function based on the application of the Monte Carlo method for a single variable. The approach was successfully validated against a failure case-study on the Adige River in Italy. The application of the proposed approach requires a limited time and computational effort. The method has a clear engineering significance and is accessible to

geotechnical engineers who are not extremely familiar with probability concepts. This advantage makes it a suitable tool for the assessment of probability of failure of flood embankment in routine engineering applications.

2.1 Introduction

Over the last few decades the number of catastrophic flood events has risen all over the world and the trend in such natural disasters is increasing. Escalations in both the frequency and magnitude of flood events can be expected as a result of climate change (Guerreiro, et al., 2018). The annual average economic damage due to flooding in Europe amounted to €4.6 billion in the period 2000 – 2012 and it is expected to increase up to €23.5 billion by 2050 (Jongman, et al., 2014).

Flood embankments are (and will remain) one of the main flood defence measures. In case of failure of flood embankments entire towns can be flooded and consequences can be devastating, both in terms of loss of human lives and economic damages. It is therefore very important to assess the stability of these structures. This process involves many uncertainties, generated by different sources. Natural hazards such as floods are phenomena subjected to random variability in terms of time of occurrence and magnitude. Moreover, soils are materials of natural origin and therefore their physical, hydraulic and mechanical properties exhibit a large natural variability, which generates a significant source of uncertainty. Very often the scarcity of experimental data also adds uncertainty to the characterisation of their hydro-mechanical behaviour. The uncertainty in the hydrological loading (flood) and material properties has to be accounted for and quantified during the process of assessing the stability of flood embankments. As a result, stability analysis has to be carried out using probabilistic approaches.

A first critical aspect in probabilistic assessment of stability of flood embankments is the selection of a probabilistic method. The Monte Carlo method has been extensively applied to slope stability problems, with one of its first applications dating back to 1982 (Tobutt). It requires solving the same ‘deterministic’ problem a number of times, by sampling a random value of the uncertain parameters in each simulation. Its main limitation lies in the number of simulations required to have a sufficiently accurate estimate of the probability of failure. If the number of random variables increases, the number of simulations required for the estimation of the probability of failure increases exponentially; the process becomes more and more time-consuming and computationally demanding and makes the method impractical to use when several random variables need to be taken into account.

This problem can be overcome by using an approximate probabilistic method. The First Order Second Moment method has often been suggested as a probabilistic method for use in routine geotechnical engineering design (Duncan, 2000) because it requires a low computational effort and is less complex than other probabilistic methods. However, the application of the FOSM method on its own does not allow the direct calculation of the probability of failure, because it only provides information about the mean and variance of the Factor of Safety. In order to calculate the probability of failure, the function representing the probability distribution has to be assumed a priori and this represents the main limitation of the method. Normal or LogNormal distributions have been assumed for the Factor of Safety in the majority of slope stability studies. Duncan (2000) recommends using a LogNormal distribution, although some degree of personal judgement was involved in this assumption. Baecher and Christian (2005) suggest using a Normal distribution, which is assumed to err on the safe side and, hence, overestimate the probability of failure. It is however recognised that the assumed shape of the probability distribution may have a significant influence on the computed probability of failure, especially when an estimation of very low values of probability is required (El-Ramly, et al., 2002).

A second critical aspect in the probabilistic assessment of stability of flood embankments involves the identification of the relevant random variables. It has been recognised that the uncertainty of hydraulic and mechanical soil properties needs to be taken into account (Malkawi A.I.H., 2000; Gui, et al., 2000; El-Ramly, et al., 2002; Suchomel & Mašín, 2010). However, the source of uncertainty in the hydrological loading has been neglected in most cases with only a few exceptions (Moellmann, et al., 2011). The hydrological loading needs to be characterised via its entire hydrograph (Tracy, et al., 2016), i.e. time-dependent hydrological loading, for the case where water through-flow is analysed under transient conditions (Pozzato, et al., 2014). This poses a further challenge as the probabilistic distributions are generally available only for the peak river level. Probabilistic distributions of other variables describing the hydrograph, e.g. flood duration or the rate of increase of river level, should be considered in the probabilistic analysis.

The paper presents an accessible approach to assess the probability of failure of flood embankments taking into account transient water flow. The approach is based on the FOSM method and includes a probabilistic model for a time-dependent hydrological loading. In order to overcome the main limitation of the FOSM method about the a priori assumption of the probability distribution of the Factor of Safety, the paper also develops a criterion that can be adopted for the selection of the appropriate distribution. This approach has been validated against a case study in order to show that results are consistent and in good agreement with the observed probability of failure. The approach is 'accessible' in the sense that it can be easily applied by engineers who have a traditionally deterministic background, thus bridging the gap between the two disciplines of geotechnical engineering and statistics.

2.2 The case study

The flood embankment considered in the case study is located in the Adige Valley near the town of Bolzano in North-Eastern Italy. The Adige River is the second longest river in Italy and it flows from the Alps through most of North-Eastern Italy. In the lower Adige Valley, south of Bolzano, the river flows in direction South-West. Flood embankments were built at the end of 19th century (in the periods 1817–1826 and 1879–1885) to straighten the original meandering path of the Adige River in the glacial valley (Simeoni, et al., 2014).

In the present study, the probability of failure has been assessed for the embankment segment located near the village of San Floriano at km 122.248 of the chainage (Pozzato, et al., 2014). This segment has been chosen because instability in the form of a scarp was observed during the flood in July 1981 (Zwanenburg, et al.). This segment of the embankment was built between 1860 and 1890 (Werth, 2003) and this was the only failure observed in this location since construction. Having observed one failure in about 100 years, the expected probability of failure is of the order of 1% per year.

2.2.1 Soil profile

The soil profile of the cross-section representative of the San Floriano segment is shown in Figure 2.1. The soil layer boundaries have been identified from visual inspection of borehole samples and dynamic probing heavy (DPH) tests (*Chapter 3*).

These have been confirmed by the grain size distributions of samples collected from the identified homogeneous layers shown in Figure 2.1. The crest of the embankment is about 8.2 m high from the riverbed and about 4.2 m high from the ground surface on the landside. The embankment core is made of silty sand and is covered by a 1m thick gravelly shell. The embankment overlies a 7 m thick foundation layer of sandy material of fluvial origin, which is a trace of the ancient riverbed where the Adige River flowed before the construction of the embankment. The deepest foundation layer is constituted of deposits of sand of lacustrine origin (*Chapter 3*).

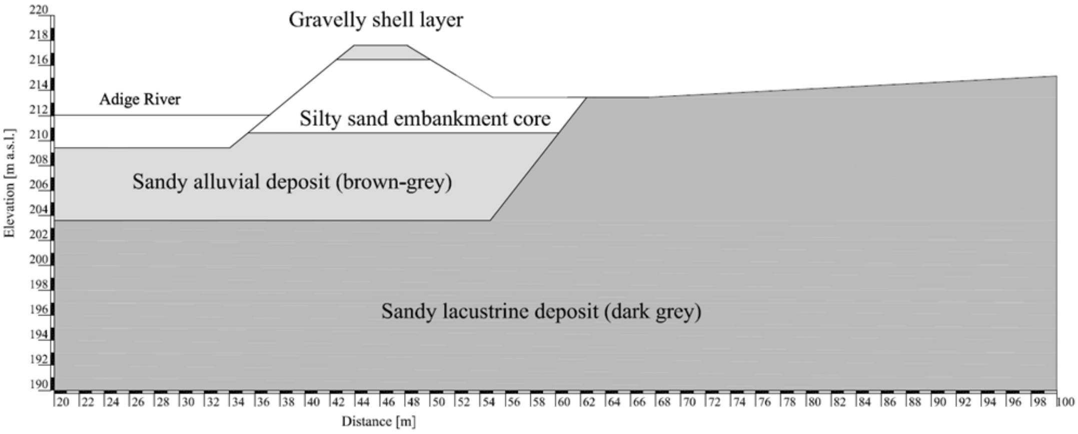

Figure 2.1. Geometry and soil profile of the embankment in San Floriano in 1981.

2.2.2 Hydraulic and mechanical characterisation

The hydraulic characterisation of the various materials was carried out by considering separately the saturated and the unsaturated range. The saturated hydraulic conductivity and the anisotropy ratio were derived from inverse analysis of field piezometer and tensiometer measurements for the sandy fluvial foundation and the embankment material, from laboratory tests for the gravelly shell and the lacustrine foundation (*Chapter 3*). A summary is reported in Table 2.1.

	$k_{Horizontal}$ [m/s]	$k_{Vertical}/k_{Horizontal}$
Gravelly shell	8.5E-04	1
Embankment core	2.0E-06	1
Fluvial foundation	4.0E-03	0.1
Lacustrine foundation	2.0E-05	0.1

Table 2.1. Saturated hydraulic conductivity of materials.

To characterise the unsaturated behaviour of the embankment sandy silt, the water retention curve was derived by fitting the van Genuchten model for water retention (Van Genuchten, 1980) to the water retention data obtained in the laboratory on samples collected from the field (*Chapter 3*). The equation of the water retention function can be written as follows (Eq. 2.1):

$$S_e = \frac{\theta - \theta_{res}}{\theta_{sat} - \theta_{res}} = \frac{1}{(1 + (\alpha s)^n)^m} \qquad \left[\mathrm{m} = 1 - \frac{1}{\mathrm{n}}\right] \qquad \textbf{\textit{Eq. 2.1}}$$

where s is the suction, θ_{res} and θ_{sat} are the residual volumetric water content and the saturated volumetric water content respectively, and α and n are soil parameters. The α parameter is related to the largest pore size in the material and is associated with the air-entry value, while n depends on the pore size distribution and controls the slope of the water retention curve (Van Genuchten, 1980) The relative hydraulic conductivity was derived from the water retention curve using the Van Genuchten model for the hydraulic conductivity (Van Genuchten, 1980) as follows (Eq. 2.2):

$$k = k_{sat} \cdot k_{rel} = k_{sat} \cdot {S_e}^{-0.5} \left(1 - \left(1 - {S_e}^{\frac{1}{m}}\right)^m\right)^2 \qquad \textbf{\textit{Eq. 2.2}}$$

The mechanical characterisation of the materials was carried out in terms of shear strength only (the material was assumed to have a rigid-perfectly plastic behaviour).

The shear strength was determined via direct shear tests on the embankment silty sand (*Chapter 3*) and the gravel (Pozzato, et al., 2014).

The hydro-mechanical properties of the embankment are critical variables in the assessment of the stability of the embankment. This includes the hydraulic properties in the unsaturated range, represented by the water retention and relative hydraulic conductivity curves. Moreover, the saturated hydraulic conductivity of the foundation layers plays a significant role in the seepage process and can influence the values of pore water pressure in the embankment, especially on the toe of the landside slope. This in turn affects the shear strength and therefore the results of the stability analysis. However, the slip surfaces are not deep enough to involve the foundation layers in the failure mechanism. The mechanical properties of the foundation layers have therefore been assumed as deterministic parameters, with a friction angle equal to 33^0 for both materials. The gravelly shell layer is only marginally involved in the seepage process and stability analysis; for this reason the hydro-mechanical properties of the gravel have also been considered as deterministic parameters.

In summary, the following probabilistic parameters have been identified as critical material properties to be used in the assessment of the probability of failure of the embankment:

- Shear strength, i.e. friction angle φ' of the embankment silty sand (being the cohesion equal to 0 in this case);
- Saturated hydraulic conductivity of the embankment silty sand, fluvial foundation layer and lacustrine foundation layer;

- Slope and air-entry value of water retention curve of the embankment silty sand, summarised by the α and n parameters of Van Genuchten model.

In a probabilistic approach each random variable has to be described by a probability distribution. Since the experimental data are not sufficient to derive the probability distribution for each variable of interest, a different approach has to be devised. One approach (Duncan, 2000) is to use estimates based on published values for similar soil types.

A LogNormal distribution has been assumed in this work for all the soil properties, in agreement with many previous studies in the literature (Arnold & Hicks, 2011; Gui, et al., 2000; Zhang, et al., 2005). Such a distribution is frequently selected because most physical properties cannot have negative values and this is consistently represented by the LogNormal distribution (Uzielli, et al., 2007). The values obtained in the experimental characterisation have been assumed as mean values for each variable, while a reference value for the standard deviation has been inferred from the literature in terms of coefficients of variation (COV), defined as the ratio of the standard deviation to the mean value. The coefficients of variation of the friction angle and the saturated hydraulic conductivity were derived from Otálvaro et al. (2013), whereas the coefficients of variation of water retention parameters were derived from Likos et al. (2014). A summary of all the probability distribution parameters for each material property of interest is reported in Table 2.2.

The soil was assumed to be homogeneous within each layer, i.e. the spatial variability of material properties was neglected. The amount of experimental data did not allow developing a more detailed probabilistic model which could account for spatial heterogeneity of material properties.

	Variable	Distribution	μ	σ
Embankment hydro-mechanical properties	**φ' [^{0}]**	LogNormal	28.9	1.73
	k_{emb} [m/s]	LogNormal	2.0E-06	1.3E-06
	n	LogNormal	1.438	0.122
	α [1/kPa]	LogNormal	0.07	0.03
Foundation layers	**k_{flu} [m/s]**	LogNormal	4.0E-03	2.5E-03
	k_{lac} [m/s]	LogNormal	2.0E-05	1.3E-05

Table 2.2. Probability distribution of friction angle, saturated hydraulic conductivity and water retention curve parameters.

2.2.3 Hydrological loading

When considering steady-state flow conditions in the stability analysis of flood embankments, only the maximum river level is taken into account to describe the hydrological loading. To analyse transient-state water flow, a time-dependent loading has to be taken into account, and aspects like duration or shape of the hydrograph have to be considered.

In this study, the hydrographs of the 30 flood events recorded between 1977 and 2014 in San Floriano have been analysed (Amabile, et al., 2016). The key variables describing the flood event have been defined as shown in Figure 2.2, where:

- h_{peak} is the maximum river level during the flood event;
- h_{start} is the initial river level marking the beginning of the flood event;
- t_{peak} is the time elapsed between the beginning of the flood event (h_{start}) and the maximum river level (h_{peak});
- β is the shape parameter governing the falling limb of the hydrograph.

The “typical” hydrograph was divided in two parts, with the rising limb (before the peak) described by a linear function as shown in Eq. 2.3 and the falling limb (after the peak) characterised by a power decay as shown in Eq. 2.4 (Amabile, et al., 2016):

$$h = h_{start} + \frac{h_{peak} - h_{start}}{t_{peak}} t \quad (t \leq t_{peak})$$

Eq. 2.3

$$h = h_{peak} * \left(\frac{t}{t_{peak}}\right)^{(-\beta)} \qquad (t > t_{peak})$$

Eq. 2.4

The least square error between the predicted and recorded hydrograph was minimised to find the best-fitting values of h_{peak}, t_{peak}, h_{start} and β for each hydrograph. These values were then used to derive the joint probability distribution of these four hydrograph parameters.

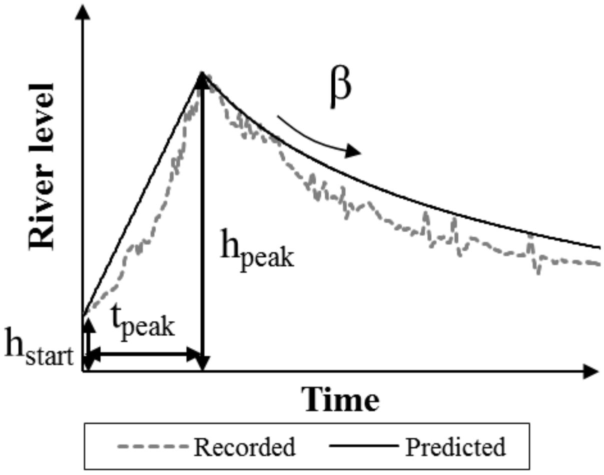

Figure 2.2. Representation of the hydrograph and key variables.

Pearson's correlation test has revealed a correlation between β and the other variables. This has been derived by means of a multivariate regression model as shown in Eq. 2.5 (*Chapter 3*):

$$\beta = 0.0009407 * h_{peak}[cm] - 0.001062 * h_{start}[cm] + 0.1005 * t_{peak}[d]$$

Eq. 2.5

The most appropriate probability distribution for the remaining independent variables (h_{peak}, h_{start}, and t_{peak}) was obtained via the maximum likelihood estimation. The

LogNormal distribution exhibited the best fitting for all the variables. Means and standard deviations are reported in Table 2.3 (*Chapter 3*).

Variable	Distribution Type	μ	σ
h_{peak} [cm]	LogNormal	580	45.6
h_{start} [cm]	LogNormal	354	46.4
t_{peak} [d]	LogNormal	1.083	0.354

Table 2.3. Probability distribution of key variables for the hydrological loading.

The flood intermittence, i.e. the time interval between subsequent flood events, is characterised by an average value of 1.26 years. This means that flood events occur every 1.26 years on average or, equivalently, the average frequency of flood events λ_f is 0.80 events per year (Eq. 2.6):

$$\lambda_f = \frac{1}{intermittence} = 0.80\, event * year^{-1} \qquad \textbf{\textit{Eq. 2.6}}$$

Flood intermittence was not considered as an hydrological loading random variable since it is significantly greater than the time of dissipation of the pore-water pressures generated by the flood event (in the range of a few days).

2.2.4 Seepage and slope stability analysis

The distribution of pore water pressure in the embankment during the flood event was evaluated via a transient-state seepage analysis. The finite element software SEEP/W (GEO-SLOPE, 2004) was used for this purpose as it takes into account flow in unsaturated soils.

Boundary conditions for the hydraulic model were set as shown in Figure 2.3, while the initial condition was obtained from a steady-state pore-water pressure distribution associated with the initial river level. The duration of the seepage analysis was set equal to four days with a time step of one hour. More details about the numerical model can be found in *Chapter 3*.

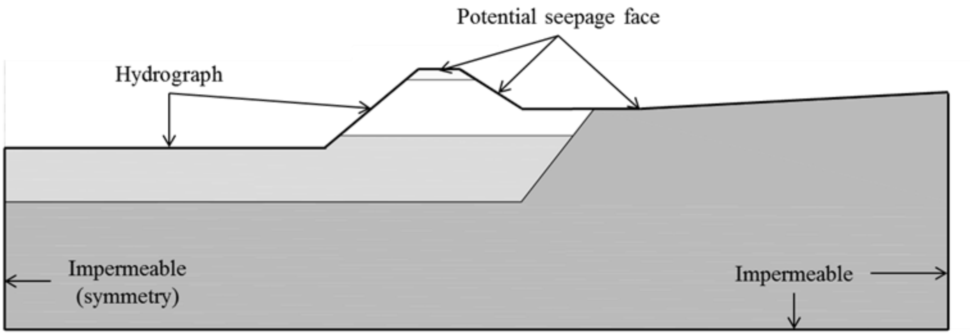

Figure 2.3. Boundary conditions applied in the transient seepage analysis.

Stability analysis was carried out using Bishop’s simplified method (Bishop, 1955) using the software SLOPE/W (GEO-SLOPE, 2004). Pore-water pressure values calculated by the software SEEP/W were used in the stability analysis to calculate the value of the Factor of Safety over the duration of the flood event. The unsaturated shear strength model implemented by the software is based on the water retention curve of the material according to Vanapalli, et al. (1996); for the stability analysis the residual volumetric water content was assumed to be equal to 10% of the saturated volumetric water content.

2.3 FOSM-based approach

2.3.1 First Order Second Moment Method

The First Order Second Moment (FOSM) method is used to determine the mean and variance of a performance function $Y=Y[X_1, X_2,\dots, X_n]$ with input random variables $X_1,\dots,X_n$. It is based on a Taylor’s series expansion of the performance function Y around its mean value. The name derives from the fact that only first order terms of the series are retained and only the first and second moment, i.e. the mean and variance, are considered. Eq. 2.7 and Eq. 2.8 give respectively the mean $\mu[Y]$ and the variance $\sigma^2[Y]$ of the performance function for the case of independent input variables:

$$\mu[Y] \cong Y(\mu[X_1], \mu[X_2], \ldots, \mu[X_n]) \tag{Eq. 2.7}$$

$$\sigma^2[Y] \cong \sum_1^n \left(\frac{\partial Y}{\partial X_i}\right)^2 \sigma^2[X_i] \tag{Eq. 2.8}$$

The mean and variance can be used to calculate the probability corresponding to any values of the performance function Y, provided that an assumption is made about its probability distribution function (Wolff, et al., 2004). If the input variables are not independent, correlation has to be considered when calculating the variance $\sigma^2[Y]$.

In the application to stability analysis the performance function is represented by the Factor of Safety; in most cases the analytical calculation of the partial derivatives in Eq. 2.8 may be complex if not impossible, so they can be estimated numerically as incremental ratios using a finite difference approach (Eq. 2.9):

$$\frac{\partial FS}{\partial X_i} = \frac{FS(\mu[X_i] + \Delta X_i) - FS(\mu[X_i] - \Delta X_i)}{2\Delta X_i} \tag{Eq. 2.9}$$

The value of the increments ΔX_i is commonly taken equal to the standard deviation for each variable X_i in order to analyse the linearity of the performance function in the range of most likely values (Wolff, et al., 2004).

2.3.2 Mean and Variance of Factor of Safety

The application of the FOSM method to the slope stability analysis of a flood embankment is first discussed for a problem with a single input variable h_{peak} for illustrative purposes (Figure 2.4).

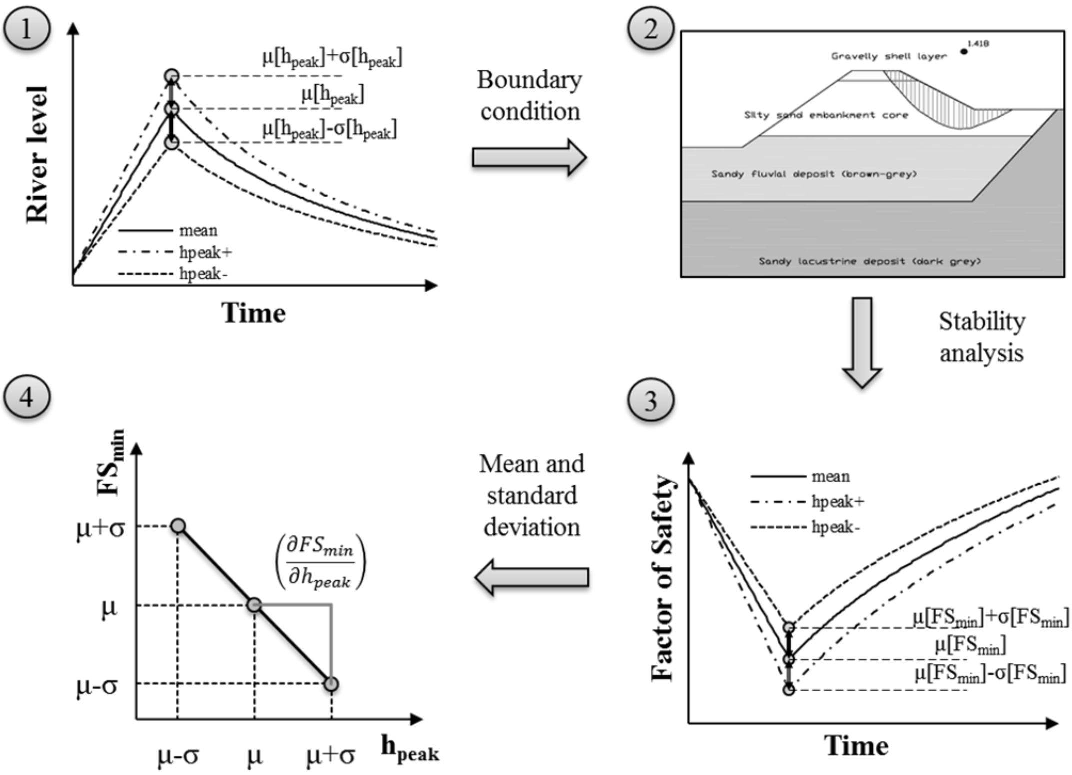

Figure 2.4. Graphical representation of FOSM method applied to stability analysis for a single input variable h_{peak}.

The uncertainty in the assessment of the input variable h_{peak} is taken into account by considering a range of likely values. Only three significant values of h_{peak} are taken into account: the mean value $\mu[h_{peak}]$ and the extremes of the range defined by adding and subtracting one standard deviation to the mean value ($\mu[h_{peak}]-\sigma[h_{peak}]$, $\mu[h_{peak}]+\sigma[h_{peak}]$). These values are used to generate three hydrographs; all the other key variables defined for the hydrograph (the initial river level h_{start} and the time t_{peak}) are taken with their mean values. The three hydrographs are applied as boundary conditions in as many transient-state seepage analyses and the resulting pore-water pressure profiles are subsequently used in the stability analyses to calculate the variation of Factor of Safety over time for the entire duration of the flood event.

The minimum Factor of Safety FS_{min} over time for each of the three stability analyses is identified. Each value of FS_{min} in the output corresponds to a value of h_{peak} in the input; in other words the Factor of Safety is calculated in three points, which correspond to the three significant values of h_{peak} taken into account. For a single variable the three points are associated with the mean value $\mu[FS_{min}]$ and the extremes of the range of Factor of Safety $\mu[FS_{min}]-\sigma[FS_{min}]$ and $\mu[FS_{min}]+\sigma[FS_{min}]$ respectively, as shown in step 3 in Figure 2.4.

The mean value of the Factor of Safety $\mu[FS_{min}]$ is associated with the mean value of the input variable $\mu[h_{peak}]$ (Eq. 2.10 and step 4 in Figure 2.4):

$$\mu[FS_{min}] \cong FS_{min}\left(\mu\left[h_{peak}\right]\right)$$

Eq. 2.10

The standard deviation of the Factor of Safety $\sigma[FS_{min}]$ is associated with the standard deviation of the input variable $\sigma[h_{peak}]$ (Eq. 2.11 and step 4 in Figure 2.4):

$$\sigma[FS_{min}] \cong \sqrt{\left(\frac{\partial FS_{min}}{\partial h_{peak}}\right)^2 \sigma^2\left[h_{peak}\right]} = \left(\frac{\partial FS_{min}}{\partial h_{peak}}\right)\sigma\left[h_{peak}\right]$$

Eq. 2.11

The derivative $\left(\frac{\partial FS_{min}}{\partial h_{peak}}\right)$ in Eq. 2.11 is represented graphically by the slope of the line shown in step 4 in Figure 2.4.

The method illustrated above for a single variable can be easily extended to the nine independent input variables considered in this study. For each input variable the Factor of Safety has been calculated in three points, one corresponding to the mean value μ and two corresponding to the mean value plus and minus one standard deviation ($\mu+\sigma$, $\mu-\sigma$) of the input variable. A summary is reported in Table 2.4.

	Variable	**Distribution**	**μ**	**σ**	**μ+σ**	**μ-σ**
Hydrological loading	**h_{peak} [cm]**	LogNormal	580	45.4	625.4	534.6
	h_{start} [cm]	LogNormal	354	46.0	400.0	308.0
	t_{peak} [d]	LogNormal	1.083	0.334	1.416	0.749
Embankment hydro-mechanical properties	**φ' [^{0}]**	LogNormal	28.9	1.73	30.6	27.2
	k_{emb} [m/s]	LogNormal	2.0E-06	1.3E-06	3.2E-06	6.9E-07
	n	LogNormal	1.438	0.122	1.560	1.316
	α [1/kPa]	LogNormal	0.07	0.03	0.10	0.03
Foundation layers	**k_{flu} [m/s]**	LogNormal	4.0E-03	2.5E-03	6.4E-03	1.4E-03
	k_{lac} [m/s]	LogNormal	2.0E-05	1.3E-05	3.2E-05	6.9E-06

Table 2.4. Values of input variables for the calculation of Factor of Safety in the FOSM method.

The number of simulations required for the calculation of the mean and standard deviation of the Factor of Safety is $2v+1=19$, where v is the number of independent input variables. The first simulation is used to calculate the mean value of the Factor of Safety, starting from the mean values of all the input variables (this corresponds to a routine deterministic analysis). The following $2v$ simulations are performed by increasing or decreasing one variable at a time, while all the others are kept constant and equal to their mean value. This allows evaluating the Factor of Safety over a range of likely values, in order to calculate its standard deviation. A summary of the combinations of values of the input variables for each simulation is reported in Table 2.5, with the corresponding value of minimum Factor of Safety FS_{min}.

It should be noted that a single slip surface has been considered in all the combinations of stability analysis when applying the FOSM method (Phoon, 2008). The critical slip surface resulting in the minimum value of Factor of Safety in the first simulation, i.e. the deterministic critical slip surface, has been taken into account for all subsequent analyses. This assumption does not constitute a major limitation in this study as the same critical slip surface has been observed in most of the other combinations.

simulation		h_{peak} [cm]	h_{start} [cm]	t_{peak} [d]	φ' $[^0]$	k_{emb} [m/s]	n	α $[kPa^{-1}]$	k_{flu} [m/s]	k_{lac} [m/s]	FS_{min}
1	*mean*	580	354	1.083	28.9	2E-06	1.438	0.07	4E-03	2E-05	1.418
2	$h_{peak}+$	625	354	1.083	28.9	2E-06	1.438	0.07	4E-03	2E-05	1.532
3	$h_{peak}-$	535	354	1.083	28.9	2E-06	1.438	0.07	4E-03	2E-05	1.311
4	$h_{start}+$	580	400	1.083	28.9	2E-06	1.438	0.07	4E-03	2E-05	1.479
5	$h_{start}-$	580	308	1.083	28.9	2E-06	1.438	0.07	4E-03	2E-05	1.324
6	$t_{rise}+$	580	354	1.417	28.9	2E-06	1.438	0.07	4E-03	2E-05	1.462
7	$t_{rise}-$	580	354	0.750	28.9	2E-06	1.438	0.07	4E-03	2E-05	1.401
8	φ'^{+}	580	354	1.083	30.6	2E-06	1.438	0.07	4E-03	2E-05	1.344
9	φ'^{-}	580	354	1.083	27.2	2E-06	1.438	0.07	4E-03	2E-05	1.519
10	k_{emb}^{+}	580	354	1.083	28.9	3E-06	1.438	0.07	4E-03	2E-05	1.603
11	k_{emb}^{-}	580	354	1.083	28.9	7E-07	1.438	0.07	4E-03	2E-05	1.388
12	n^{+}	580	354	1.083	28.9	2E-06	1.560	0.07	4E-03	2E-05	1.420
13	n^{-}	580	354	1.083	28.9	2E-06	1.316	0.07	4E-03	2E-05	1.420
14	α^{+}	580	354	1.083	28.9	2E-06	1.438	0.10	4E-03	2E-05	1.396
15	α^{-}	580	354	1.083	28.9	2E-06	1.438	0.03	4E-03	2E-05	1.460
16	k_{flu}^{+}	580	354	1.083	28.9	2E-06	1.438	0.07	6E-03	2E-05	1.479
17	k_{flu}^{-}	580	354	1.083	28.9	2E-06	1.438	0.07	1E-03	2E-05	1.405
18	k_{lac}^{+}	580	354	1.083	28.9	2E-06	1.438	0.07	4E-03	3E-05	1.412
19	k_{lac}^{-}	580	354	1.083	28.9	2E-06	1.438	0.07	4E-03	7E-06	1.424

Table 2.5. Values of input variables X_i and minimum Factor of Safety FS_{min} obtained in the simulations for the application of FOSM method. Shaded values represent the increased / decreased variables in each simulation.

The variation of the minimum Factor of Safety with respect to all the input variables is reported in Figure 2.5. The centre point corresponds to the mean value of the Factor of Safety FS_{min} generated by the mean values of all input variables (Eq. 2.12). This would be the value obtained from a deterministic analysis.

$$\mu[FS_{min}] \cong FS_{min}\begin{pmatrix} \mu[h_{peak}], \mu[h_{start}], \mu[t_{peak}], \mu[\varphi'], \mu[k_{emb}], \\ \mu[n], \mu[\alpha], \mu[k_{flu}], \mu[k_{lac}] \end{pmatrix} \qquad \textbf{\textit{Eq. 2.12}}$$

The slopes of each line in Figure 2.5 represent graphically the partial derivatives contributing to the variance of the Factor of Safety (Eq. 2.13). The Factor of Safety is not highly non-linear with respect to the input variables, so it can be approximated by a straight line without a large error. The approximation of the Factor of Safety with a straight line is implicit in the FOSM method because only first order terms are considered in the Taylor series' expansion of the Factor of Safety.

$$\begin{aligned}\sigma^2[FS_{min}] \cong {} & \left(\frac{\partial FS_{min}}{\partial h_{peak}}\right)^2 \sigma^2[h_{peak}] + \left(\frac{\partial FS_{min}}{\partial h_{start}}\right)^2 \sigma^2[h_{start}] + \left(\frac{\partial FS_{min}}{\partial t_{peak}}\right)^2 \sigma^2[t_{peak}] \\ & + \left(\frac{\partial FS_{min}}{\partial k_{emb}}\right)^2 \sigma^2[k_{emb}] + \left(\frac{\partial FS_{min}}{\partial \varphi'}\right)^2 \sigma^2[\varphi'] + \left(\frac{\partial FS_{min}}{\partial n}\right)^2 \sigma^2[n] \\ & + \left(\frac{\partial FS_{min}}{\partial \alpha}\right)^2 \sigma^2[\alpha] + \left(\frac{\partial FS_{min}}{\partial k_{flu}}\right)^2 \sigma^2[k_{flu}] + \left(\frac{\partial FS_{min}}{\partial k_{lac}}\right)^2 \sigma^2[k_{lac}]\end{aligned} \qquad \textbf{\textit{Eq. 2.13}}$$

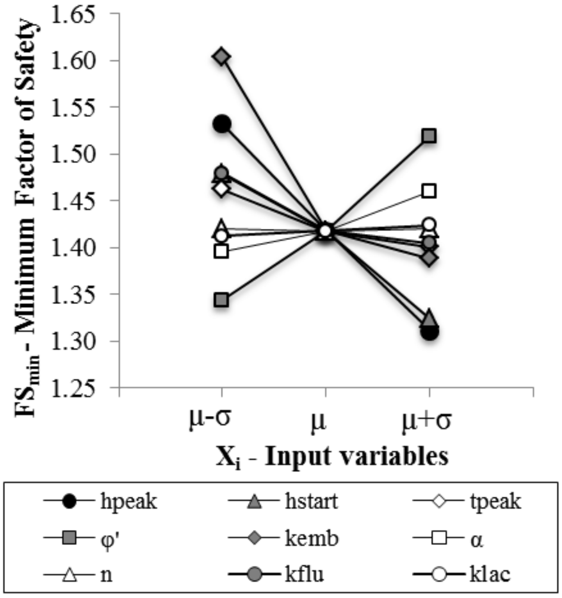

Figure 2.5. Variation of minimum Factor of Safety *FS_{min}* with respect to the input variables *X_i*.

The values of the mean and the variance of the Factor of Safety obtained from the analysis are reported in Table 2.6.

$\mu[FS_{min}]$	**1.418**
$\sigma^2[FS_{min}]$	**0.041**

Table 2.6. Mean and variance of minimum Factor of Safety *FS_{min}*.

The FOSM method also allows quantifying the relative contribution of each variable $w[X_i]$ to the variability of the Factor of Safety as shown in Eq. 2.14 and Figure 2.6.

$$w[X_i] = \frac{\left(\frac{\partial FS_{min}}{\partial X_i}\right)^2 \sigma^2[X_i]}{\sigma^2[FS_{min}]} \qquad \textit{Eq. 2.14}$$

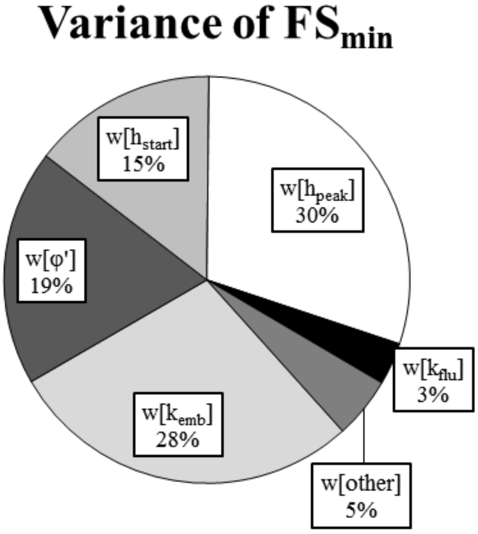

Figure 2.6. Contribution of each input variable to the variability of minimum Factor of Safety *FS_{min}*.

The results show that the maximum river level h_{peak} has the greatest influence on the variability of the Factor of Safety. This can be explained by the fact that the saturated hydraulic conductivity of the materials that constitute the embankment and especially the sandy fluvial deposit is relatively high. The pore-water pressures therefore respond very quickly to an increase in river level, in turn generating a very quick drop in shear strength and, hence, Factor of Safety.

This is further highlighted by the fact that the minimum value of Factor of Safety FS_{min} is attained when the maximum river level is reached for most combinations. A significant exception is represented by the combination k_{emb-} as shown in Figure 2.7. In this combination the saturated hydraulic conductivity of the embankment is decreased (μ-σ) and the minimum value of Factor of Safety FS_{min} is attained some time later with respect to the maximum river level, because the lower hydraulic conductivity generates a delay in the hydraulic response of the material. This also happens in the combination α^+ where the Van Genuchten parameter α is increased, because increasing α translates in a decrease in the air entry value in the water retention and relative hydraulic conductivity curves of the material. The decrease in the air entry value narrows the range of suction values in which the material behaves as saturated and is therefore characterised by its maximum value of hydraulic conductivity.

The variables n and α seem to have little influence on the variability of the Factor of Safety. This result is in agreement with the results of previous studies (Calamak & Yanmaz, 2017), which proved that the variability in the parameters α and n governing the water retention curve does not have a significant effect on the transient water flow and concluded that treating them as deterministic values does not introduce a great error in the seepage analysis.

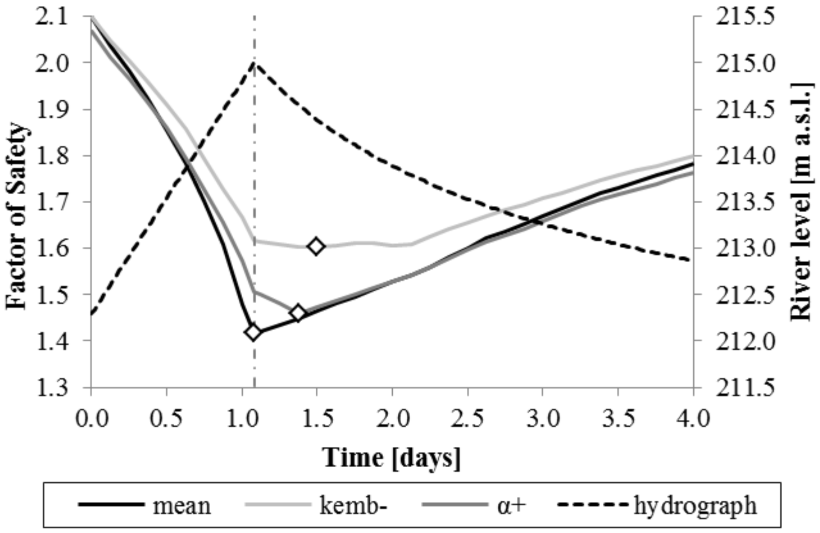

Figure 2.7. Factor of Safety over time for the simulations *mean*, k_{emb}^{-} and α^{+} compared to the hydrograph.

2.3.3 Selection of distribution function for the Factor of Safety

The probability of failure of the embankment corresponds to the probability of observing a Factor of Safety FS_{min} lower than or equal to unity. In order to calculate the probability of failure of the embankment, the mean and standard deviation of the minimum Factor of Safety FS_{min} are not sufficient; a function has to be adopted for the probability distribution of the Factor of Safety. Previous studies provide limited indication about how to select the probability distribution, with most authors adopting Normal or LogNormal distributions despite little evidence supporting these assumptions. This section presents a criterion to select the optimal distribution for the Factor of Safety, based on the application of the Monte Carlo method with a single input variable.

The Monte Carlo method is based on the repeated sampling of random numbers (Zio & Marseguerra, 2002). In the application of the Monte Carlo method a set of random values of the input variable X_i are used. These values are obtained by generating a set of random numbers between 0 and 1, which can be linked to values of the input variable X_i via its probability distribution. Every random value of the input variable X_i is used to generate a value of the Factor of Safety, and the process is repeated many times in order to cover the range of possible outcomes. All the resulting values of the Factor of Safety are then aggregated to obtain its empirical probability distribution, which can then be fitted with the most appropriate probability distribution function. The maximum river level h_{peak} has been considered as the only input variable for the Monte Carlo method because it has the greatest influence on the variability of the Factor of Safety FS_{min} (as observed from the FOSM method).

The application of Monte Carlo method is schematically illustrated in Figure 2.8.

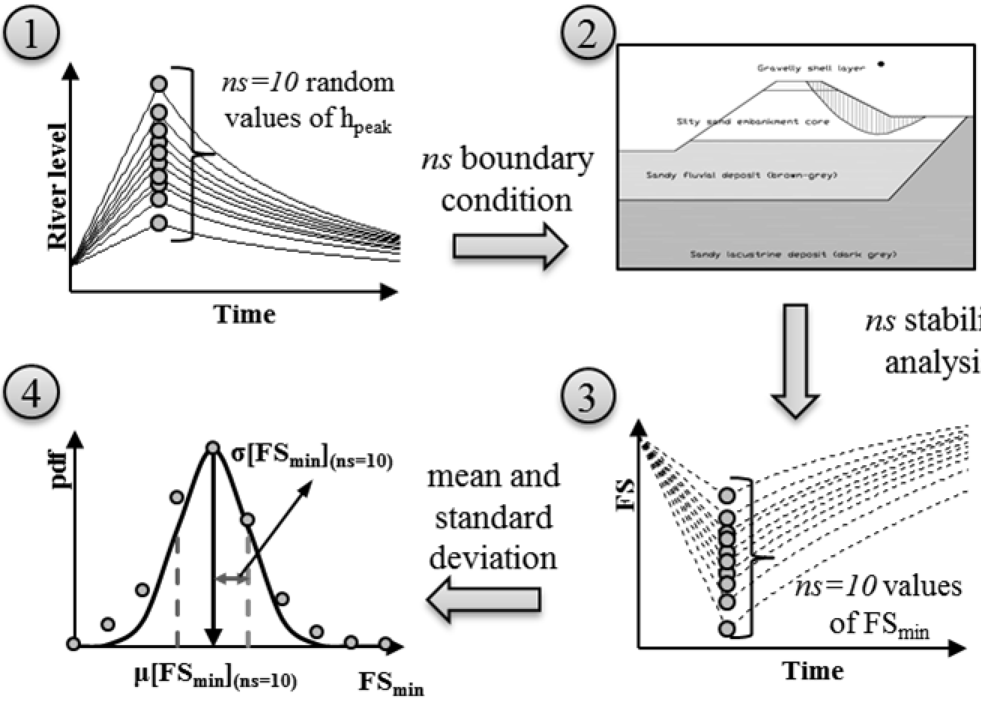

Figure 2.8. Graphical representation of Monte Carlo method applied to stability analysis for a single input variable h_{peak}.

A number *ns* of random values of the input variable h_{peak} have been sampled from its probability distribution and as many hydrographs have been generated; since the variability of the other key variables for the hydrological loading (i.e. h_{start} and t_{peak}) is neglected these variables are kept constant and equal to their mean values for the definition of all the hydrographs. Every random hydrograph generated in this way represents the hydrological loading, i.e. the boundary condition on the riverside, for one transient-state seepage analysis; the distribution of pore water pressure derived from each seepage analysis is considered in a corresponding stability analysis to calculate the variation of the Factor of Safety over time. In each stability analysis the minimum value of the Factor of Safety FS_{min} is identified. This process is repeated *ns* times, thus calculating *ns* values of FS_{min} that correspond to as many randomly sampled values of h_{peak}. All the resulting values of FS_{min} have been analysed to calculate their mean $\mu[FS_{min}]$ and variance $\sigma^2[FS_{min}]$.

The values of mean and variance of the minimum Factor of Safety FS_{min} have been calculated for increasing numbers of simulations in order to determine the appropriate number of simulations *ns*, as shown in Figure 2.9. As a first approximation, *ns* = 1000 simulations have been run. The values of $\mu[FS_{min}]$ and $\sigma^2[FS_{min}]$ appear to reasonably level off between 800 and 1000 simulations. The number *ns* = 1000 has then been selected as the appropriate number of simulations.

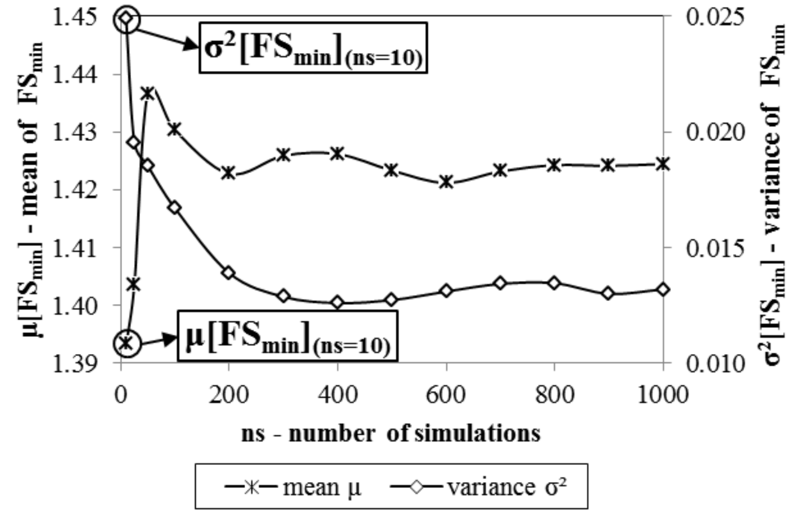

Figure 2.9. Mean *$\mu[FS_{min}]$* and variance *$\sigma^2[FS_{min}]$* of the minimum Factor of Safety *FS_{min}* for increasing number of simulations *ns* in the application of Monte Carlo method.

It is convenient to first illustrate the concept behind the proposed method in a qualitative fashion (Figure 2.10). All the values of FS_{min} obtained from the *ns* simulations have been used to derive its empirical cumulative distribution, which can be represented qualitatively as a step function as shown in Figure 2.10a. For every value of the Factor of Safety on the horizontal axis, the vertical axis shows the probability to have a Factor of Safety FS_{min} lower than or equal to that value. The probability of failure corresponds to the probability of having a Factor of Safety FS_{min} lower than or equal to unity; therefore the empirical probability of failure can be read on the vertical axis from the step curve in the point corresponding to a value of FS_{min} equal to one.

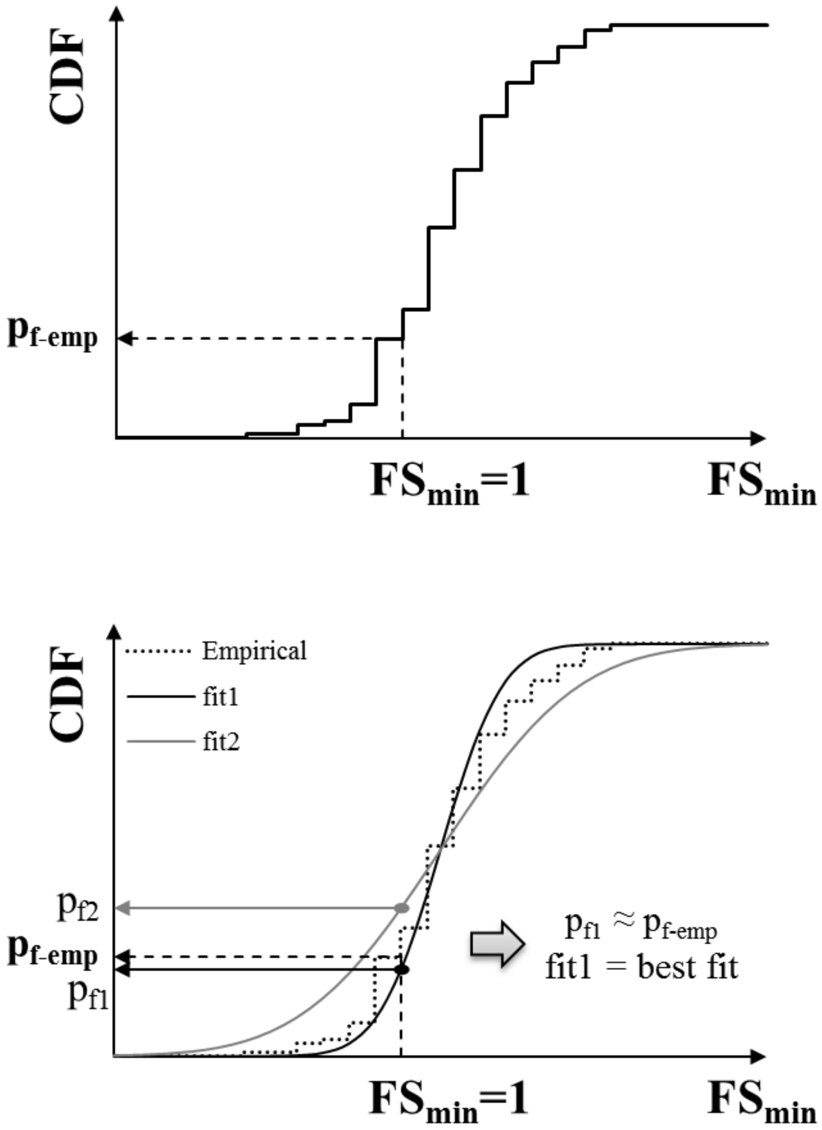

Figure 2.10. Criterion to select the most appropriate probability distribution function by (a) deriving the empirical probability of failure and (b) comparing the values of the probability of failure from different distributions.

Different probability distribution functions are then fitted to the empirical distribution function using maximum likelihood estimates. For each tested probability distribution function the probability of failure is calculated and its value is compared to the empirical probability of failure (Figure 2.10b). The probability distribution function giving a value of probability of failure closer to the empirical probability of failure is selected as the most appropriate to describe the distribution of the Factor of Safety FS_{min}.

In this study, seven different probability distribution functions have been tested and used to calculate the probability of failure (Table 2.7). The probability of failure associated with each probability distribution function has been calculated for increasing number of simulations *ns* and compared to the empirical probability of failure as shown in Figure 2.11.

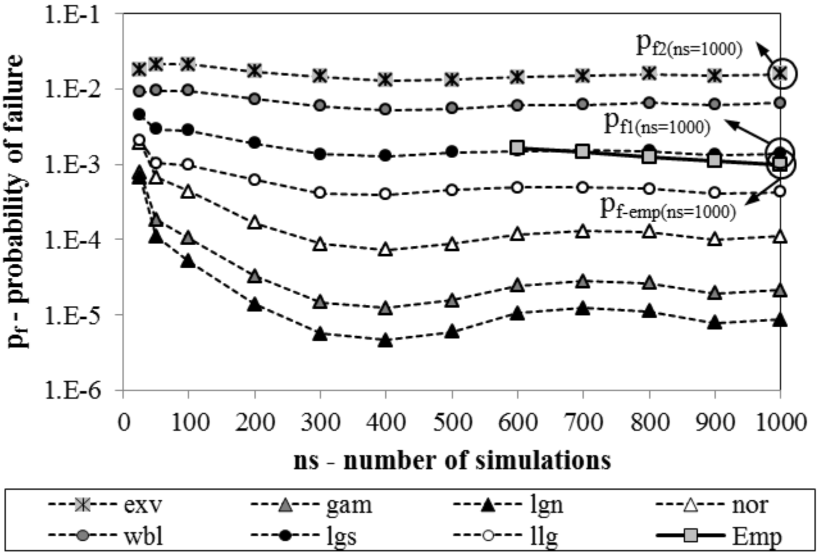

Figure 2.11. Probability of failure for increasing number of simulations *ns* obtained from different probability distribution functions compared to the empirical probability of failure.

It should be noted that the empirical probability of failure is only shown for a number of simulations greater than 600. This is because none of the first 600 stability analyses resulted in a value of FS_{min} lower than or equal to unity. It should also be noted that the very low value obtained for the empirical probability of failure is biased by the fact that only a single random variable is considered. If the variability of the other random variables was included in the Monte Carlo simulation, a higher value of the probability of failure would be expected. However, this is extremely hard to verify due to the prohibitively high number of simulations to run.

When comparing the performance of the tested probability distribution functions in Figure 2.11, the probability of failure calculated from the Logistic distribution has consistently shown the best agreement with the empirical probability of failure for all the values of *ns*; therefore the Logistic distribution has been selected as the most appropriate to assume for the distribution of FS_{min} to calculate the probability of failure of the embankment.

Distribution	**Symbol**
Extreme value	exv
Gamma	gam
Weibull	wbl
Logistic	lgs
LogNormal	lgn
Log-logistic	llg
Normal	nor

Table 2.7. Probability distribution functions tested for best fit with the empirical probability of failure obtained from the application of Monte Carlo method.

2.3.4 Probability of failure

The Logistic distribution eventually selected to represent the probability distribution of the Factor of Safety is characterised by two parameters, m_{lgs} and s_{lgs} respectively, which are linked to the mean and variance of Factor of Safety obtained from the FOSM method via Eq. 2.15 and Eq. 2.16; their values are shown in Table 2.8:

$$m_{lgs} = \mu[FS_{min}]$$ ***Eq. 2.15***

$$s_{lgs} = \frac{\sqrt{3\sigma^2[FS_{min}]}}{\pi}$$ ***Eq. 2.16***

m_{lgs}	**1.418**
s_{lgs}	**0.111**

Table 2.8. Parameters of Logistic distribution.

The probability of failure can therefore be calculated as the value of the Logistic Cumulative Distribution Function corresponding to *FS_{min}* equal to one, as shown in Eq. 2.17.

$$p_f = \frac{1}{1 + e^{-\frac{1-m_{lgs}}{s_{lgs}}}}$$ ***Eq. 2.17***

The value of the probability of failure was found to be equal to 2.3%. This value is associated with the flood events, i.e. a failure is expected to occur in 2.3% of flood events. In order to calculate an annual probability of failure the average frequency of flood events λ_f has to be taken into account as shown in Eq. 2.18:

$$p_a = p_f \lambda_f$$ ***Eq. 2.18***

The annual probability of failure p_a is equal to 1.8%; this result is consistent with the 'observed' probability of failure of 1% given the failure observed in 1981.

2.4 Conclusions

The paper has presented an accessible approach that allows accounting for uncertainty in multiple variables in the stability analysis of flood embankments, including the soil hydro-mechanical properties and the hydrological loading. To take into account transient water flow, an approach has been presented to characterise the entire hydrograph in probabilistic terms.

The proposed approach is based on the FOSM method, which allows for the estimation of the mean and variance of the Factor of Safety. The approach addresses the main limitation of the FOSM method applied to the calculation of the probability of failure, which lies in the a priori assumption of the probability distribution function of the Factor of Safety. The criterion put forward in this study consists in selecting the probability distribution that best matches the empirical probability of failure derived from the Monte Carlo method with a single input variable.

The approach has been tested and validated against the failure case-study of an embankment along the Adige River in the North of Italy. The annual probability of failure calculated with the proposed method was found to be in good agreement with the observed annual probability of failure.

The proposed method has the practical advantage to provide the geotechnical engineer with a tool to quantify the influence of the uncertainty of each random variable on the variability of the Factor of Safety. This information can be extremely useful when planning on monitoring and investigation campaigns in order to wisely focus investments of resources and time towards a decrease of uncertainty for the most relevant variables.

The proposed method has also the advantage to be accessible to geotechnical engineers with limited background in probability and statistics. The application of the method requires performing a limited number of deterministic-style simulations manageable with any available commercial software. This makes the method an affordable tool to assess the safety of flood embankments in probabilistic terms for routine applications in geotechnical engineering.

2.5 Acknowledgements

The authors wish to acknowledge the support of the European Commission via the Marie Curie IRSES project GREAT ‘Geotechnical and geological Responses to climate change: Exchanging Approaches and Technologies on a world-wide scale’ (FP7-PEOPLE-2013-IRSES-612665). The authors also wish to acknowledge the support of the Autonomous Province of Bolzano (Italy).

3. FAILURE HAZARD OF FLOOD EMBANKMENTS DUE TO UPLIFT PRESSURE: LESSON LEARNED FROM THE ADIGE RIVER CASE STUDY

Abstract

The paper presents the case study of the Adige river embankment, a segment of which experienced instability of the landside slope due to the development of uplift pressures. Soil profile and hydro-mechanical properties of the embankment and foundation materials have been assessed via site investigation, laboratory testing, and field monitoring for two cross sections, within and outside the failure segment respectively. The hydro-mechanical model developed thereof was first validated against its ability to reproduce the observed annual probability of failure for the two sections with a FOSM-based approach. Comparison of water flow regimes between the two sections was then used to highlight the importance of the hydraulic properties of the material on the landside for the development of uplift pressures at the toe of the embankment. The lesson learnt from this case study is that the hydraulic response of the ground on the landside may play a critical role on the stability of flood embankments and its characterisation should therefore not be overlooked when planning site investigation.

3.1 Introduction

Flood embankments are essential structures in flood defence systems and their failure can lead to devastating consequences. One of the most critical failure mechanisms is represented by the instability of the landside slope triggered by the development of high uplift pressures at the toe of the embankment (Phoon, 2008), often accompanied by the formation of sand boils (CIRIA, 2013). This is frequently the case when embankments are built on top of foundation layers having significantly higher hydraulic conductivity. Although this kind of stratigraphy is not uncommon, there are a few case studies reported in the literature documenting the development of uplift pressure as the primary cause of failure (Marsland & Randolph, 1978).

This paper presents a case study associated with a segment of the Adige River embankment subject to instability during a flood in 1981. This was the first failure ever since construction, which took place between 1860 and 1890 (Werth, 2003). Having observed one failure in about 100 years, the annual probability of failure of this segment is of the order of 1%.

This segment experienced instability with a failure mechanism on the landside (Pozzato, et al., 2014), likely associated with uplift pressures as boiling is often observed during intense flood events. Instability was characterised by the formation of a scarp, but the embankment did not experience a full collapse. As a result, the materials and soil profile to date are exactly the same as at the time of failure. This offers the unique chance to characterise the soil profile and hydro-mechanical properties of the embankment and its foundation as they were at the time of failure.

This is rarely the case as instability is often accompanied by a breach with the embankment and the foundation layers swept away, making soil profile and material characterisation impossible to reconstruct a posteriori.

Two sections were analysed for comparison, one within and one outside the failure segment. Soil profile was characterised via boreholes, DPH, and EM scanning. Laboratory testing was carried out to characterise grain size distribution and to investigate shear strength, saturated hydraulic conductivity, and water retention behaviour of the embankment material. Cell piezometers and tensiometers were installed in the zone below and above phreatic surface respectively and their measurements were used to characterise the hydraulic properties of embankment and the shallow foundation layer by inverse analysis of hydraulic flow.

The stability assessment was conducted in probabilistic terms to account for the uncertainty due to the natural variability of soil and the random frequency and magnitude of flood events. In particular, the hydrograph was characterised in probabilistic terms in order to ‘annualise’ the probability of failure by considering the average frequency of flood events. This allowed validating the model against the observed values of the annual probability of failure. The probabilistic assessment in terms of annual probability of failure allows benchmarking the hydro-mechanical model against a quantified probability of failure, which could not be achieved by considering a deterministic hydrograph.

The probabilistic hydro-mechanical model was first validated against its capability to reproduce realistic annual probability of failure within the failure segment (~1%) and outside the failure segment (<<1%). The hydro-mechanical model was then used to highlight critical aspects of the mechanism of failure and the key role played by the soil profile on the landside.

3.2 The case study

The embankments on the Adige River (Northern Italy in Figure 3.1) were built at the end of 19th century to straighten the river path. The traces of the ancient meanders are still visible along the alluvial valley and are easily recognisable from aerial photographs and satellite images (Angelucci, 2013). These resources can be coupled with historical cartography to reconstruct the ancient meandering path of the river (Figure 3.2).

During an intense flood event in July 1981, a 230 m segment of the embankment near the village of San Floriano experienced instability and a 50 cm deep scarp was observed on the crest of the embankment (Figure 3.3). The probability of failure has been assessed for this segment as well as for a section in the South outside the failure segment ('stable' in Figure 3.2).

Figure 3.1. Adige River in the North of Italy.

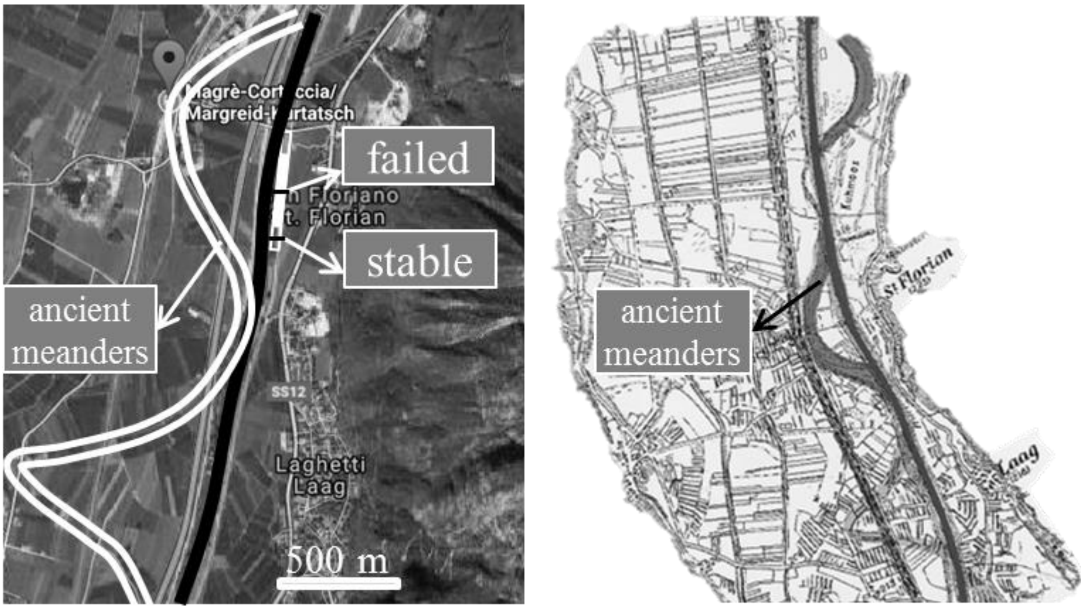

Figure 3.2. Ancient meanders of the riverbed before the construction of flood embankments (Werth, 2003).

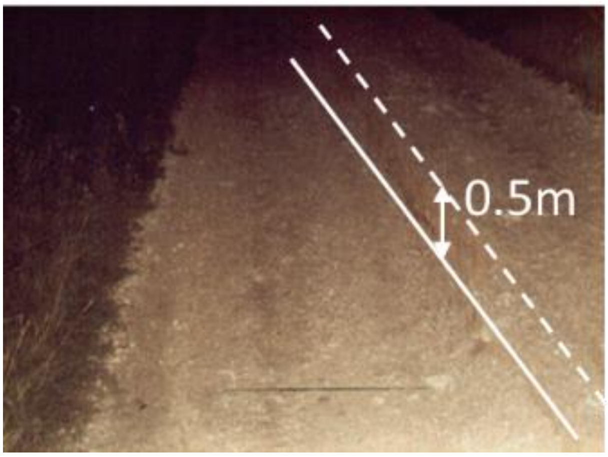

Figure 3.3. Scarp observed on the crest of the embankment in San Floriano during the flood event in 1981, modified from Zwanenburg, et al..

3.3 Soil profile

Soil profile has been inferred from boreholes and Dynamic Probing Heavy (DPH) tests from the crest at different locations along a 500 m segment (Figure 3.4), which includes the failure segment and the stable zone South of the failure segment. Layer boundaries inferred from visual inspection of core samples and DPH blow number are shown as diamonds and circles respectively in Figure 3.5. The soil profile was then cross-checked via the grain-size distribution (GSD) of samples taken from the identified soil horizons (black rectangles in Figure 3.5).

The body of the embankment is made of two different layers. The upper layer is a gravelly shell, whereas the core of the embankment is a brown sandy silt. The thickness of the embankment core layer is fairly constant (~6 m) along the 500 m segment. The thickness of the gravelly shell is slightly larger in the area located North of the failure zone, closer to San Floriano Bridge, but it is fairly constant (~1.1 m) in the area of the failure segment and outside the failure segment in the South.

Two layers form the embankment foundation. The first layer is a brown-grey sandy material, with significant coarse fraction and rounded particles. This material has alluvial origin and corresponds to the ancient riverbed where the Adige River flowed before being straightened. This material is also encountered outside the ancient riverbed projection as derived from aerial photographs and historical maps (Figure 3.2). This is because the alluvial deposit extends beyond the ancient riverbed, especially on the concave side of the meander. The deep foundation layer is a dark grey sandy deposit, with local lenses of finer material. It constitutes the glacial lacustrine deposit where the Adige River formed its meandering path.

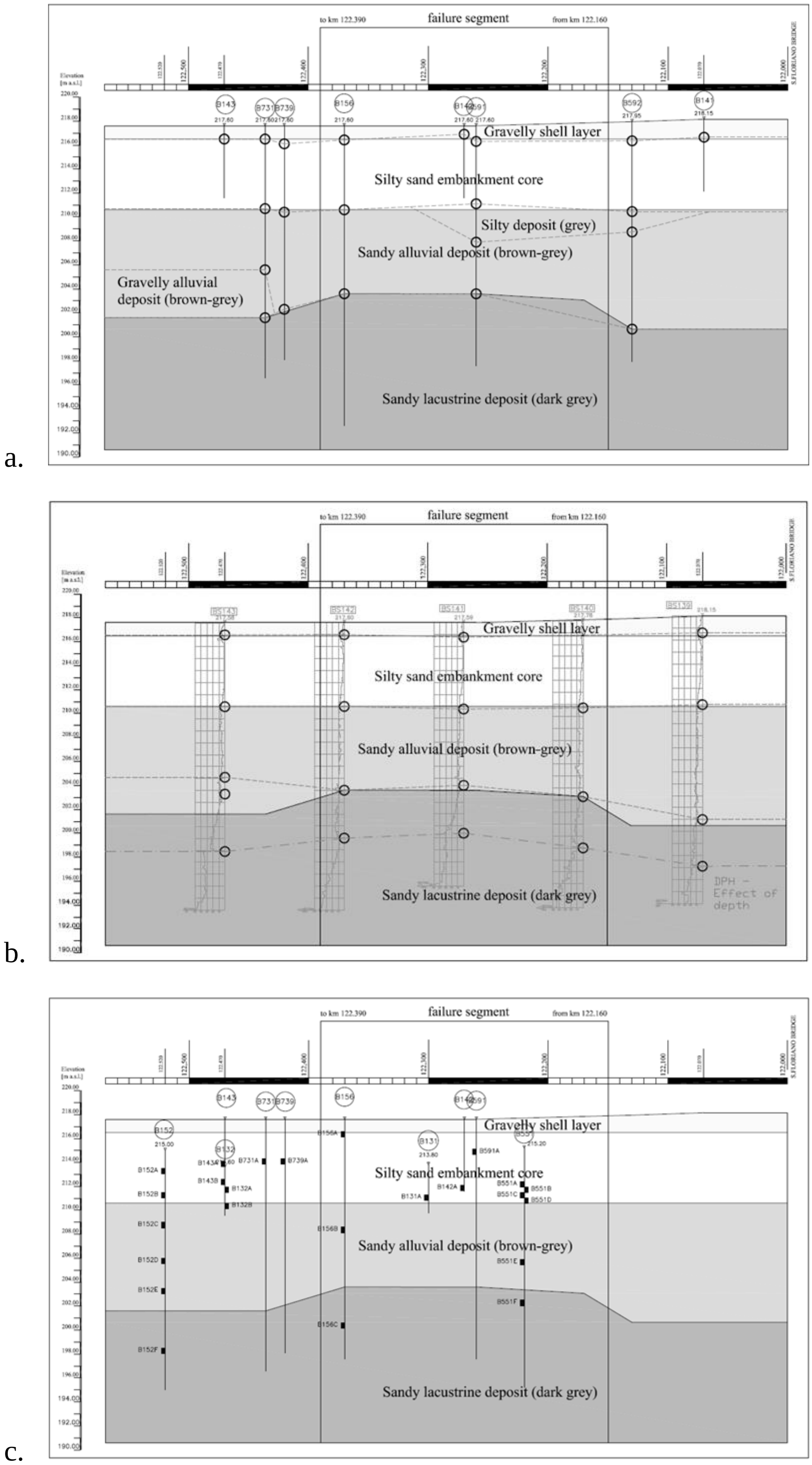

Figure 3.4. Longitudinal soil profile with details of (a) boreholes, (b) DPH tests and (c) samples collected for grain size analysis.

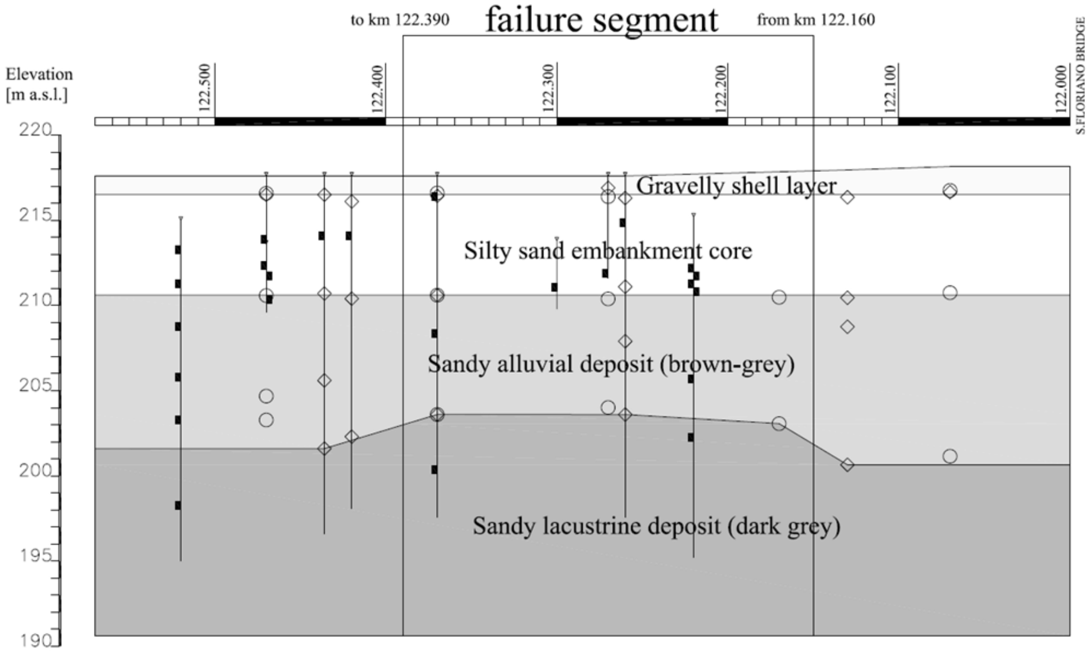

Figure 3.5. Longitudinal soil profile: layer boundaries identified from visual inspection of the borehole logs (diamonds) and DPH tests (circles) and samples collected for grain size analysis (black rectangles).

The two cross sections examined in this study are located at chainage km 122.25 (within the failure segment) and at chainage km 122.42 (outside the failure segment). After the failures observed in 1981 the entire segment of embankment has been reinforced by a berm on the landside slope (Figure 3.6) which has not been included in the geotechnical model in this study.

Only two boreholes, B131 and B132 for the sections within and outside the failure segment respectively (Figure 3.6), have been drilled on the landside at the toe of the embankment down to 4m. Additional information was therefore required to characterise the soil profile on the landside. Investigation was carried out using EM profiling based on Slingram method (Nabighian, 1992) using the device GEM2 (GEOPHEX USA) along the toe of the embankment. Results are shown in Figure

3.7. The sharp local anomalies of resistivity (chainage km 122.19, 122.28, 122.35) are associated with the presence of artificial metal objects on the surface. Within the failure segment, apparent resistivity is essentially constant with a slightly increasing trend from chainage km 122.24 to km 122.39. Outside the failure segment the resistivity increases, more markedly from chainage km 122.41. This is associated with the appearance of the sandy alluvial deposit generated by the ancient river, which is close to the embankment in the South section. The alluvial deposit on the landside therefore appears in the South but not in the failure segment, as reflected in the soil profile for the two cross-sections (in Figure 3.8).

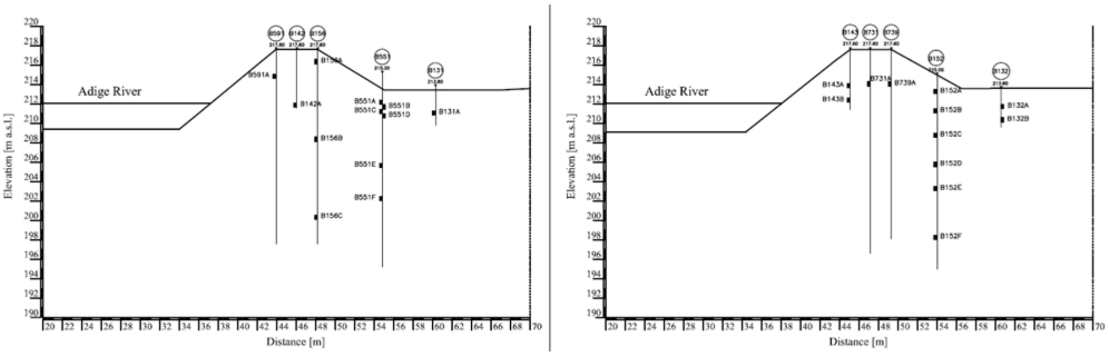

Figure 3.6. Topography and samples collected for grain size distribution from within (left) and outside (right) the failure segment.

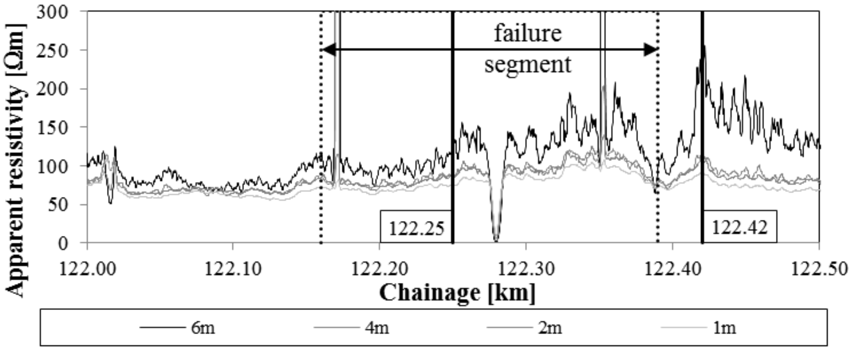

Figure 3.7. EM measurements along the longitudinal profile taken on the landside at the toe of the embankment.

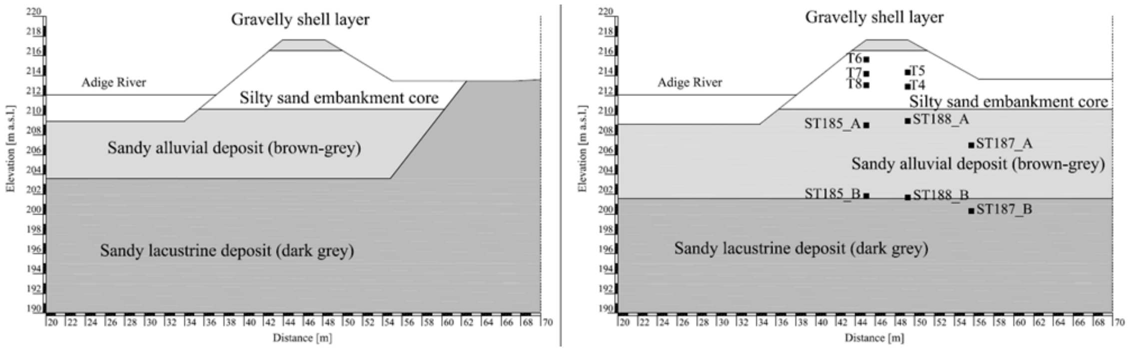

Figure 3.8. Soil profile for the section within (left) and outside (right) the failure segment.

Grain size distributions for the identified materials are shown in Figure 3.9. The embankment core is fairly homogeneous within and outside the failure segment. The alluvial material and the lacustrine material show larger variability along the longitudinal profile (Figure 3.9b,c). The grain size distribution of the sample collected at a depth of 3.5m from the only borehole on the landside in the section outside the failure segment (B132B) is consistent with the grain size distribution of the alluvial material. This confirms that the alluvial deposit extends beyond the toe of the embankment in the section located South of the failure segment.

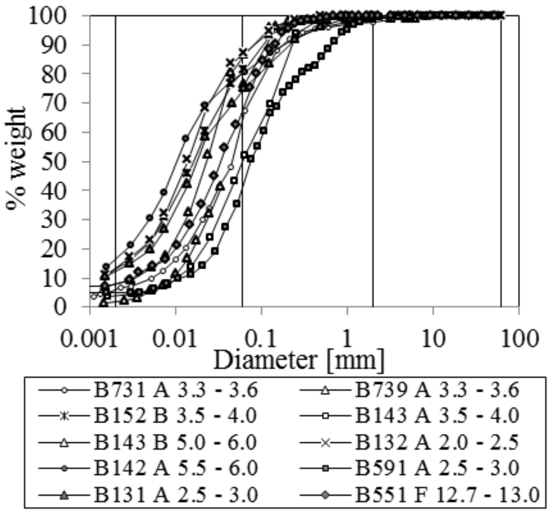

a.

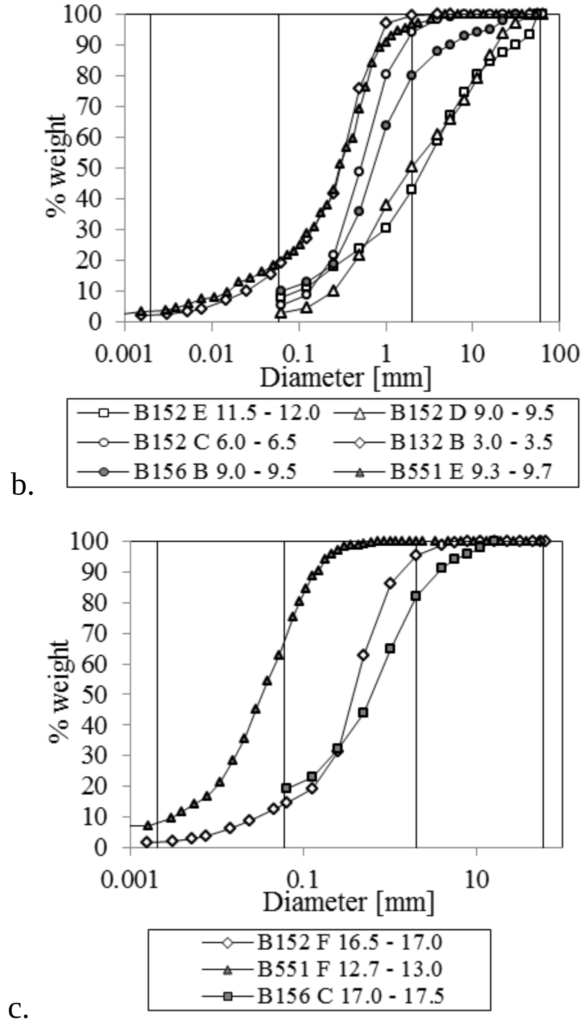

Figure 3.9. Grain size distributions for (a) embankment core, (b) alluvial deposit, (c) lacustrine deposit (grey = samples within failure segment; white = samples outside failure segment).

3.4 Hydro-mechanical characterisation

3.4.1 Deterministic hydraulic characterisation

3.4.1.1 Water retention behaviour of embankment material

Water retention behaviour of the embankment material was determined from loose samples reconstituted in the laboratory by compaction at target dry density of 1.53 g/cm^3 consistent with the estimated field value. The density index of the embankment material was first estimated based on SPT and DPH tests (I_D=0.26-0.36). Assuming a minimum and a maximum void ratio e_{min}=0.30 and e_{max}=0.90 (Lambe & Whitman, 1969), the dry density was estimated in the range 1.50-1.55 g/cm^3. Specimens 100 mm diameter and 100 mm high were compacted to gravimetric water contents ranging from 9% to 21%. After moisture equilibration overnight, matric suction was measured using a High-Capacity Tensiometer (Tarantino & Mongiovì, 2003). Water retention data points of compacted samples can be associated with the main wetting curve (Tarantino & Tombolato, 2005), which is reasonably representing water retention behaviour for infiltration associated with the flood.

The experimental data points (Figure 3.10) have been fitted with Van Genuchten model for water retention (Van Genuchten, 1980). The effective saturation S_e is defined by Eq. 3.1:

$$S_e = \frac{\theta - \theta_{res}}{\theta_{sat} - \theta_{res}} = \frac{1}{(1 + (\alpha s)^n)^m} \qquad \textbf{\textit{Eq. 3.1}}$$

where s is the suction, θ, θ_{sat} and θ_{res} are the current, saturated, and residual volumetric water contents respectively, and α and n are soil parameters (α=0.07 and n=1.438). The relative hydraulic conductivity was derived from S_e as per Eq. 3.2 (Van Genuchten, 1980).

$$k_{rel} = S_e^{-0.5}\left(1-\left(1-S_e^{\frac{1}{m}}\right)^m\right)^2 \qquad \textbf{\textit{Eq. 3.2}}$$

3.4.1.2 Saturated hydraulic conductivity of foundation layers via laboratory testing

Two specimens 80 mm diameter and 20 mm high were cut from samples taken from the alluvial deposit and lacustrine deposit at the depths of 7.3-7.7 and 12.7-13.00 m respectively (Borehole B551). The specimens were consolidated in an oedometer to 160 kPa and 250 kPa for the 7.3-7.7 and 12.7-13.00 samples respectively to reproduce field effective stress (Aldegheri, 2009).

Constant head hydraulic conductivity tests were carried out by connecting the base of the oedometer to a water reservoir placed on a balance to measure water flow rate. The values obtained for the saturated hydraulic conductivity were $8{\cdot}10^{-6}$ m/s and $4{\cdot}10^{-8}$ m/s for alluvial and lacustrine deposit respectively. The values were not considered representative of the field hydraulic conductivity in the sense that differences of 1-2 order of magnitude are generally observed between laboratory and field values. Nonetheless, the ratio between these two laboratory values was assumed to be representative of the same ratio of field values.

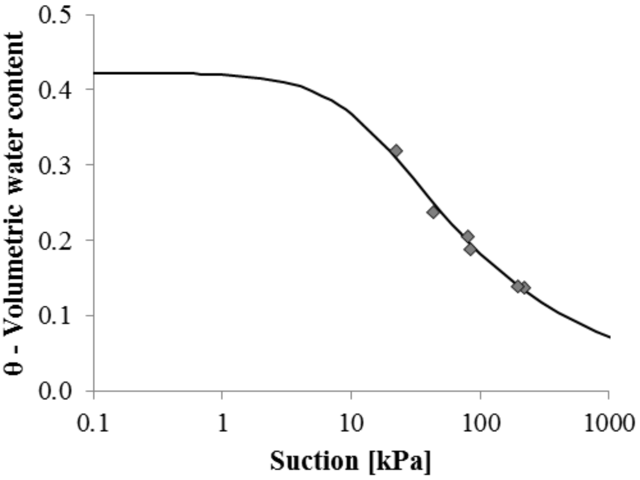

Figure 3.10. Experimental data points and Van Genuchten model for the water retention curve of the embankment material.

3.4.1.3 Saturated hydraulic conductivity of embankment and upper foundation via inverse analysis of piezometer and tensiometer data

A monitoring system has been installed at the section outside the failure segment consisting of i) 6 pressure transducers (B1-MOD level transducer from Tecnopenta) installed via bayonet fitting at the bottom of standpipe piezometers to measure pore-water pressure below the phreatic surface mainly in the alluvial deposit and ii) 5 tensiometers (T8 tensiometer from UMS) to measure suction above the phreatic surface (Figure 3.8).

The calibration of the TecnoPenta pressure transducers was verified in the field by moving the pressure transducer at different locations in the standpipe piezometers (filled with water once the piezometer was removed from its bayonet fitting). The calibration curve of the UMS tensiometers was verified in the field by submerging the porous tip into a water-filled container and imposing vacuum via a hand-operated pump.

Measurements recorded by the instruments were used to characterise the saturated hydraulic conductivity of the embankment and the alluvial deposit by inverse analysis. The time selected for the inverse analysis was a two-week window in summer 2016, where the Adige River recorded its highest level since the installation of the instruments (Figure 3.11).

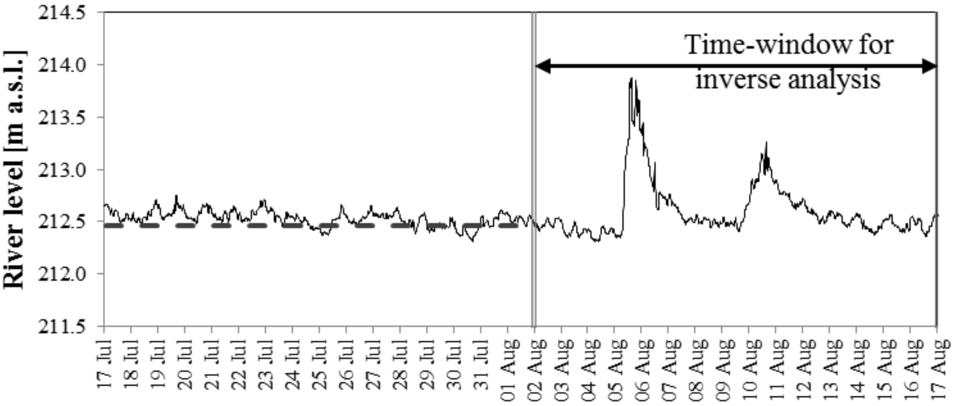

Figure 3.11. River level variations recorded between 17th July and 17th August 2016.

Measurements by the shallow tensiometer T6, closer to the ground surface, were clearly affected by the rainfall, whereas measurements by the intermediate and deep tensiometers were not (Figure 3.12b). Atmospheric boundary conditions on the crest of the embankment did not have a significant effect on the seepage in the embankment core below shallow depths. At the same time, intermediate and deeper tensiometers clearly responded to the fluctuation of the river level, which was considered as the hydraulic boundary condition in the inverse analysis.

The saturated hydraulic conductivities of the embankment and the alluvial deposit were selected to allow for the best matching between simulated and observed data. In lack of data, the ratio between the hydraulic conductivities in vertical and horizontal direction has been assumed equal to $k_V/k_H = 0.1$ for the foundation layers.

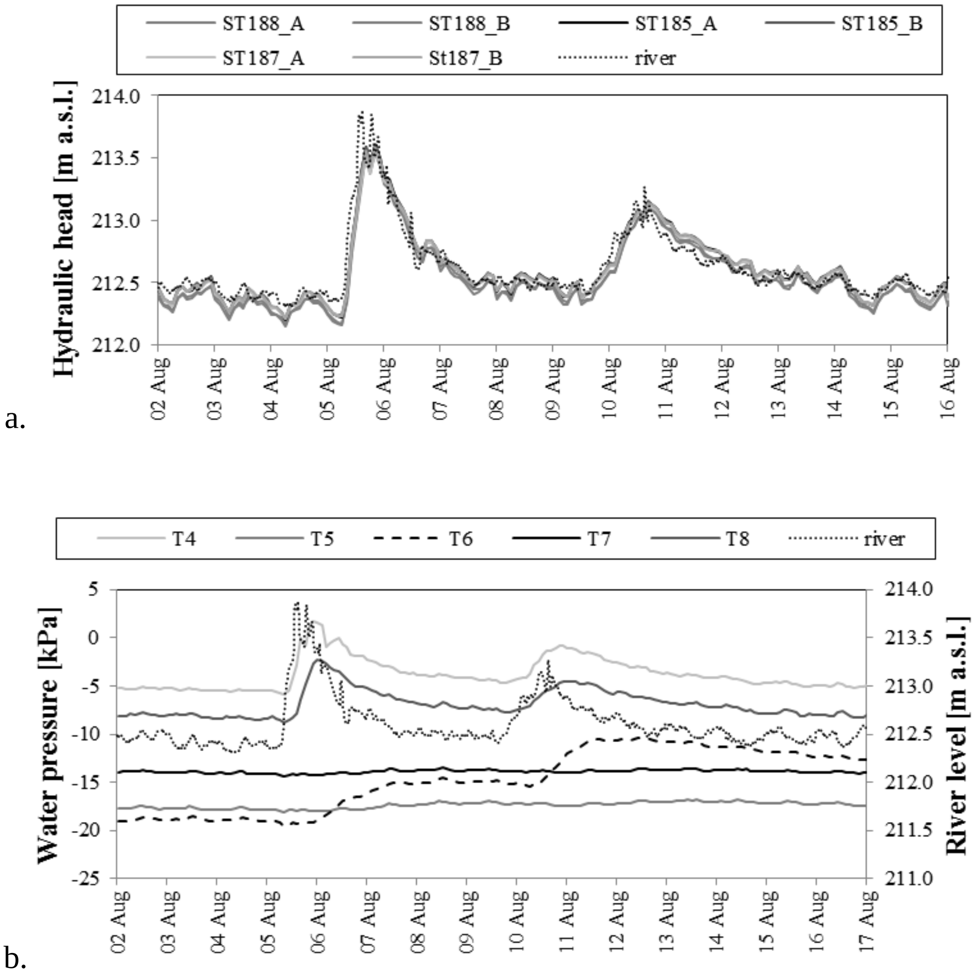

Figure 3.12. Measurements recorded by (a) piezometers and (b) tensiometers in August 2016.

The comparison between simulated and measured pore-water pressure values is reported in Figure 3.13 and was considered satisfactory. The maximum difference between measured and simulated values was less than 4 kPa for the piezometers and less than 3 kPa for the tensiometers. The values of saturated hydraulic conductivity derived from the inverse analysis are $2 \cdot 10^{-6}$ m/s and $4 \cdot 10^{-3}$ m/s for the embankment material and alluvial deposit respectively. It is worth observing that the saturated hydraulic conductivity for the alluvial deposit material derived from the inverse analysis is greater than the one measured in the laboratory tests by about two orders of magnitude, which is a difference typically encountered when comparing laboratory and field measurements of hydraulic conductivity.

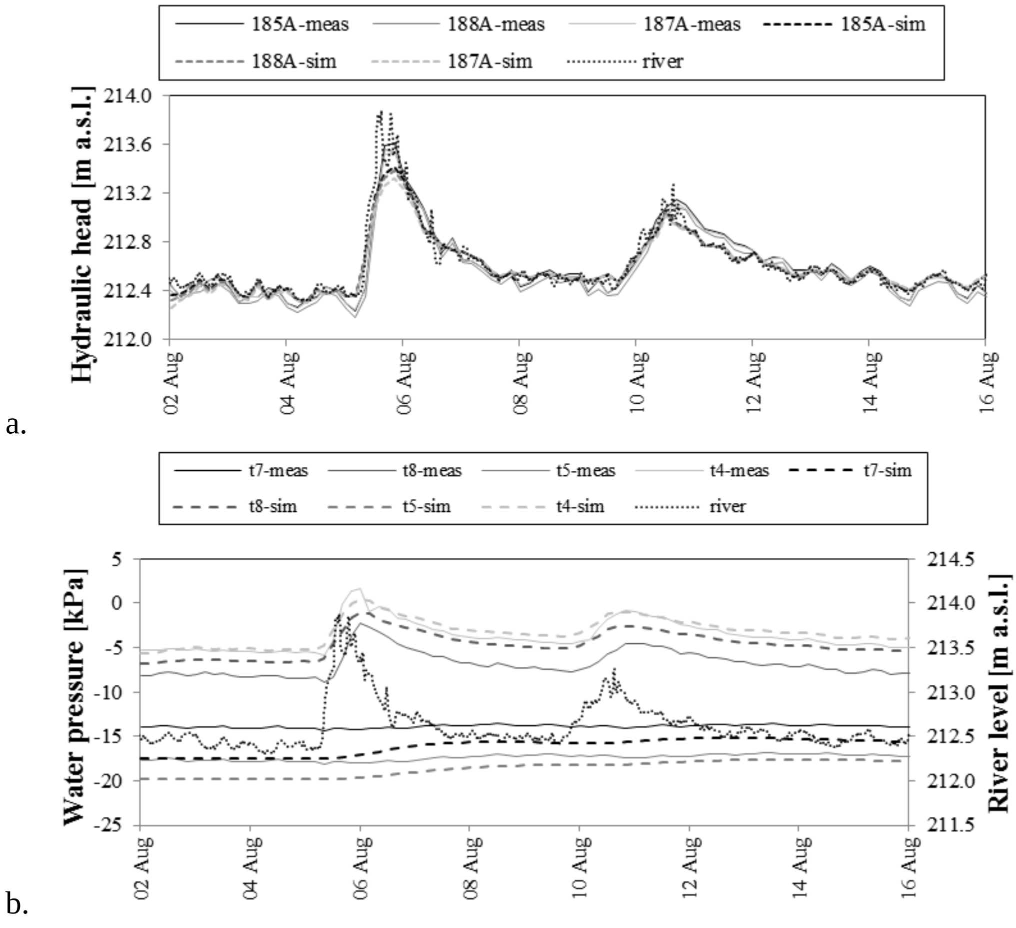

Figure 3.13. Comparison between measured (continuous lines) and simulated (dashed lines) values of (a) hydraulic head in piezometers and (b) pore water pressure in tensiometers.

3.4.2 Deterministic shear strength characterisation

Shear strength behaviour of the embankment material was determined on two sets of specimens. Two specimens from within the failure segment (B551, depth 4.20 - 4.80 m) were reconstituted from slurry and sheared at a vertical stress of 75 kPa and 150 kPa respectively under saturated conditions at shear displacement rate of 2mm/h (Aldegheri, 2009). Both specimens showed a monotonic increase in shear strength until the ultimate state with compressive behaviour.

Two specimens from outside the failure segment (B739, depth 3.0-3.3 m) were compacted into the shearbox to vertical stress of 200 kPa and water content of 18% and 21% respectively to achieve a target dry density similar to the specimens prepared for the water retention behaviour. Specimens were then unloaded to 120 kPa and 60 kPa vertical stress respectively to simulate field stress conditions. Afterwards, the specimens were saturated by flooding the shearbox external container and sheared at displacement rate of 1.6 mm/h. All specimens showed a monotonic increase in shear strength until the ultimate state with compressive behaviour. The specimens from within and outside the failure segment aligned to the same failure envelope in the Mohr-Coulomb plane (Figure 3.14) characterised by a friction angle equal to 28.9°.

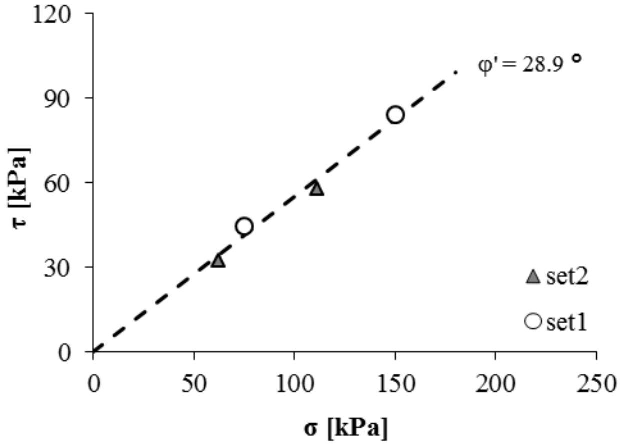

Figure 3.14. Failure envelope obtained from direct shear tests on two sets of specimens from the embankment core.

3.4.3 Probabilistic modelling of hydro-mechanical properties

Material properties have to be characterised in probabilistic terms in order to calculate the probability of failure of the embankment. The experimental characterisation in this study did not provide sufficient data to develop a full probabilistic model for the hydro-mechanical properties of the embankment. The values obtained from the experimental hydro-mechanical characterisation were therefore assumed as mean values, while the standard deviation was estimated on the basis of published values of coefficients of variations COV (ratio of the standard deviation to the mean value) as suggested by Duncan (2000).

- *Friction angle*: COV equal to 6%, in the range 2-13% suggested by Duncan (2000).

- *Saturated hydraulic conductivity*: COV equal to 90%, consistent with literature values ranging from 10% (Nguyen & Chowdhury, 1985) to 160% (Zhang, et al., 2005).
- *Water retention curve:* COV of 60% and 9% were assumed for the α and n parameters in Van Genuchten model respectively after Likos, et al. (2014). The parameters α and n were assumed to be independent, consistently with their physical meaning, being α related to the largest pore size in the material and n to the pore size distribution.

The saturated hydraulic conductivity of the foundation was not considered in probabilistic terms because preliminary studies on the embankment in San Floriano (*Chapter 2*) showed that its variability has little influence on the variability of the Factor of Safety. The mechanical properties of the foundation layers do not play any role in the stability analysis because slip surfaces are not deep enough to reach the foundation layers; a deterministic friction angle equal to 33^0 has been assumed for both materials.

A LogNormal distribution was assumed for all variables. Normal or LogNormal distributions are usually selected for the probability distribution of soil hydro-mechanical properties (see for example Arnold & Hicks, 2011; Suchomel & Mašín, 2010; Malkawi, 2000). The LogNormal distribution has the advantage of never taking any negative values (Uzielli, et al., 2007), which is consistent with most soil properties.

3.5 Hydrological loading

3.5.1 Deterministic modelling of hydrological loading

Adige River level variations are constantly recorded by a hydrometer located in Bronzolo, about 15 km north of the segment of interest. Thirty flood events have been recorded between 1977 and 2014. The recorded hydrographs have been collected to isolate the key variables and define a typical shape of the hydrograph for the area. The key parameters describing the hydrograph have been identified in the initial river level h_{start}, the maximum river level h_{peak}, the time required for the river level to reach the peak t_{peak} and a shape parameter β governing the falling limb of the hydrograph (Amabile, et al., 2016). Values of h_{peak}, h_{start}, t_{peak} and β have been obtained for the 30 recorded flood events by fitting the recorded hydrographs with the model described in Eq. 3.3 and Eq. 3.4 for the rising limb and falling limb respectively:

$$h = h_{start} + \frac{h_{peak} - h_{start}}{t_{peak}} t \quad (t \leq t_{peak})$$ ***Eq. 3.3***

$$h = h_{peak} * \left(\frac{t}{t_{peak}}\right)^{(-\beta)} \qquad (t > t_{peak})$$ ***Eq. 3.4***

3.5.2 Probabilistic modelling of hydrological loading

The probabilistic model for the hydrological loading has been developed by verifying the correlations between the identified key variables and identifying their probability distribution. In order to find the joint distribution of the variables all the pairs of variables were tested for independence. Correlation has been tested with Pearson’s correlation coefficient at a 5% significance level. The obtained *p*-values are reported in Table 3.1. Only the pairs h_{peak}-β, h_{start}-β and t_{peak}-β show correlations under the 5% significance level. The shape parameter β is therefore not independent and was obtained by multiple linear regression as shown in Eq. 3.5.

$$\beta = 0.0009407h_{peak} - 0.001062h_{start} + 0.1005t_{peak}$$

Eq. 3.5

where the coefficients have been estimated by the Ordinary Least Squares method. The difference between the observed values of β and the values predicted by the multiple linear regression model is shown in Figure 3.15. The empirical cumulative distributions for the independent variables h_{peak}, h_{start} and t_{peak} have been derived from the analysis of the database of past flood events. The optimal probability distribution for each variable has been obtained by Maximum Likelihood Estimation (Table 3.2). The LogNormal distribution appears satisfactory for all variables with means and standard deviations reported in Table 3.3.

Variables	**h_{peak} [cm]**	**h_{start} [cm]**	**t_{peak} [d]**	**β**
h_{peak} [cm]	1	0.778	0.669	0.0011
h_{start} [cm]	0.778	1	0.137	0.0002
t_{peak} [d]	0.669	0.137	1	0.0007
β	0.0011	0.0002	0.0007	1

Table 3.1. Matrix of p-values obtained for Pearson's correlation test.

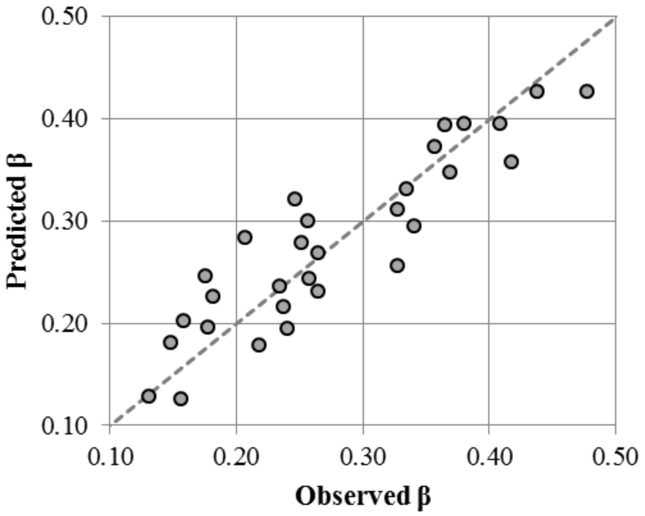

Figure 3.15. Difference between observed values and predicted values of β.

Distribution	h_{peak}	h_{start}	t_{peak}
Normal	-158	-157	-12
LogNormal	**-157**	**-157**	**-9**
Exponential	-221	-206	-32
Gamma	-157	-157	-10
T distribution	-158	-157	-11
Cauchy	-163	-163	-14
Weibull	-160	-157	-12

Table 3.2. Log-likelihood values obtained by fitting different probability distributions to the observed data for the hydrograph variables.

Variable	μ	σ
h_{peak} [cm]	580	45.4
h_{start} [cm]	354	46.0
t_{peak} [d]	1.083	0.334

Table 3.3. Probability distribution of key variables for the hydrological loading.

3.6 Deterministic assessment of embankment stability

3.6.1 Seepage analysis

The finite element software SEEP/W (GEO-SLOPE, 2004) was used to analyse transient saturated/unsaturated seepage in the embankment and its foundation.

The boundary condition on the riverside was represented by the time-dependent hydraulic head (i.e. the hydrograph), whereas the vertical boundary on the landside and the bottom boundary were modelled as impermeable boundaries. The distance of the landside vertical boundary from the toe of the embankment was set equal to 80m, large enough so that the pore-water pressure distribution up to 10 m from the toe of the embankment is not affected by the boundary condition on the landside. The vertical boundary on the riverside was modelled as an impermeable boundary being an axis of symmetry. The crest of the embankment, the landside slope and the ground surface were potential seepage faces. The soil-atmosphere interaction was not considered and therefore not included in the seepage model in the form of inward or outward flux (i.e. rainfall or evaporation).

The initial condition was obtained from a steady-state seepage analysis associated with the initial river level for the flood event h_{start}. In the steady state analysis the far field boundary condition on the vertical boundary on the landside is represented by a constant head equal to 211.45m. This corresponds to the average measurement of water level in a well located 80m from the toe of the embankment observed in winter when the baseline river level was lower than the level in the well. The level in the well was therefore attributed to the far-field groundwater table.

An unstructured mesh of quadrilateral and triangular elements was adopted for the entire domain (Figure 3.16). The mesh density in the regions where higher gradients develop was optimised by reducing the element size until no significant change in pore-water pressure was observed (~0.5 kPa). For the embankment core, the alluvial deposit and the gravelly shell, elements with size equal to 0.4m were adopted, while 1m elements have been used for the lacustrine foundation layer. A constant time step of one hour has been used for the entire duration of the seepage simulation (four days). The optimal time step duration has been selected with the same approach adopted for the mesh density, by reducing an initial time step of 3 hours until no significant change in pore water pressure was observed (~0.5 kPa).

3.6.2 Stability analysis

The stability analysis was carried out using Bishop's simplified method (Bishop, 1955). The iterative procedure to calculate the Factor of Safety was completed with the software SLOPE/W (GEO-SLOPE, 2004). The pore-water pressures from the transient seepage analysis were used to calculate the evolution of the Factor of Safety over the duration of the flood event. The unsaturated shear strength model (Vanapalli, et al., 1996) implemented by the software was considered appropriate for the embankment coarse-grained material (Tarantino & El Mountassir, 2013). The critical slip surface was assumed circular and then refined with the optimisation algorithm based on the segmental technique. The stability analysis only focused on the landside slope, where the scarp was observed at the time of failure. Instability of the riverside slope is a common failure mechanism for embankments with a very low permeability in case of rapid draw down of the river level, but is not usually observed in cases where the relatively high hydraulic conductivity of the material allows a quick dissipation of excess pore water pressures.

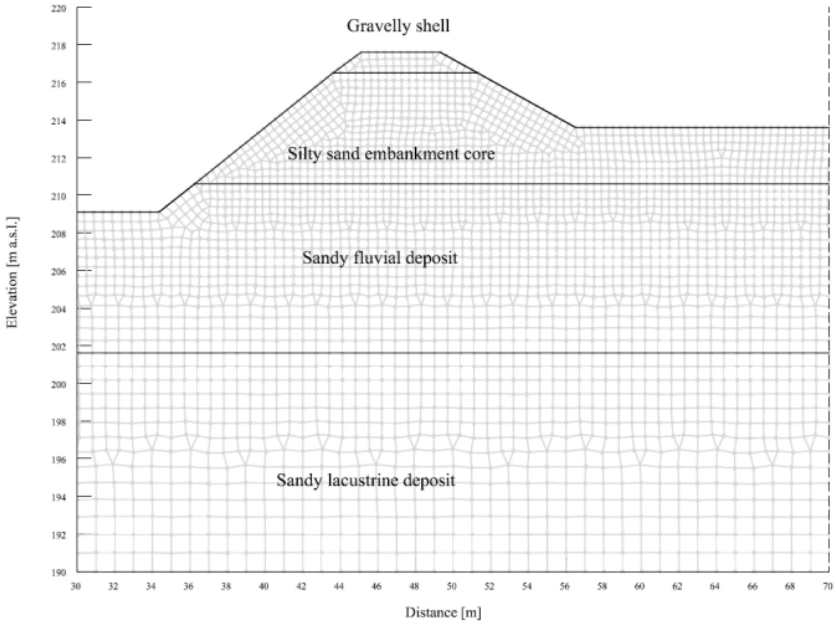

Figure 3.16. Sample of mesh density in the different layers for the seepage analysis.

3.7 Probabilistic assessment of embankment stability

The probability of failure of the embankment has been calculated with a probabilistic approach based on the First Order Second Moment (FOSM) method (Wolff, et al., 2004). The Factor of Safety is derived as a Taylor's series expansion with the first order terms of the series used to calculate the mean and variance as a function of the input variables $X_1, \ldots, X_n$. For uncorrelated input variables the mean $\mu[FS]$ and the variance $\sigma^2[FS]$ are given by Eq. 3.6 and Eq. 3.7 respectively:

$$\mu[FS] \cong FS(\mu[X_1], \mu[X_2], \ldots, \mu[X_n])$$ ***Eq. 3.6***

$$\sigma^2[FS] \cong \sum_{1}^{n} \left(\frac{\partial FS}{\partial X_i}\right)^2 \sigma^2[X_i] \qquad \textbf{\textit{Eq. 3.7}}$$

The partial derivatives in Eq. 3.7 were estimated numerically with a finite difference method by choosing the increment of each input variable equal to its standard deviation. The probability of failure corresponds to the probability of having a Factor of Safety lower than or equal to unity. The application of the FOSM method on its own only provides information about the mean and variance of the Factor of Safety. A probability distribution function of the Factor of Safety must be assumed a priori in order to calculate the probability of failure, very often Normal (Baecher & Christian, 2005) or LogNormal (Duncan, 2000). In order to overcome this limitation, the appropriate probability distribution function for the Factor of Safety has been selected as proposed in *Chapter 2*. The selection of the probability distribution function is based on the application of the Monte Carlo method for a single input variable. Different probability distribution functions were fitted to the Monte Carlo-derived empirical distribution function and the Logistic distribution function, which returned the best match of the value of the empirical probability of failure, was selected.

3.8 Application and results

The number of simulations required for the application of the FOSM method is $2n+1$, where n is the number of independent input variables X_i. Seven independent input variables were considered in this study: three variables are related to the hydrological boundary condition (h_{peak}, h_{start}, t_{peak}) while four variables correspond to material properties (k_{sat}, φ', α, n). In each simulation the minimum value of the Factor of Safety over time FS_m has been obtained (Table 3.4).

simulation		**FS_m**	
		Within f.s.	**Outside f.s.**
1	all variables taken with mean value	1.418	1.779
2	$h_{peak} = \mu + \sigma$	1.311	1.656
3	$h_{peak} = \mu - \sigma$	1.532	1.878
4	$h_{start} = \mu + \sigma$	1.324	1.648
5	$h_{start} = \mu - \sigma$	1.479	1.895
6	$t_{peak} = \mu + \sigma$	1.401	1.729
7	$t_{peak} = \mu - \sigma$	1.462	1.835
8	$\varphi' = \mu + \sigma$	1.519	1.904
9	$\varphi' = \mu - \sigma$	1.344	1.685
10	$k_{sat} = \mu + \sigma$	1.388	1.71
11	$k_{sat} = \mu - \sigma$	1.603	1.919
12	$n = \mu + \sigma$	1.420	1.791
13	$n = \mu - \sigma$	1.420	1.788
14	$\alpha = \mu + \sigma$	1.460	1.818
15	$\alpha = \mu - \sigma$	1.396	1.671

Table 3.4. Minimum Factor of Safety FS_m from slope stability analyses.

For both cross sections, the minimum Factor of Safety FS_m is fairly linear with respect to the input variables, thus complying with the implicit assumption of the FOSM method that considers only first order terms of the Taylor's series expansion. The mean value of the minimum Factor of Safety $\mu[FS_m]$ corresponds to the result of a deterministic analysis and is associated with the simulation where all input variables are taken with their mean value (Eq. 3.6). In the remaining $2n$ simulations one variable at a time is increased or decreased by adding or subtracting its standard deviation $\sigma[X_i]$ to its mean value $\mu[X_i]$. The values of minimum Factor of Safety FS_m obtained from these simulations are used to calculate the variance of the minimum

Factor of Safety $\sigma^2[FS_m]$ (Eq. 3.7). The mean and variance of the minimum Factor of Safety FS_m within the failure segment are equal to 1.418 and 0.039 respectively, while outside the failure segment they are equal to 1.779 and 0.059 respectively.

The value of the probability of failure is calculated as the probability to have a Factor of Safety lower than or equal to one and is graphically represented by the shaded areas in Figure 3.17. This probability of failure associated to a flood event has been converted into an annual probability of failure by taking into account the average time interval between flood events (*Chapter 2*).

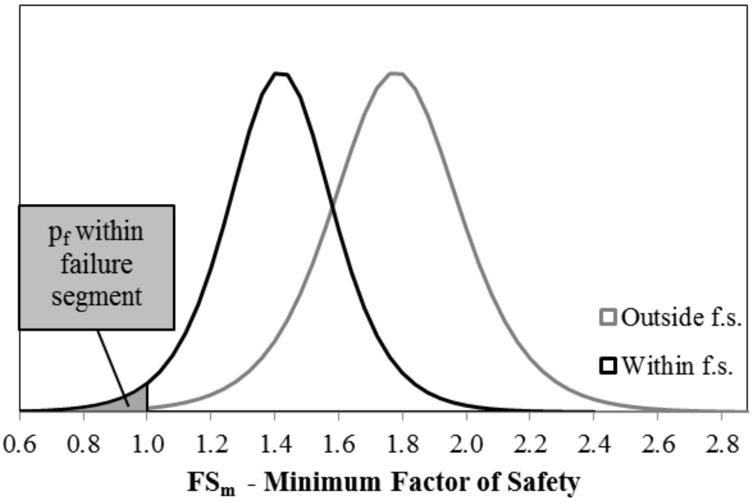

Figure 3.17. Probability of failure for the sections within and outside the failure segment.

The values of the annual probability of failure calculated for the section within and outside the failure segment are equal to 1.7% and 0.23% respectively. These values are consistent with the expected probabilities of failure. The section within the failure segment has experienced one failure in a time of 90-120 years, i.e. the time from the construction of the embankment to the flood event in 1981 when the scarp was observed. Its expected probability of failure is of the order of 1%. The section outside the failure segment has experienced no failures in the 90-120 years since its construction and a significantly lower probability of failure is obtained (<<1%).

3.9 Discussion

Results of the seepage analysis in terms of hydraulic head contours are reported in Figure 3.18. Results are shown for the time step corresponding to the peak of the hydrograph ($t=t_{peak}$) in the mean value (deterministic) simulation. For the section within the failure segment the phreatic surface (bold line in Figure 3.18) reaches the ground surface on the toe of the embankment, while for the cross section outside the failure segment positive pore water pressure does not reach the toe of the embankment as the phreatic surface remains below the ground surface by about 0.7m.

The shape of the phreatic surface is also different for the two sections. The phreatic surface lowers down monotonically outside the failure segment whereas it ‘bulges’ in proximity of the embankment toe within the failure segment. This bulging is due to the upward flow originating from the foundation layer as shown by the velocity vectors in Figure 3.18. In turn, this is generated by the sharp contrast in hydraulic conductivity between the alluvial material below the embankment (k=$4{\cdot}10^{-3}$ m/s) and the lacustrine material on the landside (k=$2{\cdot}10^{-5}$ m/s). The lacustrine material acts as a barrier diverting the water flow upward towards the embankment toe. On the other hand, water flow is not diverted in the section outside the failure segment because there is no contrast in hydraulic conductivity in the horizontal direction.

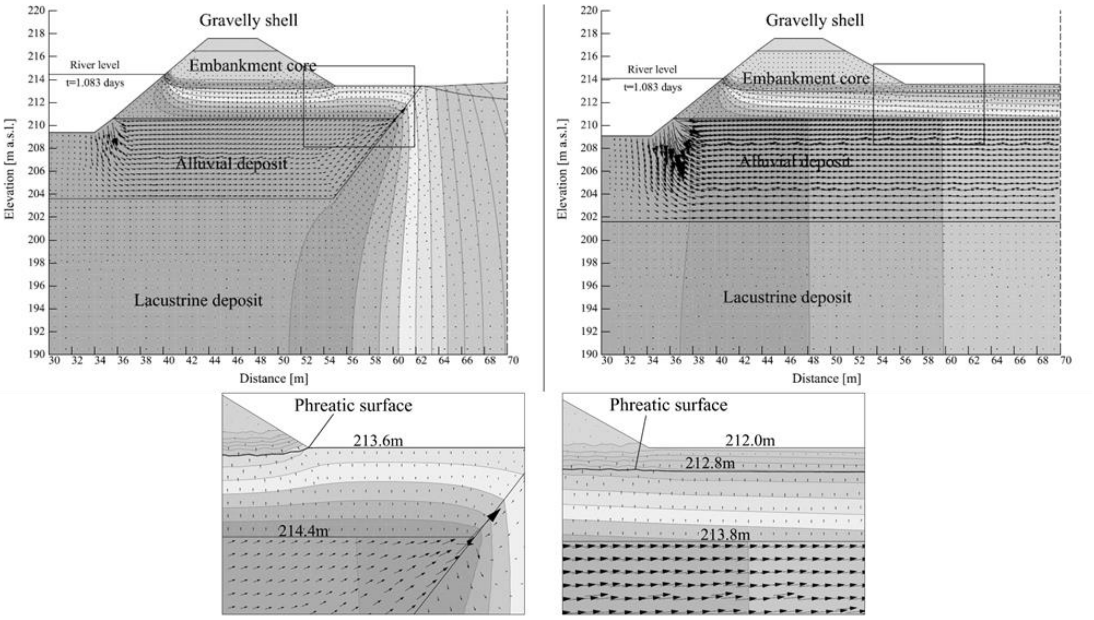

Figure 3.18. Hydraulic head contours and water flow vectors in the transient seepage analysis for the sections within (left) and outside the failure segment (right) at the time of peak.

The different water flow pattern affects the distribution of hydraulic head at the embankment toe. In the failure segment, hydraulic head is not dissipated in the alluvial material below the embankment because its hydraulic conductivity is much higher than the adjacent lacustrine deposit. This makes available the full hydraulic head at the base of the embankment and water flow therefore occurs upward with relatively high hydraulic gradients. This does not occur outside the failure segment as the hydraulic head dissipates uniformly in the homogenous alluvial deposit.

In turn, the different distribution of hydraulic head and, hence, pore-water pressures affect the stability of the embankment. In the section within the failure zone, the build-up of pore water pressure at the toe of the embankment leads to decrease in the shear strength and lower Factor of Safety. Results of the stability analysis resulting in the mean value of the minimum Factor of Safety FS_m are shown in Figure 3.19.

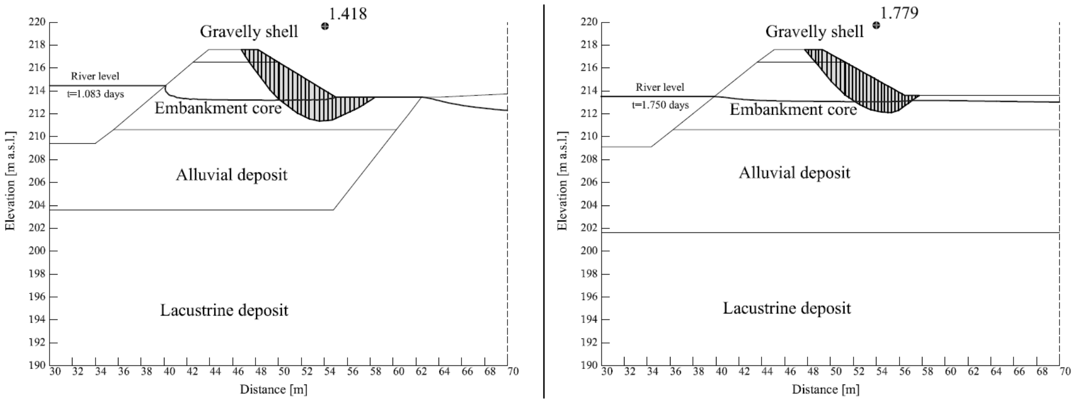

Figure 3.19. Critical slip surface and mean value of the minimum Factor of Safety FS_m for the sections within (left) and outside (right) the failure segment.

The critical slip surface obtained in the mean value (deterministic) simulation has been considered in all the other simulations (Phoon, 2008). Its shape and position compare very favourably with the scarp observed during the flood in 1981, when a cut of about 50 cm of depth was observed roughly in the middle of the crest of the embankment.

The variation of Factor of Safety over time for the mean value simulation is shown in Figure 3.20. The minimum Factor of Safety FS_m is not attained at the same time in both sections. It corresponds to the time of maximum river level (t = t_{peak} = 1.083 days) for the section within the failure segment and t = 1.750 days for the section outside the failure segment. This can be explained by the results of the seepage analysis. The Factor of Safety depends on the value of the pore water pressure along the slip surface. In the section within the failure segment the variation of pore water pressure is immediately affected by the variation of river level because of the high hydraulic transmissivity of the confined alluvial layer beneath the embankment. This is shown by the fact that the maximum pore water pressure for a point at a depth of 0.5 m below the toe of the embankment corresponds to the peak of the hydrograph (Figure 3.20). In the section outside the failure segment pore water pressure along the slip surface is less affected by variations in river level, even if the foundation material is extremely permeable, because water tends to flow towards the landside. The value of pore water pressure along the slip surface increases more slowly because water flow is taking place in the embankment from the river, not from the foundation layer, therefore the seepage process is governed by the hydraulic conductivity of the unsaturated embankment material. For this reason it takes some time for the water front to reach the slip surface, resulting in a delay between the peak of the hydrograph and the time when the maximum pore water pressure and, hence, the minimum Factor of Safety is attained.

The conclusion drawn by this comparison is that the stability of the embankment is strongly affected by the water flow regime, which is in turn strongly controlled by the hydraulic conductivity of the material on the landside of the embankment (and not just by the hydraulic conductivity of the material directly beneath the embankment). In the section outside the failure segment the presence of a permeable foundation layer on its own is not a decisive cause for the development of uplift pressure.

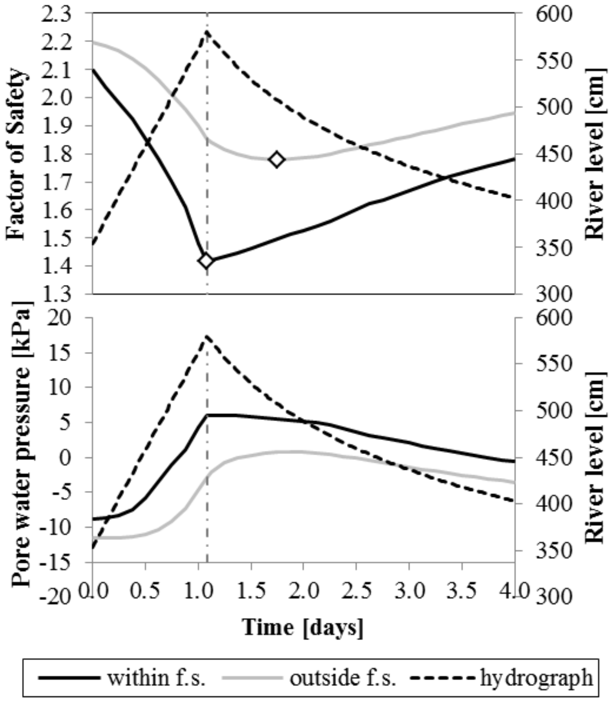

Figure 3.20. Variation over time of Factor of Safety and pore water pressure at the toe of the embankment (depth = 0.5 m) compared to mean hydrograph.

3.10 Conclusions

The paper has presented the case study of the embankment instability along the Adige River. A segment of this embankment experienced instability in the form of a scarp without collapsing, thus offering the chance to investigate soil profile and material properties as they were at the time of instability. Soil profile within and outside the failure segment has been inferred from boreholes, DPH tests and EM scanning. The hydro-mechanical properties of the embankment and its foundation have been characterised through laboratory tests and inverse analysis of water flow based on field measurements below and above phreatic surface.

The hydro-mechanical model has been validated by calculating the annual probability of failure within and outside the failure segment with a FOSM-based approach. The calculated annual probability of failure has shown a good agreement with the observed probability of failure, i.e. of the order of 1% for the section within the failure segment and <<1% for the section outside the failure segment.

The analysis of the flow regime within the segment that experienced failure has shown that the contrast in hydraulic conductivity in the foundation layers on the landside leads to an upward diversion in the water flow and build-up of pore-water pressures at the toe of the embankment. On the other hand, the zone outside the failure segment is characterised by homogeneous foundation layers and the water flow towards the landside is undisturbed, with dissipation of hydraulic head taking place in horizontal direction in the foundation layers beneath the embankment and on the landside.

These results show that the high hydraulic conductivity of the foundation layer does not represent per se a critical condition for the development of uplift pressures at the toe of the embankment. The material outside the embankment footprint can play indeed a key role on the water flow regime and, hence, on the stability of flood embankments. The role of the soil profile on the landside is often overlooked and should be addressed by site investigation.

3.11 Acknowledgements

The authors wish to acknowledge the support of the European Commission via the Marie Curie IEF project RESCUE ‘River flood Embankments Subject to Climate change: Understanding Effects of future floods and novel ‘low-carbon’ adaptation measures’ (PIEF-GA-2013-625258) and the Marie Curie Industry-Academia Partnership and Pathways Network MAGIC ‘Monitoring systems to Assess Geotechnical Infrastructure subjected to Climatic hazards’ (PIAPP-GA-2012-324426). The authors also wish to acknowledge the support of the Autonomous Province of Bolzano (Italy).

4. AN ASSESSMENT OF ERT AS A METHOD TO MONITOR WATER CONTENT REGIME IN FLOOD EMBANKMENTS: THE CASE STUDY OF THE ADIGE RIVER EMBANKMENT

Abstract

Stability of flood embankments is strongly affected by the water flow taking place in the saturated and unsaturated soil. Monitoring of the water flow in flood embankments is therefore essential in the context of flood risk management to predict and prevent failures of embankments. Electrical Resistivity Tomography (ERT) is gaining popularity for its ability to monitor water regime in the subsoil more quickly, cost-effectively and on a larger scale compared to traditional geotechnical monitoring systems that rely on local sensors. This paper presents the application of ERT to the monitoring of water content in a flood embankment on the Adige River in Italy. The resistivity profiles obtained from the ERT measurements were converted into water content profiles via a laboratory-derived relationship between resistivity and water content. At the same time, local sensors that monitor pore water pressure were installed in the saturated and unsaturated zone of the embankment and this allowed reconstructing the water content regime in the embankment via inverse analysis of water flow. This offered the chance to

benchmark ERT-derived water content against independent indirect measurements of water content in the field.

ERT-inferred water content profiles based on laboratory calibration could capture the water content profiles derived from water flow analysis only qualitatively. This was attributed to artefacts in the ERT data inversion arising from the high contrasts in resistivity between different embankment layers. On the other hand, ERT proved to be a valuable tool to quantify the water content in the soil if a field-specific relationship between water content and ERT-measured resistivity is developed.

4.1 Introduction

River embankments are often used as a defence measure to protect people and properties against floods. When the river level changes water flows through the embankment and alters the pore water pressure distribution, and consequently the shear strength of the soil. This may lead to instability of the embankment and its failure to protect the floodplain. Characterisation of water flow is therefore very important to assess the stability of flood embankments and understand their failure mechanisms. Geophysical methods offer an attractive and valuable tool to carry out diffuse monitoring of water flow on geotechnical structures such as flood embankments. Geophysical methods are non-intrusive, cost-effective and can be employed to monitor water flow at a larger scale compared to local sensors.

Electrical Resistivity Tomography (ERT) is a common geophysical investigation technique. It is based on the measurement of apparent resistivity when an electric field is generated by injecting current in the subsoil by means of electrodes. The apparent resistivity is then converted into electrical resistivity of the soil through the inversion process. Electrical resistivity in unsaturated soils is strongly dependent on the moisture content, among other variables such as grain size and temperature (Samouelian, et al., 2005). Resistivity profiles offer a qualitative assessment of water flow in the subsoil, with lower resistivity associated to higher moisture content and higher resistivity associated to low moisture content. For this reason ERT is a versatile tool and has found applications in the monitoring of seepage in earth structures (Johansson & Dahlin, 1996; Lin, et al., 2013).

The relationship between water content and resistivity for a specific soil is described by generalised Archie's law (Archie, 1942). If the calibration parameters of Archie's law can be derived experimentally, either via laboratory testing or in the field, variations in resistivity can be used to quantify variations in moisture content and map water content in the subsoil.

This has found a variety of applications in the monitoring of water regime in the subsoil, from the interaction between soil and vegetation (Fan, et al., 2015) to the detection of permafrost (Hilbich, et al., 2009). It has also found applications in the monitoring of water content in earth structures such as railway embankments (Chambers, et al., 2014) or highway embankments (Gunn, et al., 2015). However, although this technique has been acknowledged as a valuable tool for monitoring water flow in flood prone areas (Brunet, et al., 2010), it has found limited applications in the monitoring of water content in flood embankments.

Interpretation of ERT results can be complicated and affected by uncertainties for several reasons, including anomalies in the resistivity due to improper contact between electrodes and ground surface, numerical artefacts generated during the inversion process, other variables influencing the resistivity values (e.g. temperature) and inaccuracies in the calibration parameters of Archie’s law. It is therefore essential to validate water content values derived from ERT data against independent direct or indirect measurements of water content.

In this paper the soil electrical resistivity data derived from ERT measurements are used to map water content profiles in a flood embankment located on the Adige River in the North of Italy. The soil specific relationship between soil resistivity and water content was derived experimentally in the laboratory using Time Domain Reflectometry (TDR) on intact and compacted samples collected from the embankment. A geotechnical monitoring system consisting of piezometers and tensiometers was installed to measure pore water pressure above and below the phreatic surface respectively in the same location where ERT measurements were carried out. This offered the chance to benchmark ERT-derived water content profiles against the water content derived from numerical simulations based on the inverse analysis of the piezometer and tensiometer data.

4.2 The case study

The study site is located along the Adige River, in the North of Italy, near the village of San Floriano. The soil profile was characterised from borehole logs and DPH tests carried out on a 500 m segment from chainage km 122.000 to km 122.500 (*Chapter*

3). The geophysical investigation focused on the area between chainage km 122.410 and km 122.460. The soil profile of a representative cross section of this segment is shown in Figure 4.1. This area was chosen because a monitoring system consisting of tensiometers and piezometers is installed in the same segment, thus offering the chance to compare water content estimated from resistivity measurements to water content based on inverse analysis of the monitoring data.

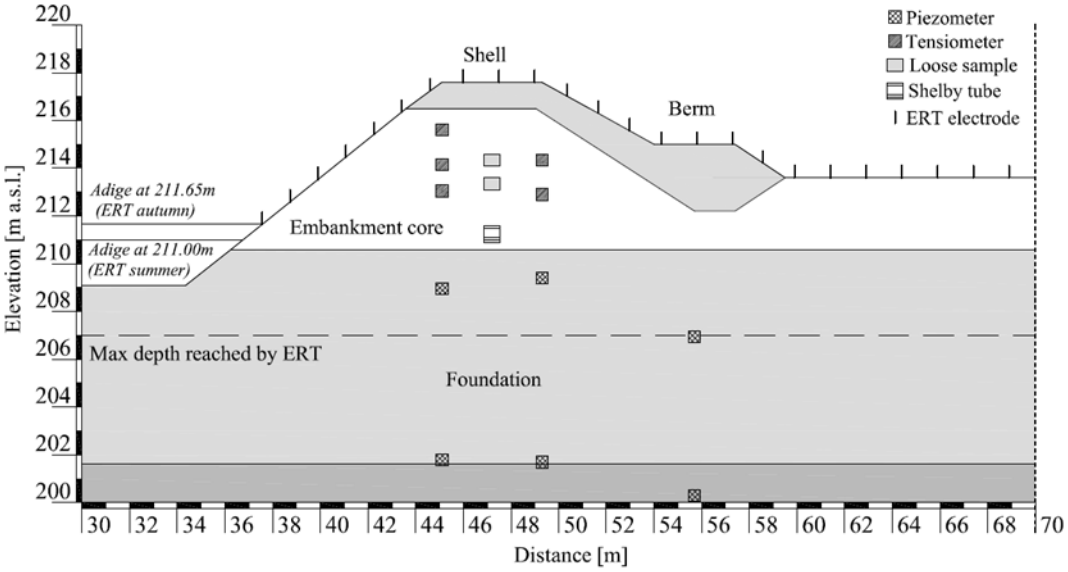

Figure 4.1. Cross-section of the embankment with field instruments and samples collected for material characterisation.

Two materials can be identified in the embankment. The shell surrounding the core of the embankment and the berm built on the landside are made of coarse gravel and sand, while the core of the embankment is a brown sandy silt of fluvial origin and has a thickness of about 5m. The foundation material is a coarse sand of fluvial origin corresponding to the ancient riverbed of the Adige River.

Intact samples were collected from the embankment core in a Shelby tube in order to characterise experimentally the relationship between resistivity and water content via laboratory testing. Additional samples were collected at different depths for the geotechnical characterisation of the material (Figure 4.1). The grain size distribution for the material in the embankment core was obtained from loose samples taken at a depth of 3.3 m and is shown in Figure 4.2.

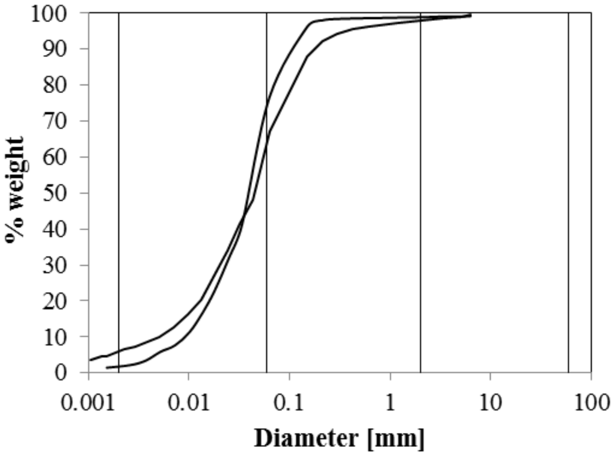

Figure 4.2. Grain size distribution for two ‘loose’ samples collected from the embankment core at a depth of 3.3m.

4.3 Laboratory determination of the relationship between resistivity and water content

4.3.1 Electrical resistivity measurements with TDR

4.3.1.1 Theoretical background

Time Domain Reflectometry (TDR) is a technique to measure the time-domain envelopes of electromagnetic waves propagating through waveguides installed into the soil. It can be used to measure the soil electrical conductivity via the measurement of the standing wave ratio.

The TDR system includes a step pulse generator which generates electromagnetic waves and an oscilloscope which records voltage variations. Electromagnetic waves are transmitted through a probe connected to the oscilloscope and pulse generator via a coaxial cable (Tarantino, et al., 2008). Multiple reflections and transmissions of the electromagnetic wave take place at the head and at the end of the probe, until a stable level (standing wave) is achieved.

TDR systems often return the signal recorded by the oscilloscope in terms of reflection coefficient R:

$$R(t) = \frac{V(t) - V_0}{V_0} \qquad \textbf{\textit{Eq. 4.1}}$$

where V is the reflected voltage and V_0 is the incident voltage, i.e. the voltage going into the head of the probe.

Topp, et al. (1988) have shown that the bulk electrical conductivity σ of a soil can be measured by using TDR and applying the Giese & Tiemann (1975) equation:

$$\sigma = \frac{1}{Z_c}\frac{\varepsilon_o c Z_p}{L}\left[\frac{1 - R_\infty}{1 + R_\infty}\right] \qquad \textbf{\textit{Eq. 4.2}}$$

where ε_0 is the permittivity of free space ($8.854 \cdot 10^{-12}$ F m^{-1}), c is the speed of light ($3 \cdot 10^{8}$ m s^{-1}), L is the probe span (m), R_∞ the final (standing wave) reflection coefficient returned by the oscilloscope, Z_c is the impedance of the cable tester, and Z_p is the impedance of the probe.

By introducing the probe constant K_p

$$K_p = \frac{\varepsilon_o c Z_p}{L}$$ ***Eq. 4.3***

Eq. 4.2 can be rewritten as follows:

$$\sigma = \frac{K_p}{Z_c}\left[\frac{1 - R_\infty}{1 + R_\infty}\right]$$ ***Eq. 4.4***

The probe constant K_p can be obtained by measuring the reflections occurring at infinite time in solutions of known electrical conductivity (Zegelin, et al., 1989) or calculated by using Eq. 4.3 with the impedance of the probe Z_p calculated as in Ball (2002):

$$Z_p = \frac{1}{2\pi n}\sqrt{\frac{\mu_0}{\varepsilon_0}}\, ln\left(H + \sqrt{H^2 - 1}\right)$$ ***Eq. 4.5***

with

$$H = \frac{(s^2 - a^2)^n - a^{2n}}{a^n((s + a)^n - (s - a)^n)}$$ ***Eq. 4.6***

where μ_0 is the magnetic permeability in vacuum (1.26 10^{-6} N A^{-2}), ε_0 is the permittivity of free space, a is the radius of the single conductor, s is the spacing between conductors and n is the number of external conductors (n=2 for trifilar probe). The nominal value of the probe constant K_p is also often provided by the manufacturer.

4.3.1.2 Signal correction

Correction of the TDR signal is needed when the reflection measured in air is not equal to the theoretical value of 1 and when the reflection measured on the short circuited probe is not equal to the theoretical value of -1. Castiglione & Shouse (2003) have suggested correcting the reflection coefficient to account for additional losses in the cables as follows:

$$R_{\infty,c} = \frac{R_{air} - R_{\infty}}{R_{\infty} - R_{sc}} \qquad \textbf{\textit{Eq. 4.7}}$$

where R_{∞} is the reflection coefficient at infinite time, R_{air} is the reflection coefficient measured in air and R_{SC} is the reflection coefficient measured on the short-circuited probe. If $R_{\infty,c}$ is substituted for R_{∞}, the conductivity of the sample can finally be calculated from Eq. 4.4 as follows:

$$\sigma = \frac{K_p}{Z_c}\left[\frac{1 - R_{\infty,c}}{1 + R_{\infty,c}}\right] \qquad \textbf{\textit{Eq. 4.8}}$$

The electrical resistivity ρ is the reciprocal of the electrical conductivity σ, so it can be calculated as:

$$\rho = \frac{1}{\sigma} \qquad \textbf{\textit{Eq. 4.9}}$$

4.3.1.3 Calibration of the resistivity function

Two 75 mm long TDR probes with three rods were used for the measurements. The TDR probes (Campbell Scientific CS640) were calibrated to establish the relationship between the conductivity and the reflection coefficients that the probes return by measuring the reflections occurring at infinite time in sodium chloride (NaCl) solutions of known electrical conductivity. The conductivity of NaCl solutions is related to the molality of the solution (Weast, et al., 1985). Solutions with electrical conductivity ranging between 1,500-12,000 μS/cm were prepared by mixing oven-dried salt and demineralised water in a large plastic container. To ensure that the container did not affect the TDR measurements, solutions were prepared in a container wider than the sampling volume, which has diameter equal to the distance between the external rods (Ferre, et al., 1998). The TDR probe was then fully inserted into the solution and the final reflection R_∞ was measured and corrected as shown in Eq. 4.7 to account for the dissipation of the signal in the cables.

The slope of the calibration curve (Figure 4.3) represents the ratio K_p/Z_c (Eq. 4.8) for each probe. The obtained values are equal to 899 μS/cm and 871 μS/cm respectively. These values derived from the probe-specific calibration were checked against the values derived from the manufacturer specifications. The probe constant K_p provided by the manufacturer is equal to 6.3 S/m Ω. Assuming a value of Z_c equal to 63.3 Ω for the impedance of the cable (Tarantino & Pozzato, 2008) a value of K_p/Z_c equal to 990 μS/cm is obtained, which compares favourably with the measured value.

Moreover, the probe impedance Z_p was calculated using Eq. 4.5 and a value of 183Ω was obtained (for s=7.705 mm and a=0.795 mm). By substituting this value in Eq. 4.3 and considering the same value of Z_c equal to 63.3 Ω, a value of K_p/Z_c equal to 1018 μS/cm was found, which again compares favourably with the value measured from the specific calibration.

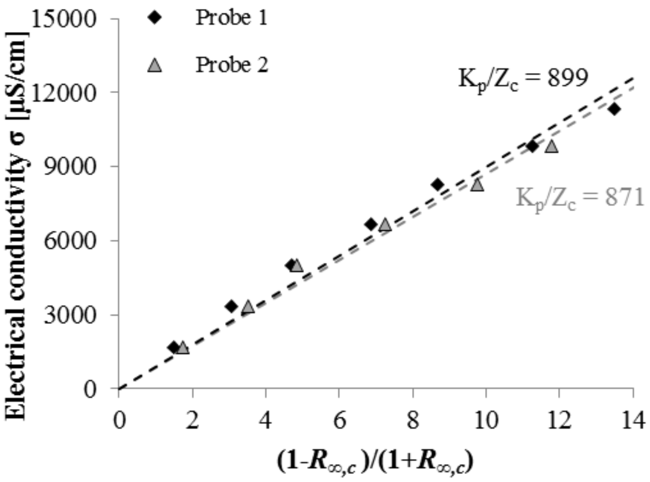

Figure 4.3. Calibration curves for the two TDR probes.

4.3.2 Experimental procedure

4.3.2.1 Sample preparation

Three cylindrical intact samples 100 mm high, 75 mm diameter were taken at depths of 6.0, 6.5 and 6.6 m from the crest of the embankment.

A 1 cm high slice of each sample was cut and oven-dried to estimate the initial volumetric water content. Samples were air-dried in steps and the mass of water evaporated upon each step was used to calculate the volumetric water content reached at the end of each evaporation step. This water content θ_{target} is given by:

$$\theta_{target} = \frac{m_w}{\gamma_w V_c} \qquad \textbf{\textit{Eq. 4.10}}$$

where m_w is the mass of water in the sample at the time of measurement, γ_w is the unit weight of water at 20°C and V_c is the volume of the cylindrical sample.

After each evaporation step each sample was sealed in a plastic bag for 24 hours to let the water content homogenise before taking the TDR measurement. The TDR probe was initially slowly pushed centrally into the sample to avoid deforming the probe rods and it was left in the sample for all measurements.

Loose material collected from the embankment at a depth between 3 m and 4.5 m was used to prepare eleven samples which were compacted to a target value of dry density of 1.52 g/cm^3 to replicate the dry density in the field (*Chapter 3*). The samples were prepared with target volumetric water contents θ_{target} ranging between 0.14 and 0.32, calculated as:

$$\theta_{target} = \rho_{dry} \frac{m_w}{m_s} \gamma_w \qquad \textbf{\textit{Eq. 4.11}}$$

where ρ_{dry} is the dry density and m_w and m_s are respectively the mass of water and the mass of soil used to prepare the sample.

Samples were prepared by mixing the oven dried soil with fluids at different conductivities σ_w to evaluate the influence of the fluid on the bulk electrical resistivity. In particular, demineralised water, NaCl solution mimicking electrical resistivity of the Adige River, and NaCl solution having electrical resistivity much higher than the Adige River were considered. The Adige-like solution was prepared by measuring the electrical conductivity of the water collected from the Adige River and reproducing similar electrical conductivity by adding NaCl to demineralised water. Details about the preparation of the samples are reported in Table 4.1.

Sample	θ_{target}	w	Water	σ_w [S/m]
D1	0.14	0.09	Demineralised	0.00005
D2	0.21	0.14	Demineralised	0.00005
D3	0.32	0.21	Demineralised	0.00005
A1	0.16	0.11	Adige-like	0.02
A2	0.26	0.17	Adige-like	0.02
A3	0.21	0.14	Adige-like	0.02
A4	0.32	0.21	Adige-like	0.02
A5	0.15	0.10	Adige-like	0.02
A6	0.25	0.16	Adige-like	0.02
S1	0.15	0.10	Saline	0.10
S2	0.25	0.16	Saline	0.10

Table 4.1. Compacted samples prepared at different target water contents and with different pore water.

For each sample, the dry soil was spread on a tray in a thin layer, sprayed with water and mixed carefully to avoid the formation of lumps. To obtain a uniform value of water content the samples were prepared in two steps. Half of the soil was spread in a thin layer (~1mm) and wetted with half of the amount of water; after mixing, the second half of soil was added on the tray, wetted with the remaining water and mixed with the first half sample. Each sample was left in a sealed plastic bag for 24 hours to let the water content homogenise.

The samples were compacted in a mould having diameter equal to 100 mm and height equal to 120 mm. For the compaction each sample was divided in three equal parts. Each part was put in the mould and compacted until the layer reached the required thickness of 40 mm. The samples were compacted with a standard compaction hammer, having weight equal to 4.5 kg and a drop of 457 mm. TDR measurements were taken on each sample immediately after compaction and then the samples were discarded in order to keep under control the salt concentration and therefore fluid conductivity for each sample.

4.3.2.2 Water content

For every measurement the water content was determined as in Topp, et al. (1980):

$$\theta_{Topp} = -5.3 * 10^{-2} + 2.92 * 10^{-2} K_a - 5.5 * 10^{-4} {K_a}^2 + 4.3 * 10^{-6} {K_a}^3 \qquad \textbf{\textit{Eq. 4.12}}$$

where K_a is the apparent dielectric permittivity of the sample. The value of K_a was obtained from the propagation velocity of the pulse in the probe as described in Tarantino, et al. (2008):

$$K_a = \left(c \frac{t_{end} - t_{probe}}{2L_e} \right)^2 = \left(c \frac{t_{end} - (t_{head} + \Delta t)}{2L_e} \right)^2 \qquad \textbf{\textit{Eq. 4.13}}$$

where L_e is the electrical length of the probe, c is the speed of light (3 10^9 m/s), t_{end} is the time corresponding to the reflection at the end of the rods, t_{probe} is the time at which the wave enters the probe electrodes, t_{head} is the time at which the wave enters the head of the probe and Δt is the time interval between t_{head} and t_{probe}. The values of L_e and Δt were obtained from the probe calibration in air and water (Robinson, et al., 2003), while the times t_{end} and t_{head} were obtained graphically from the waveform in terms of reflection coefficient as shown in Figure 4.4. The time t_{head} corresponds to the first dip in the waveform signal, while the time t_{end} can be found at the intersection point between the tangent to the second rising limb at the inflection point and the horizontal tangent at the base of the signal (Baker & Allmaras, 1990).

The volumetric water content calculated using Topp's equation was compared to the imposed water content θ_{target} for the compacted samples and a good agreement was found as shown in Figure 4.5. Intact samples are not included in Figure 4.5 because the measurement of the volumetric water content was affected by inaccuracies in the measurement of the total volume after extrusion from the sampler.

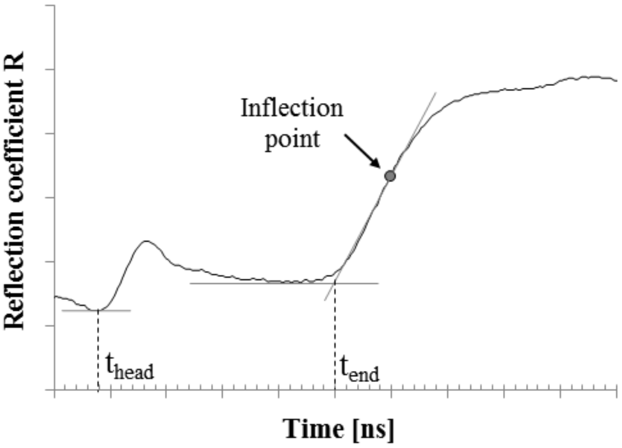

Figure 4.4. Typical waveform signal returned by TDR in terms of reflection coefficient R.

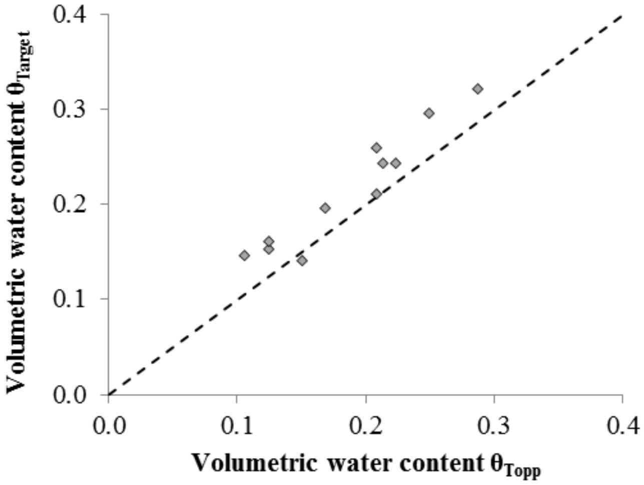

Figure 4.5. Comparison between volumetric water content calculated using Topp's equation θ_{Topp} and estimated volumetric water content θ_{Target}.

4.3.2.3 Relationship between resistivity and water content

The electrical resistivity of a porous medium depends on its moisture content. The resistivity and the volumetric water content of an unsaturated soil can be related via Archie's law (1942) as:

$$\rho = k \cdot n^{-p} \cdot {S_r}^{-m} \qquad \textbf{\textit{Eq. 4.14}}$$

where ρ is the electrical resistivity of the unsaturated soil, n is the porosity, S_r is the degree of saturation and k, p and m are coefficients depending on the type of soil, with k also dependent on the resistivity of the fluid in the pores. Experimental evidence has shown that the fitting parameters p and m can be assumed to have the same value, leading to the formulation of the generalised Archie's law (Shah & Singh, 2005), which can be used to relate electrical resistivity to volumetric water content θ as follows:

$$\theta = \alpha\rho^{-\beta} \qquad \textbf{\textit{Eq. 4.15}}$$

For both the intact and compacted samples the values of the fitting parameters α and β were found by plotting the measured resistivity against the volumetric water content calculated with Eq. 4.12 and fitting the data points with the expression in Eq. 4.15. The results are shown in Figure 4.6.

The data points corresponding to samples prepared with demineralised water show a larger value of resistivity at the same water content compared to sample prepared with saline water. This trend is consistent with expectations, being the conductivity of the demineralised water much lower than the one of the saline water. However, when comparing the data points corresponding to the resistivity of the Adige River to the ones corresponding to saline water, no significant difference can be observed as both sets of data points align on the same curve. This shows that although the different resistivity of the fluid in the pores plays a role in the measured bulk resistivity, its effect is not proportional to the difference in the resistivity of the fluid on its own. This is reasonably associated with the electrical interaction between clay particles and ions in the water. The difference in the resistivity values measured for the compacted samples is comparable to the scattering in the data points corresponding to measurements taken on intact samples, which is only generated by the natural variability of the soil in the samples. For this reason all the experimental data points were fitted by the same power function with α=4.166 and β=0.622.

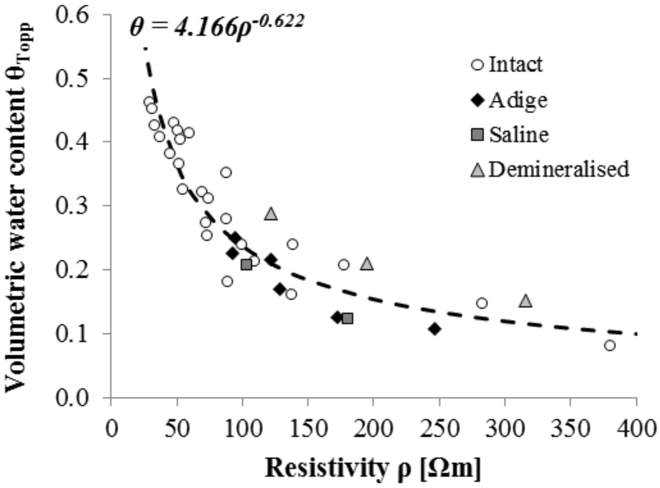

Figure 4.6. Relationship between resistivity and volumetric water content.

4.4 ERT data

4.4.1 Field measurements

Electrical resistivity tomography (ERT) is based on the measurement of resistivity in the soil using a large number of electrodes placed at the ground surface. 2D ERT measurements were taken in two surveying campaigns on the Adige River embankment. The first campaign was carried out in the wet season and one week after a moderate flood (autumn 2014), while the second campaign was carried out during the dry and warm season (summer 2015). The river levels recorded during both surveying campaigns are shown in Figure 4.1. The surveys were aimed at mapping the water content in the unsaturated zone above the phreatic surface.

Measurements were taken along the longitudinal and cross-sectional profile of the embankment. For the longitudinal profile, electrodes were installed on the crest of the embankment along a 50m segment (chainage km 122.415-122.460) with 1m spacing between the electrodes. For the cross-sectional profiles, electrodes were installed along the topographic profile of the embankment in a 40 m long array, starting from the river level on the riverside and progressing towards the toe of the embankment, with an electrode spacing of 1.5m as shown Figure 4.1. Measurements were taken along three cross-sections located at chainage km 122.425, km122.445 and km122.452. A Schlumberger array configuration was chosen for the ERT measurements and the device ARES (GF Instruments, Czech Republic) was used. The maximum penetration depth from the crest of the embankment is about 10 m, therefore allowing measuring the resistivity in the entire unsaturated zone in the embankment core and also below the phreatic surface.

4.4.2 Resistivity from ERT measurements

2D resistivity profiles were compiled using the programme Res2Dinv (GEOTOMO Software - Malaysia). Data points with out-of-range values of resistivity were removed from the measured datasets before the inversion. These values were associated with inadequate electrode grounding, i.e. anomalous electrode contact resistance on the asphalt cover on the crest. The proportion of the excluded data did not exceed 5% of the total data at any of the measured profiles. The robust least-square inversion method was selected because a sharp contrast in resistivity was expected between the gravelly shell layer and the silty material in the core of the embankment (Geotomo, 2003). The RMS error at the 5th iteration was considered acceptable (<10%) for all the measurements. The topographic profile was included in the modelling mesh. Examples of resistivity contours obtained from the inversion are shown in Figure 4.7 for one representative cross section. The areas of high resistivity close to the ground surface below the crest of the embankment correspond to the shell layer which is made of gravelly material. The pavement on the crest of the embankment prevents infiltration of water from the surface, leading to a very high resistivity in the dry gravel. This is more evident during summer because on the sloping sides of the embankment the shallow layer is also dry due to evaporation. The high resistivity at the toe of the berm on the landside is associated to a drainage system. For depths greater than 7 m the material shows a uniform resistivity in the range 50-100 Ωm. This resistivity is associated to the saturated foundation material.

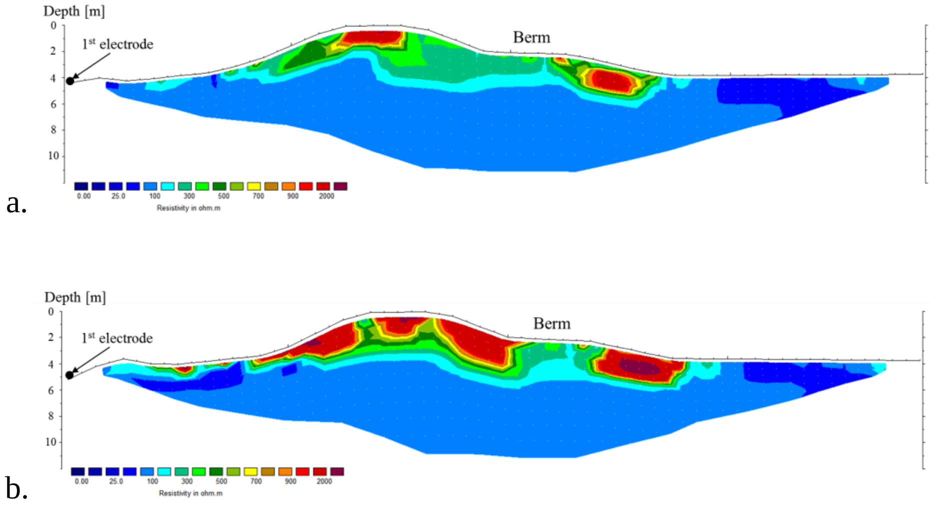

Figure 4.7. Resistivity contours obtained from the inversion of ERT data at chainage km 122.425 in autumn (a) and summer (b).

4.4.3 Effect of temperature

The resistivity values were corrected to account for temperature changes in the subsurface soil due to seasonal variations according to Eq. 4.16 (Keller & Frischknecht, 1966):

$$\rho_{20} = \rho \cdot \left(1 + b(T - 20°)\right) \qquad \textbf{\textit{Eq. 4.16}}$$

where ρ_{20} is the resistivity at a reference temperature of 20°C, ρ is the resistivity obtained from the inversion of the ERT data, b is taken equal to 0.02 $°C^{-1}$ (Hayley, et al., 2007) and T is the temperature in the subsurface soil.

Temperature variations in the subsoil can be described by the following equation (Kasuda & Archenbach, 1965):

$$T(t,z) = T_m - T_a e^{\left(-z\sqrt{\frac{\pi}{365D}}\right)} \cos\left(\frac{2\pi}{365}\left(t - t_s - \frac{z}{2}\sqrt{\frac{365}{\pi D}}\right)\right) \qquad \textbf{Eq. 4.17}$$

where T is the temperature at time t (expressed in days of the year) and depth z, T_m is the yearly mean temperature at ground surface, T_a is the amplitude of the yearly temperature variation at ground surface, t_s is the phase offset i.e. the day of the year corresponding to the minimum yearly temperature (Table 4.2). D is the soil's thermal diffusivity which can be calculated as:

$$D = \frac{K}{\rho_s C} \qquad \textbf{Eq. 4.18}$$

where ρ_s is the average soil density (kg/m^3), C the soil specific heat capacity (J/kg K) and K the soil thermal conductivity (W/m K). These parameters change with the water content in the soil, which is not known a priori, therefore an average value was assumed between the values of dry soil and fully saturated soil as reported in the literature (Pal Arya, 2001).

	2014 (autumn)	***2015 (summer)***
T_m [°C]	13.9	13.8
T_a [°C]	13.6	15.9
t_s [day]	360	32
t_{ERT} [day]	316	175

Table 4.2. Yearly temperature data for San Floriano in 2014 and 2015.

The temperature profiles in the subsurface soil obtained for both surveying campaigns are shown in Figure 4.8. Although the temperature at ground surface is significantly different for the two seasons, temperature in the subsurface tends to level towards the annual mean temperature of 13°C and the effect of seasonal variations does not affect the temperature in the subsoil for depths greater than 10m.

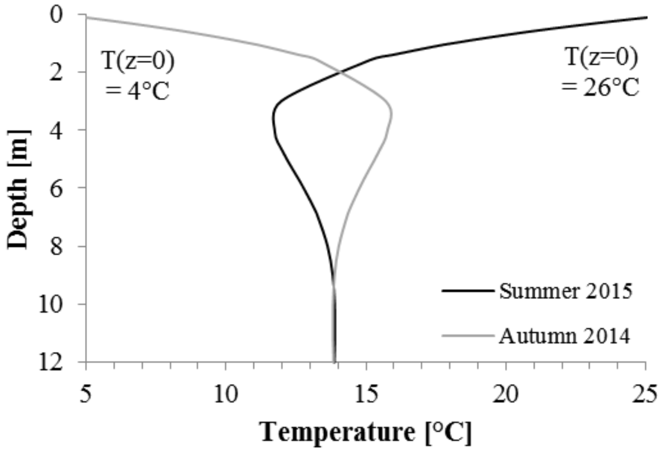

Figure 4.8. Temperature profiles in the subsurface at the time of ERT measurements.

The average corrected resistivity profile below the crest of the embankment is shown in Figure 4.9 for one representative cross-section. Resistivity at a given depth is the average measured across the crest footprint. The values of corrected resistivity in summer are much higher than the ones measured in autumn at shallow depths. This appears to be consistent with a lower phreatic surface, which generates higher suction and, hence, lower water contents. At greater depths (below 212m a.s.l.) no significant difference can be observed between the two seasons and the resistivity has a constant value of about 50 Ωm. This part of the embankment is below the phreatic surface, therefore this value of resistivity is not affected by the moisture content and corresponds to the resistivity measured for the fully saturated material.

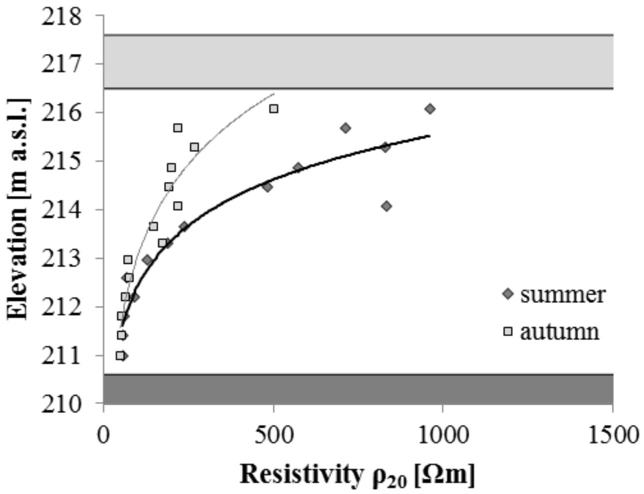

Figure 4.9. Average corrected resistivity profile for the cross-section at chainage km 122.425 in summer 2015 and autumn 2014.

4.5 Inverse analysis of monitoring data

To benchmark the water content profiles obtained from the ERT measurements, numerical simulations of water flow in the embankment at the time of ERT measurements were carried out. Since the three cross-sections where ERT measurements were taken are very close, a single geotechnical model was considered (Figure 4.1). The numerical model was calibrated by inverse analysis of the water flow based on the measurements of the piezometers and tensiometers installed in the field. The values of the saturated hydraulic conductivity of the materials in the core of the embankment and in the foundation were obtained from the inverse analysis of the monitoring data (*Chapter 3*). The water retention curve of the embankment core material (Figure 4.10) was derived experimentally in the laboratory on specimens collected at different depths, while the unsaturated hydraulic conductivity was derived from the water retention curve using Van Genuchten's model (Van

Genuchten, 1980). More details about the numerical model can be found in *Chapter 3*.

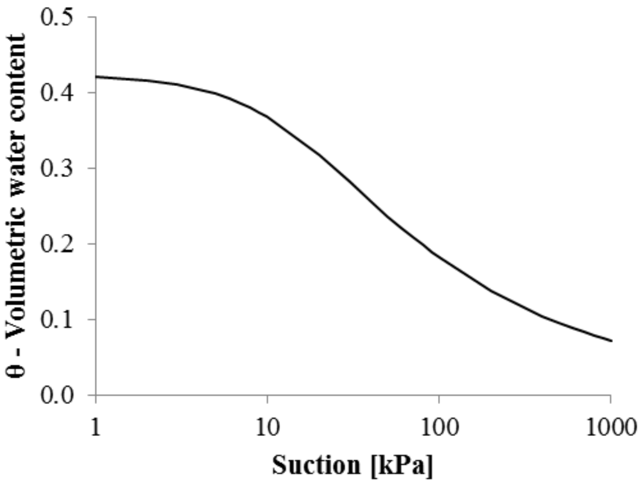

Figure 4.10. Water retention curve of the material in the embankment core.

The hydrograph in the water flow simulations is given by the level of the Adige River at the study site, which is recorded by a hydrometer and is shown in Figure 4.11 for the months corresponding to the two ERT measurement campaigns. In June 2015 no significant change of the river level was observed in the weeks leading up to the time of ERT measurements, therefore steady-state conditions were considered in the water flow simulations. In November 2014 a moderate flood was observed a few days before the ERT measurements, therefore transient conditions were taken into account in the water flow simulation to account for the variations of river level in the ten days preceding the ERT measurement.

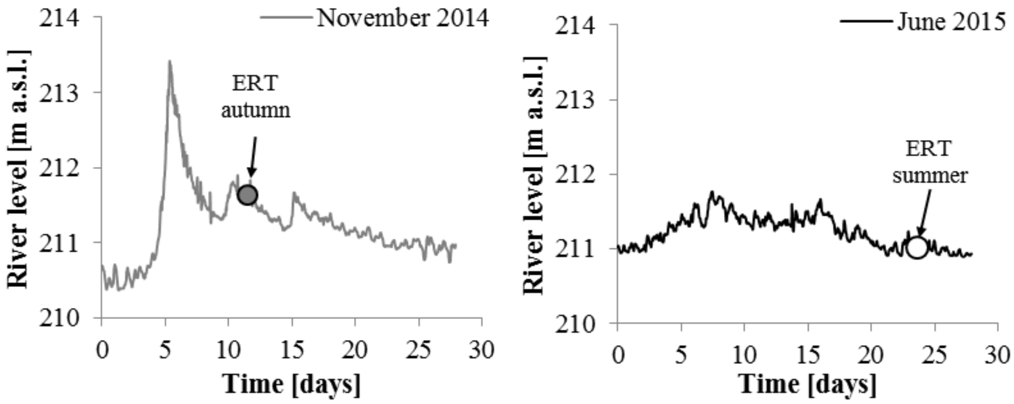

Figure 4.11. River level variations recorded in the months of the ERT measurement campaigns.

4.6 Discussion

The average resistivity profiles deriving from ERT measurements were converted in volumetric water content profiles using the relationship between resistivity and volumetric water content obtained in the laboratory tests (Figure 4.6).

The comparison of water content profiles obtained from the ERT data and from the inverse analysis of monitoring data is shown in Figure 4.12 for both seasons.

From a qualitative point of view the comparison between water content profiles shows a good match between the water contents derived from ERT and the numerical simulation of water flow. The profiles show the same trend, with increasing water content with depth in the unsaturated area and a constant water content, corresponding to the saturated one, in the saturated zone.

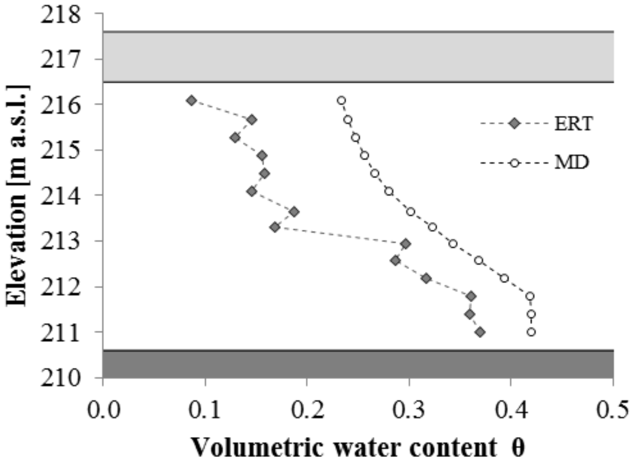

a.

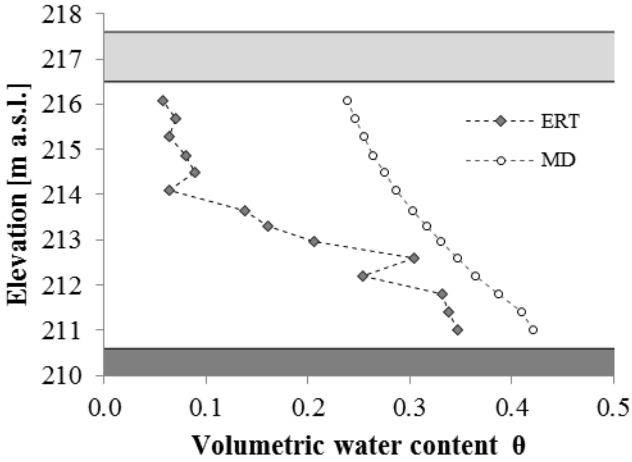

b.

Figure 4.12. Volumetric water content profiles obtained from ERT data (θ_{ERT}) and from inverse analysis of monitoring data (θ_{MD}) in (a) autumn and (b) summer.

However, from a quantitative point of view the water content obtained from ERT data does not seem to give an accurate estimate of the water content in the embankment. The water content derived from ERT measurements is always lower than the one obtained from numerical simulations, meaning that the resistivity returned by the inversion of the ERT data is greater than the one obtained from TDR measurements in the laboratory. This may be due to artefacts associated to the inversion process. The high contrast in resistivity between layers has been acknowledged as a source of artefacts during the inversion in several applications (Carey, et al., 2017; Hilbich, et al., 2009; Rings, et al., 2008), raising questions about the reliability of resistivity values obtained in the areas of the model where such contrasts are found. For the embankment in San Floriano, the resistivity returned by the inversion in the gravelly shell layer reaches values as high as 2200 Ωm in autumn and 3500 Ωm in summer. The high contrast between the resistivity of the gravelly shell and the resistivity of the silty material in the embankment core may therefore be the source of the mismatch observed in terms of water content.

The mismatch is more evident for the summer measurement, when the evaporation from ground surface is more intense and leads to a very dry gravelly shell layer. The higher contrast in resistivity values at the boundary between the two layers would explain why the difference between the ERT-derived water content and the one obtained from the inverse analysis of monitoring data is more significant for measurements taken during summer.

This issue can be addressed by deriving a field specific relationship between the resistivity returned by the inversion of ERT data and the water content. This can be achieved by having an independent measurement of water content at the same time as the ERT measurement to relate the two variables (Fan, et al., 2015). To test this approach, a field specific water content-resistivity relationship was derived using the average resistivity profile obtained from the longitudinal ERT measurements carried out on the crest of the embankment in the first measurement campaign (autumn

2014). This resistivity profile has been associated to the water content profile obtained from the numerical simulations based on the inverse analysis of monitoring data. The field specific relationship is shown in Figure 4.13 together with the curve obtained from the laboratory testing. The two curves diverge significantly for values of resistivity higher than 100 Ωm, with the field-derived curve showing much higher values of water content corresponding to the same resistivity.

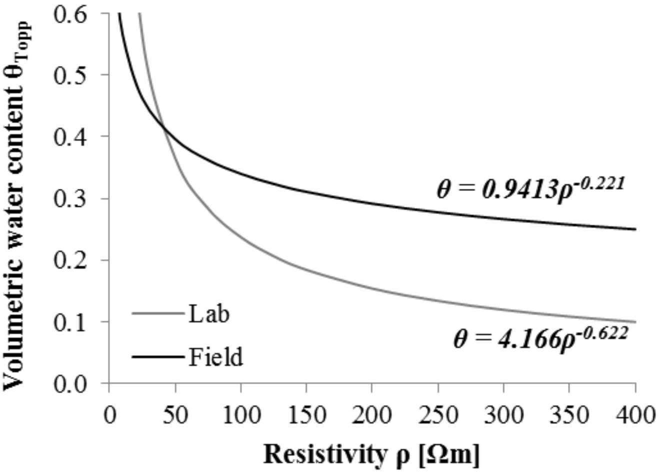

Figure 4.13. Relationship between resistivity and volumetric water content derived from laboratory measurements and from inversion of ERT data.

The field specific water content-resistivity relationship built on the autumn 2014 dataset was then validated against its capability to simulate the water content on the summer 2015. To this end, the field specific water content-resistivity relationship was used to convert the resistivity profiles obtained from the ERT on the cross section for the summer 2015 campaign. As shown in Figure 4.14a, there is a satisfactory quantitative prediction of the ERT-based water content compared with the one derived from the water flow analysis.

The same figure also shows the water content profile derived from the ERT on the cross section in the autumn 2014 campaign. The good match with the water content derived from the water flow analysis is trivial because essentially these same ERT data have been used to construct the water content-resistivity relationship.

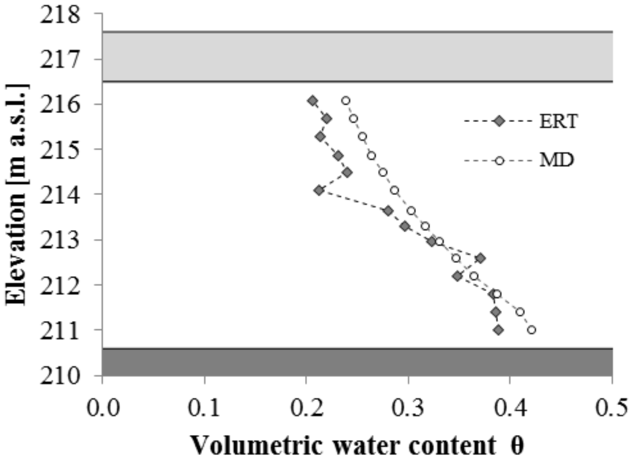

a.

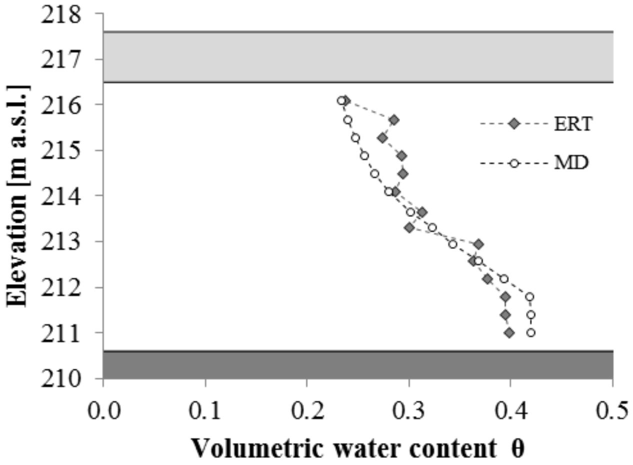

b.

Figure 4.14. Volumetric water content profiles obtained from ERT data (θ_{ERT}) and from inverse analysis of monitoring data (θ_{MD}) using a field specific relationship between resistivity and water content in (a) summer and (b) autumn.

These results indicate that ERT may be a suitable method to quantify volumetric water content in the subsoil, provided that a direct or indirect measurement of water content is available to calibrate a field-based relationship between the ERT derived resistivity and the water content.

4.7 Conclusions

The paper has presented an application of ERT technique to assess water content in a flood embankment on the Adige River, where a monitoring system consisting of piezometers and tensiometers is installed. The relationship between water content and resistivity expressed by Archie's law has been characterised in the laboratory using TDR on intact and compacted samples collected from the embankment. This allowed converting the temperature-corrected resistivity profiles derived from ERT measurements along the cross section of the embankment into water content profiles.

Data from the monitoring system have been used to calibrate a numerical model to analyse water flow in the embankment via inverse analysis. Comparison of ERT-derived water content profiles with water content profiles derived from water flow simulations has shown that ERT can capture the qualitative trend of water content variations in the embankment. However, the high resistivity contrasts between the silty material in the core of the embankment and the gravelly shell layer on the top surface can affect the quantitative interpretation of the results. When there are strong contrasts in the ERT derived resistivity profiles the results tend to be less reliable because of artefacts generated by the inversion process. In this case, an experimental field-calibrated relationship between resistivity and water content can be developed in order to obtain a satisfactory quantitative assessment of the water content. This can be achieved by coupling ERT with more traditional geotechnical monitoring systems based on the use of local sensors, to have an initial direct or indirect measurement of water content in the field.

ERT has proven to be a quick and cost effective tool to assess the water regime in earth structures such as flood embankments. This technique can be easily applied to identify patterns of water flow and anomalies in the moisture content in the soil, which in turn can provide valuable information about the stability of flood embankments.

4.8 Acknowledgements

The authors wish to acknowledge the support of the European Commission via the Marie Curie Industry-Academia Partnership and Pathways Network MAGIC ‘Monitoring systems to Assess Geotechnical Infrastructure subjected to Climatic hazards’ (PIAPP-GA-2012-324426). The authors also wish to acknowledge the support of the Autonomous Province of Bolzano (Italy).

5. DISCUSSION AND CONCLUSIONS

The stability analysis of flood embankments requires the use of flexible approaches that can be easily applied to assess the performance of long segments of embankment. The aim of this thesis was therefore to develop an accessible probabilistic approach for the stability analysis of flood embankments and to provide a method for the characterisation of the hydro-mechanical model of the embankment. The deterministic characterisation may be based on the results of field monitoring; however, this may prove difficult to achieve on a large scale for linear structures like flood embankments. To address this issue this thesis has assessed the use of suitable techniques for the monitoring of water regime in these structures, focusing on ERT.

In particular, the thesis focused on three main objectives:

1. To develop and validate a probabilistic method to assess the probability of failure of flood embankments which is affordable and easy to apply in routine hazard assessment;
2. To characterise the hydro-mechanical model of the embankment for the stability analysis and use it to investigate the failure case study of the Adige River embankment;
3. To investigate the use of ERT technique in the monitoring of water content in the unsaturated soil of flood embankments.

The conclusions drawn in this work regarding each of the aforementioned objectives are described in the following sections.

An approach for the hazard assessment associated with the instability of flood embankments has been presented in **Chapter 2**. The approach allows taking into account uncertainties in both the hydrological loading (i.e. the flood event) and the hydro-mechanical properties of the soil. In particular, to analyse transient water flow the entire hydrograph has been characterised in probabilistic terms.

The proposed approach is based on the FOSM method, which is used to determine the mean and the variance of the Factor of Safety. The main limitation of the method lies in the a priori assumption of the probability distribution of the Factor of Safety, which is necessary to estimate the probability of failure. In the proposed approach a criterion is suggested to overcome this limitation by applying the Monte Carlo method with a single input variable to select the appropriate probability distribution for the Factor of Safety.

The approach has been successfully validated against its ability to reproduce the observed annual probability of failure for a segment of the flood embankment on the Adige River. One of the main advantages of the FOSM method is that it allows quantifying the influence of the uncertainty of each input variable on the probability of failure. This is a useful tool when planning investigation campaigns in order to direct investments towards a decrease of uncertainty for the most significant variables.

The proposed approach has also the advantage of being accessible to geotechnical engineers with a more traditional, deterministic background. The application of the method does not require much more time and computational effort compared to a conventional deterministic analysis. The time and number of simulations required to achieve a sufficiently accurate estimate of the probability of failure are affordable and easy to manage with any available commercial software, making it an accessible tool for the hazard assessment in routine applications in geotechnical engineering.

The case study of the Adige River embankment has been discussed in more details in **Chapter 3** to analyse the transient water flow in the embankment. The segment of the embankment which experienced instability in the form of a scarp has not fully collapsed, thus offering the chance to investigate soil profile and material properties as they were at the time of instability. This has allowed comparing water flow regime for two sections located within and outside the failure segment respectively.

Soil profile within and outside the failure segment has been inferred from site investigations including boreholes, DPH tests and EM scanning. The hydro-mechanical properties of the embankment and its foundation have been characterised via laboratory tests and inverse analysis of water flow based on field measurements of piezometers and tensiometers.

The analysis of the water flow regime for the section within the failure segment has shown that the contrast in hydraulic conductivity in the foundation layer on the landside leads to an upward diversion in the water flow, which in turn generates a build-up of pore-water pressures at the toe of the embankment. However, in the section outside the failure segment, having a homogeneous foundation, the water flow in the horizontal direction towards the landside is not diverted and dissipation of hydraulic head takes place uniformly in the foundation layer beneath the embankment and on the landside.

The comparison of transient water flow regime for the two sections has shown that the contrast in hydraulic conductivity between the foundation layer and the embankment does not represent the only critical condition for the development of uplift pressures at the toe of the embankment. The hydraulic response of the material on the landside outside the footprint of the embankment can play a crucial role in governing the water flow regime and, in turn, affecting the stability of the embankment. These results have highlighted the importance of characterising the hydraulic properties of the material on the landside outside the footprint of the embankment; this aspect should be considered and addressed during site investigations.

In addition to conventional geotechnical techniques based on local sensors, the use of ERT for the monitoring of water regime in flood embankments has been assessed in **Chapter 4**. Two ERT campaigns have been carried out with the aim to map water content in the unsaturated zone of the embankment along the Adige River, along the same segment where a monitoring system consisting of piezometers and tensiometers is installed. This has offered the chance to compare ERT-derived water content profiles to results of water flow simulations calibrated via inverse analysis of the field monitoring data.

The relationship between electrical resistivity and volumetric water content has been determined via laboratory tests with TDR on intact and compacted samples collected from the embankment. The resistivity profiles obtained from ERT measurements have been corrected to account for temperature variations in the subsoil and converted into water content profiles using the laboratory-derived relationship between resistivity and water content. Comparison with results of numerical water flow simulations has shown that ERT can reproduce the trend in water content profiles from a qualitative point of view. However, a quantitative interpretation of the results can be affected by the high contrast in resistivity values between the different layers of the embankment, which can generate artefacts during the inversion process.

This issue has been addressed by deriving an experimental field-specific relationship between the water content and the ERT derived resistivity. This can be achieved by coupling ERT-derived resistivity profiles to direct or indirect measurements of water content in the field. When such a relationship has been applied, ERT-derived water content profiles have provided a good quantitative estimation of water content in the embankment.

ERT has therefore proved to be a valuable tool to quantify the water content in the unsaturated zone of flood embankments, provided that, where high contrasts in resistivity are observed, an initial water content measurement is used to derive a field-specific relationship between water content and ERT measured resistivity. This technique is quick, cost-effective and can be easily implemented on a large scale to monitor the water regime, which can represent a useful tool in the characterisation of the hydro-mechanical model of the embankment.

The overarching aim connecting the three research objectives was the development of a suitable method for the hazard assessment associated with the instability of flood embankments. Since the challenging aspect for the stability analysis of flood embankments is represented by the long scale of these structures, the thesis focused on the development of a flexible and simple method that could be adopted for routine analysis with affordable investments in terms of time, effort and depth of investigation.

This has been achieved by both developing an accessible probabilistic approach which does not require an excessive time or computational effort, and providing a method to characterise the deterministic hydro-mechanical model of the embankment which can easily be extended to long segments. The Adige River embankment case study allowed validating the proposed probabilistic approach against the observed probability of failure, proving that it is a suitable and effective tool for the hazard assessment associated with the instability of flood embankments. Moreover, the monitoring system and the ERT survey campaigns that were carried out on the same segment of embankment allowed highlighting the potential of this technique for diffuse monitoring of water flow, which in turn can provide valuable information to characterise the hydro-mechanical model of the embankment. The proposed method offers a flexible framework which is not dependent on the specific characteristics of the case study considered in this thesis and could be easily adapted to applications in different contexts.

6. RECOMMENDATIONS FOR FURTHER WORK

The approach proposed for the hazard assessment associated to the instability of flood embankments has been tested and validated against a case study along the Adige River embankment. A first step to confirm the validity of the approach would be testing it against failure case studies of different flood embankments. The proposed approach could be tested against its ability to reproduce the observed annual probability of failure for other cases where failures have been documented and information about material characterisation is still available.

It would also be interesting to analyse the performance of the approach for embankments made of finer materials such as clay, as is often the case in other geographical areas. In this case, it may be necessary to consider different failure mechanisms, such as instability on the riverside or erosion. This can be achieved by adapting the proposed FOSM-based method to analyse different failure mechanisms. Once a model is defined to characterise the performance function for the failure mechanism of interest, the method can be implemented with the same approach described in this work. The key variables affecting the variability of the performance function should be identified and characterised via a probability distribution, using approximate estimates if necessary. The performance function should be evaluated in $2v+1$ points, if v is the number if random input variables, to calculate the mean and standard deviation. The Monte Carlo method with a single variable should then be applied to select the appropriate probability distribution of the performance function and calculate the probability of failure associated to each failure mechanism. The overall probability of failure can then be calculated by combining the probability of failure of all the failure mechanisms considered for the embankment (Phoon, 2008).

One limitation of the approach presented in this work is the assumption of homogeneous soil within each layer of the embankment. Uncertainties in the characterisation of soil properties derive from limitations in the experimental procedure, from the natural variability of soils, and also from the spatial distribution of their properties within the considered domain. This can be taken into account by applying the theory of random fields (Vanmarcke, 1983) and considering the statistical parameter of the autocorrelation distance, i.e. the distance over which a soil property is strongly correlated. The proposed approach could therefore be developed to account for the spatial heterogeneity of soil in the embankment and its foundation.

Another limitation of the proposed approach is represented by the assumptions about soil-atmosphere interaction. The soil-atmosphere interaction was not taken into account in the boundary conditions of the seepage model as inward or outward flux (i.e. rainfall or evaporation). This assumption may be representative of the condition on the crest of the embankment, which is covered by impermeable asphalt, but on the sloping sides of the embankment the interaction with the atmosphere may affect the water flow in the embankment. Neglecting evaporation may be considered a conservative assumption, as it leads to an increase of suction and therefore of shear strength. However, the effect of rainfall on the water regime in the embankment could lead to saturation of the shallow layers of soil and a reduction of shear strength, which may play a significant role on the stability of the embankment. This is especially relevant for materials which are relatively permeable, as in the case of the Adige River embankment. The proposed FOSM-based approach could be easily extended to account for the soil-atmosphere interaction by considering the rainfall parameters as additional input variables in the seepage and stability analysis. Rainfall intensity and duration may be considered in probabilistic terms, with a similar approach to the one implemented for the hydrograph variables. Further research would be required to investigate the hydrological interaction between rainfall and flood events, and correlation between variables should be taken into account.

The natural application for the proposed approach would be predicting the probability of failure for existing embankments. The approach can be easily extended to assess the probability of failure for different representative cross sections along segments of the embankment, in order to compare the values and identify the critical areas. This information can help the authorities in the decision process regarding mitigation strategies, for example to prioritise remedial measures to reinforce embankments where the probability of failure is higher.

In order to assess the probability of failure the hydro-mechanical properties of the soil in the embankment and its foundation need to be characterised. An experimental characterisation can be carried out via site investigations, field measurements and laboratory testing on samples collected from the field. However, flood embankments are linear structures which can reach lengths of thousands of kilometres. It would be extremely expensive, and practically not feasible, to achieve a detailed experimental hydro-mechanical characterisation for the soil along the entire span of the embankment.

The next step to improve the accessibility and applicability of the proposed approach would therefore lie in a simplification of this process. One option to characterise the hydraulic model is to rely on the inverse analysis of field monitoring of water flow. To this purpose, ERT is a promising technique for diffuse monitoring of water content more cheaply and quickly, compared to traditional monitoring systems based on local sensors. It has proved to offer a good prediction of water content variations in the unsaturated soil if a field-specific relationship between ERT-measured resistivity and water content is developed. However using ERT to monitor water content is a fairly recent approach, compared to more traditional monitoring systems based on local sensors. This conclusion could therefore be corroborated by further experimental evidence by comparing water content profiles estimated via ERT to direct or indirect measurements of water content in the field for different flood embankments (Fan, et al., 2015).

Limitations in the use of ERT method for monitoring water content have been attributed to the high contrast in resistivity observed between the layers of the embankment. A better understanding of the artefacts generated during the inversion process could also improve the quality of the water content estimation obtained from ERT measurements. This could be achieved by generating sets of synthetic resistivity data (forward modelling) with high resistivity contrasts and analysing the results of the inversion process (Carey, et al., 2017). This would help to identify and isolate the anomalies in the resistivity profiles that are generated by artefacts in the inversion process.

If a more reliable interpretation of ERT results could be achieved, this technique could be implemented for the hydraulic characterisation of flood embankments via inverse analysis of water flow by taking repeated measurements over time and analysing the changes in water regime, with the same approach adopted with local sensors.

A further step to simplify the characterisation of the hydro-mechanical model could be accomplished by deriving the key hydro-mechanical soil characteristics from easily available soil parameters, such as bulk density or particle size. Many hydraulic properties show some correlations to grain size distribution: the hydraulic conductivity depends strongly on the pore size, while the parameters of the water retention curve depend on both the largest pore size and on the pore size distribution. Also for the shear strength there is a correlation between grain size distribution and friction angle, with coarser materials showing generally higher values of friction angle. The friction angle can also be related to the relative density or other easy-to-determine parameters like the results of SPT tests (see for example Peck, et al. (1974); Hatanaka & Uchida (1996)).

In the literature there are many well-established examples of empirical correlations which allow estimating the hydraulic conductivity or the water retention behaviour from the grain size distribution of soil (see for example for the hydraulic conductivity Hazen (1892); Carman (1937); Vukovic & Soro (1992); for the water retention curve

Vereecken, et al. (1989)). Determining the grain size distribution for soil samples collected from the embankment and its foundation would be easier and cheaper than a detailed hydro-mechanical experimental characterisation. A further development could therefore be implementing the use of such empirical correlations in the framework of the proposed FOSM-based approach, making it more widely employable in routine engineering practice.

7. REFERENCES

Aldegheri, A., 2009. *Instabilità degli Argini Fluviali: il Caso di S. Floriano (BZ).* s.l.:Università degli Studi di Trento.

Amabile, A., Cordão-Neto, M., De Polo, F. & Tarantino, A., 2016. *Reliability analysis of flood embankments taking into account a stochastic distribution of hydraulic loading.* Paris, Proceedings of 3rd European Conference on Unsaturated Soils .

Angelucci, D., 2013. *La valle dell'Adige: genesi e modificazione di una grande valle alpina come interazione tra dinamiche naturali e fattori antropici. Conference: Il fiume, le terre, l'immaginario. L'Adige come fenomeno storiografico complesso.* Rovereto, V. Rovigo.

Archie, G. E., 1942. Electrical Resistivity Log as an Aid in Determining Some Reservoir Characteristics. *Transactions of the American Institute of Mining and Metallurgical Engineers,* Volume 146, pp. 54-62.

Arnold, P. & Hicks, M., 2011. *A stochastic approach to rainfall-induced slope failure, in Proceedings of the 3rd International Symposium on Geotechnical Safety and Risk.* Munich, Karlsruhe, Germany, Bundesanstalt für Wasserbau.

Baecher, G. & Christian, J., 2005. *Reliability and Statistics in Geotechnical Engineering.* s.l.:John Wiley & Sons.

Baker, J. & Allmaras, R., 1990. System for automating andmultiplexing soil moisture measurement by time-domain reflectometry. *Soil Sci Soc Am J,* 54(1), pp. 1-6.

Ball, J., 2002. Characteristic Impedance of Unbalanced TDR Probes. *IEEE TRANSACTIONS ON INSTRUMENTATION AND MEASUREMENT,* 51(3), pp. 532-536.

Bishop, A., 1955. The use of the Slip Circle in the Stability Analysis of Slopes. *Géotechnique,* 5(1), pp. 7-17.

Brunet, P., Clément, R. & Bouvier, C., 2010. Monitoring soil water content and deficit using ERT - A case study in the Cevennes area, France. *Journal of Hydrology,* Volume 380, p. 146–153.

Buijs, F., Simm, J., Wallis, M. & Sayers, P., 2007. *Performance and Reliability of Flood and Coastal Defences,* London: Defra.

Calamak, M. & Yanmaz, A., 2017. Uncertainty Quantification of Transient Unsaturated Seepage through Embankment Dams. *Int. J. Geomech.,* 17(6).

Carey, A., Paige, G., Carr, B. & Dogan, M., 2017. Forward modeling to investigate inversion artifacts resulting from time-lapse electrical resistivity tomography during rainfall simulations. *Journal of Applied Geophysics* , Volume 145, p. 39–49.

Carman, P., 1937. Fluid Flow through Granular Beds. *Trans.Inst.Chem. Eng.,* Volume 15.

Castiglione, P. & Shouse, P., 2003. The effect of ohmic cable losses on time-domain reflectometry measurements of electrical conductivity. *Soil Sci Soc Am J,* Volume 67, p. 414–424.

CEN, 2004. *EN 1997-1: Geotechnical design: part 1: general rules.* Brussels, Belgium: Comité Européen de Normalization.

Chambers, J. et al., 2014. 4D electrical resistivity tomography monitoring of soil moisture dynamics in an operational railway embankment. *Near Surface Geophysics,* Volume 12, pp. 61-72.

Christian, J., Ladd, C. & Baecher, G., 1994. Reliability applied to slope stability analysis. *J. Geotech. Engrg.,* 120(12), pp. 2180-2207.

CIRIA; French Ministry of Ecology; USACE, 2013. *The International Levee Handbook.* London: Ciria.

Cygal, A., Stefaniuk, M., Kret, A. & Kurowska, M., 2016. The application of electrical resistivity tomography (ERT), induced polarization (IP) and electromagnetic conductivity (EMC) methods for the evaluation of technical condition of flood embankment corpus. *Geology, Geophysics and Environment,* 42(3), p. 279–287.

Duncan, J., 2000. Factors of Safety and reliability in geotechnical engineering. *J. Geotech. Geoenviron. Eng.,* 126(4), pp. 307-316.

El-Ramly, H., Morgenstern, N. & Cruden, D., 2002. Probabilistic slope stability analysis for practice. *Can. Geotech. J.,* Volume 39, p. 665–683.

Fan, J. et al., 2015. Quantifying spatiotemporal dynamics of root-zone soil water in a mixed forest on subtropical coastal sand dune using surface ERT and spatial TDR. *Journal of Hydrology,* Volume 523, p. 475–488.

Fenton, A., 2014. Simulation. In: M. Hicks & C. Jommi, eds. *Stochastic Analysis and Inverse Modelling.* s.l.:Alert Doctoral School , pp. 127-180.

Ferre, P., Knight, J., Rudolph, D. & Kachanoswki, R., 1998. The sample areas of conventional and alternative time domain reflectometry probes. *Water Resources Research,* Volume 36, p. 2461–2468.

GEO-SLOPE, 2004. *Seepage Modeling with SEEP/W.* s.l.:GEO-SLOPE International, Ltd..

GEO-SLOPE, 2004. *Stability Modeling with SLOPE/W.* s.l.:GEO-SLOPE International Ltd. .

Geotomo, 2003. *Geoelectrical imaging 2D and 3D.* s.l.:s.n.

Giese, K. & Tiemann, R., 1975. Determination of complex permittivity from thin-sample time domain reflectometry improved analysis of step response waveform. *Adv. Mol. Relax. Processes ,* Volume 7, p. 45–59.

Guerreiro, S. et al., 2018. Future heat-waves, droughts and floods in 571 European cities. *Environmental Research Letters,* Volume 13.

Gui, S., Zhang, R., Turner, J. & Xue, X., 2000. Probabilistic slope stability analysis with stochastic soil hydraulic conductivity. *J. Geotech. Geoenviron. Eng.,* 126(1), pp. 1-9.

Gunn, D. et al., 2015. Moisture monitoring in clay embankments using electrical resistivity tomography. *Construction and Building Materials,* Volume 92, p. 82–94.

Hatanaka, M. & Uchida, A., 1996. Empirical correlation between penetration resistance and internal friction angle of sandy soils. *Soils and Foundations,* 36(4), pp. 1-9.

Hayley, K., Bentley, L., Gharibi, M. & Nightingale, M., 2007. Low temperature dependence of electrical resistivity: Implications for near surface geophysical monitoring. *Geophysical Research Letters,* 34(18).

Hazen, A., 1892. *Some Physical Properties of Sands and Gravels, with Special Reference to their Use in Filtration.,* s.l.: Massachusetts State Board of Health, Pub.Doc. No.34, 539-556.

Hilbich, C. et al., 2009. Applicability of Electrical Resistivity Tomography Monitoring to Coarse Blocky and Ice-rich Permafrost Landforms. *Permafrost and Periglacial Processes* , 20(3), pp. 269-284.

Johansson, S. & Dahlin, T., 1996. Seepage monitoring in an earth embankment dam by repeated resistivity measurements. *European Journal of Engineering and Environmental Geophysics,* 1(3), pp. 229-247.

Jongman, B. et al., 2014. Increasing stress on disaster-risk finance due to large floods. *Nature Climate Change,* 4(4), pp. 264-268.

Kasuda, T. & Archenbach, P., 1965. Earth Temperature and Thermal Diffusivity at Selected Stations in the United States. *ASHRAE Transactions,* 71(1).

Keller, G. & Frischknecht, F., 1966. *Electrical Methods in Geophysical Prospecting.* Oxford: Pergamon Press.

Lambe, T. & Whitman, R., 1969. *Soil Mechanics.* s.l.:Wiley.

Liang, R., Nusier, O. & Malkawi, A., 1999. A reliability based approach for evaluating the slope stability of embankment dams. *Engineering Geology,* Volume 54, p. 271–285.

Likos, W., Lu, N. & Godt, J., 2014. Hysteresis and Uncertainty in Soil Water-Retention Curve Parameters. *J. Geotech. Geoenviron. Eng.,* 140(4).

Lin, C., Hung, Y., Yu, Z. & Wu, P., 2013. Investigation of abnormal seepages in an earth dam using resistivity tomography. *Journal of GeoEngineering,* 8(2), pp. 61-70.

Malkawi A.I.H., H. W. A. F., 2000. Uncertainty and reliability analysis applied to slope stability. *Structural Safety,* Volume 22, pp. 161-187.

Marsland, A. & Randolph, M., 1978. A study of the variation and effects of water pressures in the pervious strata underlying Crayford Marshes. *Géotechnique,* 28(4), pp. 435-464.

Moellmann, A., Vermeer, P. & Huber, M., 2011. A probabilistic finite element analysis of embankment stability under transient seepage conditions. *Georisk,* 5(2), pp. 110-119.

Nabighian, M., 1992. *Electromagnetic Methods in Applied Geophysics, Volume 2.* Denver, Colorado, US: Newmont Exploration Limited.

Nguyen, V. & Chowdhury, R., 1985. Simulation for risk analysis with correlated variables. *Géotechnique*, 35(1), pp. 47-58.

Otálvaro, I., Cordão-Neto & M.P., 2013. *Probabilistic analyses of slope stability under infiltration conditions, in Advances in Unsaturated Soils.* Cartagena de Indias, Colombia, Taylor & Francis Group.

Pal Arya, S., 2001. *Introduction to Micrometeorology.* 2nd edition ed. s.l.:Academic Press.

Peck, R. B., Hanson, W. E. & Thornburn, T. H., 1974. *Foundation Engineering, 2nd ed.*. New York: Wiley.

Phoon, K., 2008. *Reliability-Based Design in Geotechnical Engineering. Computations and Applications.* s.l.:Taylor & Francis.

Pozzato, A., Tarantino, A. & De Polo, F., 2014. Analysis of the effects of the partial saturation on the Adige river embankment stability. In: *Unsaturated Soils: Research & Applications.* Sydney, Australia: s.n., pp. 1367--1372.

Reynolds, J., 2011. *An Introduction to Applied and Environmental Geophysics.* Oxford: John Wiley & Sons.

Rings, J., Scheuermann, A., Preko, K. & Hauck, C., 2008. Soil water content monitoring on a dike model using electrical resistivity tomography. *Near Surface Geophysics*, 6(2), pp. 123-132.

Robinson, D. et al., 2003. Considerations for improving the accuracy of permittivity measurement using time domain reflectometry: air-water calibration, effects of cable length. *Soil Sci Soc Am J* , Volume 67, p. 62–70.

Samouelian, A. et al., 2005. Electrical resistivity survey in soil science: a review. *Soil & Tillage Research* , Volume 83, p. 173–193.

Schultz, M., Gouldby, B., Simm, J. & Wibowo, J., 2010. *Beyond the Factor of Safety: Developing Fragility Curves to Characterize System Reliability,* Washington: USACE.

Shah, P. & Singh, D., 2005. Generalized Archie's Law for Estimation of Soil Electrical Conductivity. *Journal of ASTM International,* 2(5).

Simeoni, L., Zatelli, P. & Floretta, C., 2014. Field measurements in river embankments: validation and management with spatial database and webGIS. *Nat Hazards,* Volume 71, p. 1453–1473.

Suchomel, R. & Mašín, D., 2010. Comparison of different probabilistic methods for predicting stability of a slope in spatially variable c–u soil. *Computers and Geotechnics,* Volume 37, pp. 132-140.

Tarantino, A. & El Mountassir, G., 2013. Making unsaturated soil mechanics accessible for engineers: preliminary hydraulic-mechanical characterisation and stability assessment. *Engineering Geology,* Volume 165, pp. 89-104.

Tarantino, A. & Mongiovì, L., 2003. Calibration of tensiometer for direct measurement of matric suction. Technical Note.. *Géotechnique,* 53(1), pp. 137-141.

Tarantino, A. & Pozzato, A., 2008. Strumenti per il monitoraggio della zona non satura (in Italian). *Rivista Italiana di Geotecnica,* Volume 3, pp. 109-126.

Tarantino, A., Ridley, A. & Toll, D., 2008. Field Measurement of Suction, Water Content, and Water Permeability. *Geotech Geol Eng,* Volume 26, pp. 751-782.

Tarantino, A. & Tombolato, S., 2005. Coupling of hydraulic and mechanical behaviour in unsaturated compacted clay. *Géotechnique,* 55(4), pp. 307-317.

Tobutt, D. C., 1982. Monte Carlo simulation methods for slope stability. *Computers and Geosciences,* 8(2), pp. 199-208.

Topp, G., Davis, J. & Annan, A., 1980. Electromagnetic determination of soil water content: measurements in coaxial transmission lines. *Water Resour Res* , Volume 16, p. 574–582.

Topp, G., Yanuka, M., Zebchuk, W. & Zegelin, S., 1988. Determination of electrical conductivity using TDR: soil and water esperiments in coaxial lines. *Water Resour Res,* 24(7), p. 945–952.

Tracy, F., Brandon, T. & Corcoran, M., 2016. *Transient Seepage Analyses in Levee Engineering Practice,* s.l.: U.S. Army Corps of Engineers.

U.S. Army Corps of Engineers, 1997. *Introduction to probability and reliability methods for use in geotechnical engineering,* s.l.: s.n.

Uzielli, M., Lacasse, S., Nadim, F. & Phoon, K., 2007. Soil variability analysis for geotechnical practice. In: *Characterisation and Engineering Properties of Natural Soils.* s.l.:Taylor & Francis Group, pp. 1653-1754.

Van Genuchten, M., 1980. A Closed-form Equation for Predicting the Hydraulic Conductivity of Unsaturated Soils. *Soil Sci. Soc. Am. J.,* Volume 44, pp. 892-898.

Vanapalli, S., Fredlund, D., Pufahl, D. & Clifton, A., 1996. Model for the prediction of shear strength with respect to soil suction. *Can. Geotech. J.,* Volume 33, pp. 379-392.

Vanmarcke, E. H., 1983. *Random Fields: Analysis and Synthesis.* Cambridge, Massachusetts: : MIT Press..

Vereecken, H., Feyen, J., Maes, J. & Darius, P., 1989. Estimating the soil moisture retention curve characteristic from texture, bulk density, and carbon content. *Soil Science,* Issue 148, pp. 389-403.

Vukovic, M. & Soro, A., 1992. *Determination of Hydraulic Conductivity of Porous Media from Grain-Size Composition.* Littleton, Colorado: Water Resources Publications.

Weast, R., Astle, M. & Beyer, W., 1985. *CRC Handbook of Chemistry and Physics.* Boca Raton, Florida: CRC Press, Inc..

Werth, K., 2003. *Geschichte der Etsch: zwischen Meran und San Michele Flussregulierung, Trockenlegung der Möser, Hochwasserschutz.* s.l.:Tappeiner.

Wolff, T. et al., 2004. *Geotechnical Reliability of Dam and Levee Embankments,* s.l.: U.S. Army Corps of Engineers.

Zegelin, S., White, I. & Russel, G., 1989. Improved field probes for soil water content and electrical conductivity measurement using time domain reflectometery. *Water Resour Res*, 25(11), pp. 2367-2376 .

Zhang, L., Zhang, L. & Tang, W., 2005. Rainfall-induced slope failure considering variability of soil properties. *Géotechnique*, 55(2), pp. 183-188.

Zio, E. & Marseguerra, E., 2002. *Basics of the Monte Carlo method with application to system reliability*. s.l.:LiLoLe-Verlag.

Zwanenburg, C. et al., Submitted 2017. Lessons learned from dike failures in the past decades. *International Journal of Geoengineering Case histories.*

List of Figures

List of Tables

8. APPENDIX

8.1 Effect of microstructure on the relationship between electrical resistivity and volumetric water content

The Electrical Resistivity Tomography (ERT) technique can be used to map the water content of geotechnical structures in the unsaturated zone. Since the ERT maps the distribution of electrical resistivity, the relationship between electrical resistivity and volumetric water content has to be known to estimate the water content from the ERT measurements. This relationship can be derived by Archie's law (1942) as previously discussed:

$$\rho = k \cdot n^{-p} \cdot {S_r}^{-m} \qquad \textbf{\textit{Eq. 8.1}}$$

where ρ is the electrical resistivity, n is the porosity, S_r is the degree of saturation and k, p and m are coefficients depending on the type of soil, with k also dependent on the resistivity of the fluid in the pores. If the fitting parameters p and m are assumed to have the same value, the generalised Archie's law (Shah & Singh, 2005) can be used to relate electrical resistivity ρ to volumetric water content θ as follows:

$$\theta = \alpha\rho^{-\beta} \qquad \textbf{\textit{Eq. 8.2}}$$

where the calibration parameters α and β can be obtained from laboratory measurements of electrical resistivity and volumetric water content on samples taken from the field. However, there is the problem of assessing the effect of microstructure on the relationship between electrical resistivity and volumetric water content.

Collecting intact samples from the field is not always possible, so often this relationship is determined by testing ‘disturbed’ samples. The question is whether the relationship between resistivity and water content derived for a ‘disturbed’ sample can still be considered representative of the soil in the field. In other words, the question to address is whether the different structure of disturbed and intact samples affects the relationship between the electrical resistivity and the water content.

Reconstituted and compacted samples of ball clay have been tested in the laboratory to assess the influence of soil microstructure (texture) on the relationship between electrical resistivity and volumetric water content. The electrical resistivity and volumetric water content of the ball clay samples have been measured using TDR probes, as explained in **Chapter 4**. To evaluate the effect of soil microstructure, samples prepared in compacted states (at different dry densities) and reconstituted states were tested. The relationship between the electrical resistivity and the water content was therefore determined experimentally for the different samples and compared.

8.1.1 Reconstituted samples

A cake of ball clay with diameter equal to 250 mm and height equal to 200 mm has been prepared from slurry, by mixing the dry powder with water in order to obtain a gravimetric water content equal to 95%. The cake has been consolidated in a Rowe cell under a vertical stress of 100 kPa for ten days and then sealed with cling film for two days in order to let the water content homogenise. In order to estimate the initial volumetric water content a small cylindrical sample has been cut and trimmed from the cake at the same time of the first measurement. The cylindrical sample had diameter equal to 17.7 mm and height equal to 20.0 mm; its weight was recorded before putting it in the oven and then after 24 hours in the oven in order to determine the mass of water lost by the sample m_w. The volumetric water content was then calculated as:

$$\theta = \frac{m_w / \varrho_w}{V_c} \qquad \textbf{\textit{Eq. 8.3}}$$

where ρ_w is the density of water and V_C is the volume of the cylindrical sample.

The first resistivity measurement was taken immediately after the cut of the cylindrical sample; the probe was inserted into the soil by slowly pushing it in the middle of the sample and avoiding deforming rods.

The sample has been air-dried by evaporation in different steps in order to take measurements of electrical resistivity corresponding to different values of volumetric water content. After each evaporation step the sample has been sealed in cling film for 24 hours to let the water content homogenise before taking the measurement. The procedure has been repeated for every evaporation step and the same small cylindrical sample has been used to estimate the volumetric water content at the time of every TDR measurement.

For each measurement the probe has been inserted at a different point of the sample; it was not advisable to use the holes corresponding to previous measurements because the probe may not have been in proper contact with the soil due to shrinkage of the sample during drying. Points for new measurements were always chosen in order to have at least 3 cm around the probe on all sides to ensure adequate sampling volume.

After six measurements the sample became too hard, making it impossible to push the probe in the soil without damaging the rods; besides the size of the sample didn't allow for any more measurements without using previous holes.

8.1.2 Compacted samples

Sixteen samples have been prepared by mixing dry soil and demineralised water in order to achieve target values of volumetric water content between 0.15 and 0.36. Samples have been compacted to three different values of dry density in order to investigate its effect on the relationship between the electrical resistivity and the volumetric water content. The selected values of dry density were 1.20 g/cm^3 (High Density), 1.10 g/ cm^3 (Medium Density) and 0.93 g/ cm^3 (Low Density).

The samples have been compacted in a mould having diameter equal to 100 mm and height equal to 120 mm, therefore their volume V_m was equal to 942500 mm^3. After fixing the value of the dry density ρ_{dry} the amount of dry soil m_s required for each sample was calculated as:

$$m_S = \rho_{dry} V_m \tag{Eq. 8.4}$$

For each value of the target water content θ_{Target} the amount of water m_w to add to each sample was calculated as:

$$m_w = m_s \theta_{Target} \frac{\rho_w}{\rho_{dry}} \qquad \textbf{\textit{Eq. 8.5}}$$

where ρ_w is the density of water at 20°C.

For the preparation of each sample, the dry clay was spread in a thin layer on a tray and sprayed with demineralised water; it was then mixed with a spatula very carefully in order to avoid the formation of lumps. The procedure was carried out as described in **Chapter 4**. Before compaction each sample was left in a sealed plastic bag for 24 hours in order to obtain a homogeneous water content.

For the compaction each sample has been divided in three equal parts. Each part has been put in the mould and compacted until the layer reached the required thickness; the mould had height equal to 120 mm, so each layer was compacted until it reached the thickness of 40 mm. The samples were compacted with standard compaction hammers, having weight equal to 4.5 kg and a drop of 457 mm. For the low density samples, the smaller compaction hammer was used, with weight equal to 2.5 kg and a drop of 305 mm.

A summary of the sample preparation for the compacted samples is reported in Table 8.1. In order to evaluate the influence of the fluid on the bulk resistivity measured with TDR, four additional samples at medium dry density were prepared by mixing the same soil with fluids at different conductivities. Two solutions of dry NaCl and demineralised water have been prepared with different concentrations of NaCl. This allowed comparing resistivity measurements corresponding to three different values of fluid conductivities, i.e. demineralised water (σ_w=0.00005 S/m), a NaCl solution reproducing the conductivity of the Adige River water (σ_w=0.02 S/m), and a NaCl solution with a much higher conductivity (σ_w=0.10 S/m). Samples were prepared and compacted as previously described. After the measurement soil mixed with salty water has been disposed of in order to keep under control the salt concentration and therefore fluid conductivity for each sample.

TDR measurements were taken on each sample immediately after compaction and were not repeated on the same sample, i.e. each sample corresponds to a single measurement of electrical resistivity and volumetric water content.

Type	**Sample**	**ρ_{dry} [g/cm^3]**	**θ_{Target}**	**m_S [g]**	**m_W [g]**	**σ_w [S/m]**
High density	*H1*	1.20	0.15	1200	150	0.00005
	H2	1.20	0.30	1200	300	0.00005
	H3	1.20	0.36	1200	360	0.00005
	H4	1.20	0.21	1200	210	0.00005
	H5	1.20	0.19	1200	190	0.00005
	H6	1.20	0.17	1200	170	0.00005
Medium density	*M1*	1.10	0.15	1100	150	0.00005
	M2	1.10	0.23	1100	230	0.00005
	M3	1.10	0.30	1100	300	0.00005
	M4	1.10	0.19	1100	190	0.00005
	M5	1.10	0.17	1100	170	0.00005
	M_A1	1.10	0.18	1100	180	0.02
	M_A2	1.10	0.28	1100	280	0.02
	M_S1	1.10	0.18	1100	180	0.10
	M_S2	1.10	0.28	1100	280	0.10
Low density	*L1*	0.93	0.15	900	145	0.00005
	L2	0.93	0.23	900	223	0.00005
	L3	0.93	0.30	900	290	0.00005
	L4	0.93	0.19	900	184	0.00005
	L5	0.93	0.20	900	194	0.00005

Table 8.1. Preparation of compacted samples of ball clay.

8.1.3 Results

For every TDR measurement, the volumetric water content was determined with Topp's equation (1980):

$$\theta = -5.3 * 10^{-2} + 2.92 * 10^{-2} K_a - 5.5 * 10^{-4} {K_a}^2 + 4.3 * 10^{-6} {K_a}^3 \qquad \textbf{\textit{Eq. 8.6}}$$

where K_a is the apparent dielectric permittivity of the soil. The electrical resistivity was calculated from the reflection coefficient at infinite time returned by the oscilloscope. The procedure is explained in detail in **Chapter 4**.

Results of electrical resistivity and volumetric water content measurements on all ball clay samples are reported in Figure 8.1 and Table 8.2.

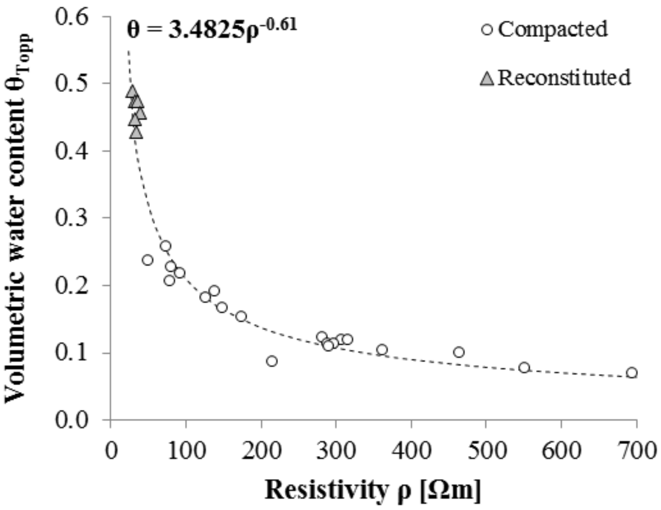

Figure 8.1. Relationship between electrical resistivity and volumetric water content for the ball clay.

Type	Water	Sample	ρ [Ωm]	K_a	θ_{TOPP}
Reconstituted	***Demineralised***	*R0*	28.4	36.2	0.49
		R1	31.6	33.8	0.47
		R2	35.9	33.8	0.47
		R3	38.9	31.5	0.46
		R4	31.5	30.1	0.44
		R5	34.3	27.9	0.43
Compacted	***Demineralised***	*H1*	196.5	5.3	0.09
		H2	73.9	12.2	0.23
		H3	45.0	12.7	0.24
		H4	159.7	8.3	0.15
		H5	280.6	6.7	0.12
		H6	257.3	6.9	0.12
		M1	289.3	6.7	0.12
		M2	115.0	9.7	0.18
		M3	66.4	13.9	0.26
		M4	426.1	5.9	0.10
		M5	264.6	6.5	0.11
		L1	637.4	4.6	0.07
		L2	135.0	9.0	0.17
		L3	84.2	11.6	0.22
		L4	504.5	4.9	0.08
		L5	272.4	6.5	0.11
	Adige-like	*M_A1*	361.4	6.1	0.11
		M_A2	138.3	10.3	0.19
	Saline	*M_S1*	289.3	6.3	0.11
		M_S2	77.2	11.1	0.21

Table 8.2. Results of TDR measurements on all ball clay samples.

Data in terms of volumetric water content appear to be well fitted by a single curve for both reconstituted and compacted samples, showing that the microstructure of soils does not affect electrical resistivity. For compacted samples the dry density doesn’t seem to affect the electrical resistivity because samples with high, medium and low density are very well fitted by the same curve. This is easier to observe from Figure 8.2, which breaks down the results obtained for the compacted samples according to their dry density and to the fluid conductivity. The data point that has the greatest distance from the fitting curve corresponds to the sample H1, with high density and lowest water content. This sample was very hard after compaction and the insertion of the probe was not as smooth as in the other samples; the rods might have been slightly deformed when pushing the probe and this may explain the error in the measurement. Comparison of results obtained on samples prepared with pore fluids at different conductivities shows that the value of the electrical conductivity of the fluid does not seem to affect the bulk resistivity of the samples. Even if the fluid conductivity increases significantly, by 3 orders of magnitude, the bulk resistivity measured with TDR does not seem to change significantly. This is consistent with the behaviour observed in **Chapter 4** and may be due to the electrical interaction between clay particles and ions in water.

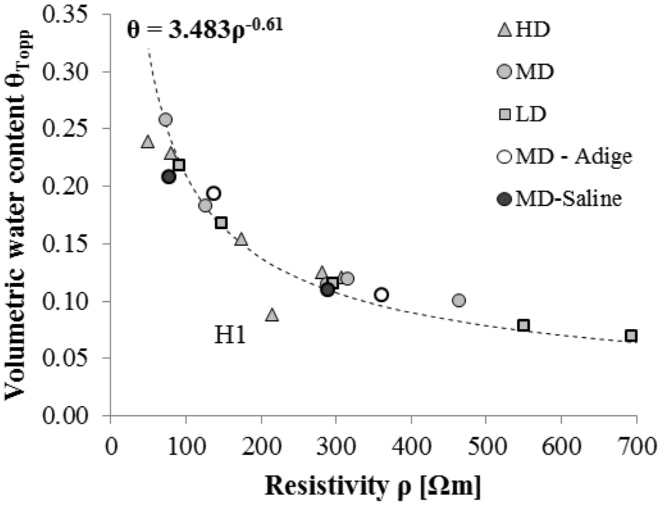

Figure 8.2. Relationship between electrical resistivity and volumetric water content for the compacted samples of ball clay.

These preliminary results show that it is correct to correlate the volumetric water content alone to the electrical resistivity of materials and there is no need to take into account separately the effect of porosity and degree of saturation on electrical resistivity. The effect of microstructure has been assessed by comparing the volumetric water content versus electrical resistivity curve on soil prepared in samples compacted at different dry densities and reconstituted. It appears that the microstructure and the dry density have little effect on the relationship between the volumetric water content and the electrical resistivity. This outcome is very promising for the experimental determination of the relationship between the electrical resistivity and volumetric water content for the sites to be investigated using ERT. They seem to suggest that there is no need to test intact samples in the laboratory to calibrate the relationship between the electrical resistivity and volumetric water content for a soil.